HIGH-PERFORMANCE SIMULATIONS FOR ATMOSPHERIC PRESSURE PLASMA REACTOR

A Dissertation
Submitted to the Graduate Faculty
of the
North Dakota State University
of Agriculture and Applied Science

By

Svyatoslav Chugunov

In Partial Fulfillment
for the Degree of
DOCTOR OF PHILOSOPHY

Major Department:
Mechanical Engineering

October 2012

Fargo, North Dakota

North Dakota State University
Graduate School

Title

HIGH-PERFORMANCE SIMULATIONS FOR ATMOSPHERIC PRESSURE PLASMA REACTOR

By

Svyatoslav Chugunov

The Supervisory Committee certifies that this *disquisition* complies with North Dakota State University's regulations and meets the accepted standards for the degree of

DOCTOR OF PHILOSOPHY

SUPERVISORY COMMITTEE:

Dr. Iskander Akhatov
Chair

Dr. Fardad Azarmi

Dr. Yechun Wang

Dr. Orven Swenson

Approved:

11/07/2012
Date

Dr. Alan Kallmeyer
Department Chair

ABSTRACT

Plasma-assisted processing and deposition of materials is an important component of modern industrial applications, with plasma reactors sharing 30% to 40% of manufacturing steps in microelectronics production [1]. Development of new flexible electronics increases demands for efficient high-throughput deposition methods and roll-to-roll processing of materials. The current work represents an attempt of practical design and numerical modeling of a plasma enhanced chemical vapor deposition system. The system utilizes plasma at standard pressure and temperature to activate a chemical precursor for protective coatings. A specially designed linear plasma head, that consists of two parallel plates with electrodes placed in the parallel arrangement, is used to resolve clogging issues of currently available commercial plasma heads, as well as to increase the flow-rate of the processed chemicals and to enhance the uniformity of the deposition. A test system is build and discussed in this work. In order to improve operating conditions of the setup and quality of the deposited material, we perform numerical modeling of the plasma system. The theoretical and numerical models presented in this work comprehensively describe plasma generation, recombination, and advection in a channel of arbitrary geometry. Number density of plasma species, their energy content, electric field, and rate parameters are accurately calculated and analyzed in this work. Some interesting engineering outcomes are discussed with a connection to the proposed setup. The numerical model is implemented with the help of high-performance parallel technique and evaluated at a cluster for parallel calculations. A typical performance increase, calculation speed-up, parallel fraction of the code and overall efficiency of the parallel implementation are discussed in details.

ACKNOWLEDGEMENTS

First and foremost, I would like to express my appreciation to my academic adviser Dr. Iskander Akhatov for his mentoring throughout my education at North Dakota State University. I would like to thank him for his support, advising and encouraging that helped me to grow as a research scientist and complete my research.

I would also like to thank my committee members Dr. Fardad Azarmi, Dr. Yechun Wang, and Dr. Orven Swenson for guiding and assisting me in my research when it was necessary as well as for their brilliant comments and suggestions. Their expertise was of a great help in the completion of this thesis.

There is no doubt that I would not accomplish this study without the expertise, assistance, and support of different professionals within the North Dakota State University and outside. I would like to thank members of Center for Nanoscale Science and Engineering for collaboration, experience exchange and providing theoretical basis to proceed with my research. My special thanks to Dr. Martin Ossowski for his contribution into the theoretical part of my work and the financial support that helped me to accomplish this project.

And finally, I thank to my family who supported me in everything and encouraged me throughout my experience.

TABLE OF CONTENTS

LIST OF TABLES

LIST OF FIGURES

LIST OF APPENDIX TABLES

LIST OF APPENDIX FIGURES

INTRODUCTION

General Overview

Chemical deposition and coating methods are viable means for an effective manufacturing of electronic parts and components (i.e., ICs [2] and photovoltaic cells [3]), modification of material properties (i.e., wetting parameters [4], surface modification/coating [5], and etching [2], [5]-[7]), deposition of thin films [2], [3], [5]-[7] etc.

There are two general concepts that are used for materials processing. The first concept assumes the deposition at low pressure of the surrounding gas, usually in vacuum. Obvious advantages of such an approach are extreme cleanness of the final product, safe use of hazardous chemicals in the sealed system, and substantial rate of chemical reactions in the absence of contamination from atmospheric gases. On a general basis, the low pressure process provides the best quality of the deposition result, at the same time there are certain limitations that complicate and/or restrict the use of low-pressure process for industrial production, especially in the areas where high throughput and low cost are the primary objectives. The restrictions of the low-pressure units are related to their overall complexity, due to the requirements for sealed chambers, loading/unloading ports, vacuum pumps, and supplementary equipment needed for system operation and control [3]. Not only the capital cost of such a setup is significantly high, but also maintenance of the system poses certain challenges. The setup has to be scaled up to accommodate specimens of larger size. The scaling process requires enlargement of the reactor chamber, which inevitably levels up the cost of the unit and aggravates its maintenance. The result is the increase of the produced materials' cost and the decrease of demand for the product. The scalability of the low pressure setups is compromised by the negative effects associated with

special requirements of the production cycle, in particular with maintaining a specific environment in the reaction chamber. The low pressure in the chamber requires the use of loading/unloading ports to transition samples from air-based atmosphere into the sealed unit. This requirement severely affects the rapidness of the production cycle and the maximum size of the processed specimen. Thus, from one perspective, the low-pressure materials deposition is very accurate technique that could be used for critical applications where cleanness of the result is crucial (e.g. manufacturing of semiconductors, atomic level coatings/sputtering, and nanofabrication). From another perspective, some level of impurities is acceptable for the majority of applications (for instance, photovoltaic cells, anti-corrosion coatings, and fibers production). Therefore, the very accurate low-pressure technique is attractive, but it is not cost-efficient. This is why there is an active search for cheaper and simpler alternative techniques.

The second concept of material processing owes its existence to high-pressure deposition, which usually happens at atmospheric conditions. When the requirement for a sealed and evacuated reaction chamber is eliminated, the system may be constructed without expensive vacuum pumps and chamber seals. The design of the chamber is simplified, allowing a wide range of adjustments for samples of different sizes. The energy use decreases, due to fewer components requiring power input. The time of the production cycle shortens since there is no need for load/unload procedures. The cost of the final product also decreases due to the simplified technological process. The deposition techniques at atmospheric pressure are often producing similar quality of the coatings in comparison to low-pressure processes [3]. Such systems can be developed with mobility in mind, which expands their range of applicability. The payoff for multiple positive features of the high-pressure systems is a dramatic decrease in the rates of chemical reactions which happens due to the presence of chemically reactive gases in the

surrounding atmosphere. To promote the reactions rate, the high-pressure process requires additional energy input in the form of heat flux, electric actuation or catalytic assistance.

The necessary energy input may be provided in a very efficient way, using plasma assisted deposition. The supplied energy is used to break neutral molecules into ions and electrons with the help of kinetic reactions [8,9]. Plasma is generated in the reaction chamber; it interacts with chemical precursors, supplying a surplus of electrons and energetic ions to the chemical reactions [10]. Plasma consists of electrons, positive or/and negative ions. These species respond to electric fields and, being bonded by electric forces, exhibit collective behavior, which is an intrinsic characteristic of plasma. There are two types of plasmas usually distinguished – thermal plasma, and non-thermal plasma. The species of thermal plasma possess comparable quantities of energy; thus, featuring similar temperatures and kinetic velocities. Thermal plasma may reach temperatures up to 10^4 K, this feature determines the range of applications for thermal plasmas – welding, metal cutting, deposition of molten metal particles etc. In many coating applications, excessive heat flux is rather destructive, while energetic ions are desirable to promote modifications of injected chemical precursor or to enhance surface chemistry at a substrate. Non-thermal plasma is an ideal candidate for such applications. This type of plasmas is characterized by a tremendous difference in energy of electrons and ions. Ions are large and bulky in comparison to electrons, with the mass differing by the order of $10^3\,\mathrm{kg}$ (electron mass is $\sim 10^{-30}\,\mathrm{kg}$ and helium ion mass is $\sim 10^{-27}\,\mathrm{kg}$). Because of such bulkiness, ions cannot efficiently accelerate in electric field, especially when surrounded by a gas at atmospheric pressure. This fact is depicted by the low electric mobility of ions. At the same time, electrons are small and light; they rapidly accelerate in an electric field and acquire high kinetic energy, in the range of 5-6 eV (1 eV = 11000 K). Thus, electrons in non-thermal plasma may be very “hot”,

but their total mass is negligible in comparison to ions. The temperature of plasma is determined by ions that constitute the majority of the mass, exchanging their energy with surrounding gas and generating a heat flux.

In this work we consider non-thermal plasma only which we refer to as Atmospheric Plasma (AP); this term is based on the fact that plasma is generated at atmospheric pressure. Generation of plasma involves a certain number of processes, responsible for production of energetic species constituting plasma. These processes take place at the molecular level and are described with rate constants.

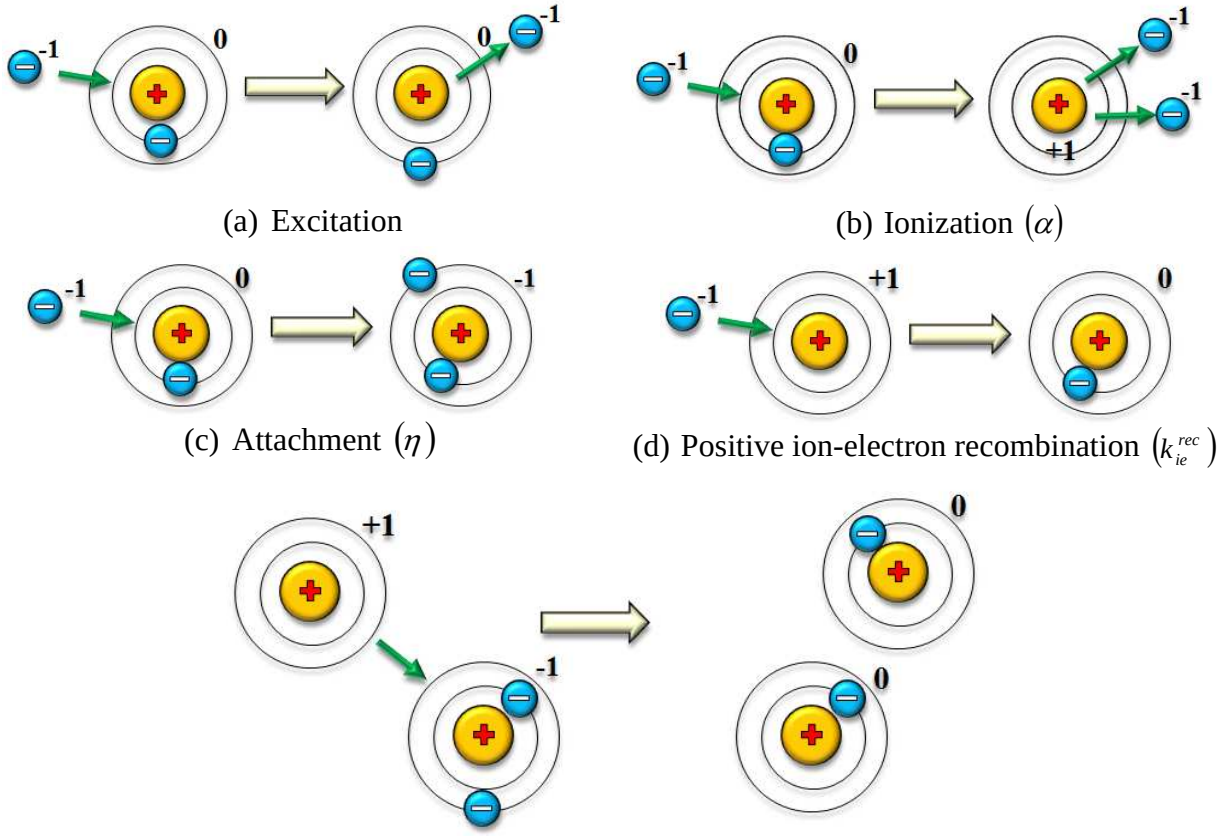

(a) Excitation

(b) Ionization (α)

(c) Attachment (η)

(d) Positive ion-electron recombination (k_{ie}^{rec})

(e) Positive ion-negative ion recombination (k_{ii}^{rec})

Figure 1. Schematics of processes in plasma at atomic level

The most useful rate constants were revealed during experiments by Townsend [6] with discharges in evacuated tubes, they are known as the first, second and third Townsend

coefficients. We explain these coefficients and basic plasma processes using He-based plasma, as this is the test gas we utilize in our theoretical and numerical analysis. Figure 1 contains a schematic diagram that does not truly image the actual physical process (it would require describing ions using a combination of elementary particles and electrons using clouds of charges depicted with proper spin and energy orbit), but provides a simple explanation which is intuitively appealing.

Let us assume that in a plasma generation chamber there are two electrodes arranged in a parallel configuration, the rest of the space is filled with some neutral gas – helium, for instance. Electric potential is applied across a gap created by electrodes, giving rise to an electric field in the gap. When the strength of the electric field increases, the field pulls an electron out of an electrode. The electron is accelerated by the electric field, traveling against the field lines (from lower electric potential to a higher one) and reaching very high velocity. Since the space between the electrodes is filled with a gas, there is a finite distance that the electron may travel without collisions with gas molecules. This distance, called the mean free path [11], is a function of gas pressure, with higher pressure corresponding to shorter distance. For example, for air at atmospheric pressure the mean free path is only 68 nm [12]; therefore, for a 1 mm gap there would be approximately 14700 collisions if electrons would be able to fly over such distance. For helium, the mean free path is in the range of 173.6 nm [13] to 192.7 nm [14], which is explained by the smaller size of the helium atom in comparison to nitrogen, oxygen and water molecules, as the main components of air. The smaller the molecule size, the lower the number of collisions to happen on the way of an electron. Thus, in helium per 1 mm gap, there would be about 5460 collisions. Since the average distance between collisions is quite large, the electron has more time to accelerate to high velocity, than it would in nitrogen. Therefore, in helium,

electrons possess more energy when a collision happens; this energy significantly increases the chances of ionization. This outcome also explains why helium has a lower breakdown voltage in comparison to nitrogen, while ionization energy required for helium is higher than that of nitrogen [3].

There are four types of collision outcomes possible in electron-neutral molecule interactions. The first type – excitation – is related to exchange of energy between the particles. Helium has seven energy levels corresponding to different excited states of its atom (19.82 eV, 20.61 eV, 20.96 eV, 21.21 eV, 22.97 eV, 23.70 eV, 24.02 eV [15]). Excitation may have different forms: increase in rotational and/or vibration energy of the molecule, change of electron orbit; the later excitation form is schematically shown in Figure 1.(a). The molecule may be excited to a certain state for a short period of time; if there is no additional energy input during that period, the molecule returns to its ground state, emitting a quantum of energy in the form of a photon [16, 17]. In our approach we do not consider this process; this is why we do not track energy exchange and excited states of atoms.

The second type of a collision outcome is ionization (Figure 1.(b)). When energy, transferred during the collision, overcomes 24.58 eV, a direct ionization $\mathrm{He} + \mathrm{e} \rightarrow \mathrm{He}^{+} + \mathrm{e} + \mathrm{e}$ takes place. One of the electrons is released from the molecule, at the same time the molecule becomes a positive ion. Ionization may be stepwise, when the molecule gradually increases its excited state during multiple collisions $\mathrm{He} + \mathrm{e} \rightarrow \mathrm{He}^{*} + e$, $\mathrm{He}^{*} + \mathrm{e} \rightarrow \mathrm{He}^{+} + \mathrm{e} + \mathrm{e}$, with the last collision bringing enough energy to overcome the ionization limit. The last energy portion is not necessarily large. It may be even energy absorbed from a photon emitted by another molecule $\mathrm{He} + \hbar\omega \rightarrow \mathrm{He}^{+} + \mathrm{e}$; in this case the process is called photo-ionization [6]. The sufficient photon

wavelength can be determined from $\lambda < \frac{12400\ \text{Å}\cdot\text{eV}}{I(\text{eV})} = \frac{1240\ \text{nm}\cdot\text{eV}}{24.58\ \text{eV}} \approx 50.45\ \text{nm}$, since it is lower than 100 nm, these photons fall into ultraviolet radiation range [6].

Ionization is described with the first Townsend coefficient α, which determines how many new electrons are generated per unit length, along a path of an electron. According to previous calculations, an electron may travel about 180 nm without a collision, constantly accelerating with the help of the electric field. Mokrov and Raizer [18] mention that electrons acquire the energy necessary for ionization faster when the current at the electrodes is higher. Electrons reach velocity $u_e = \frac{eE_0}{m_e \nu_{ea}}$ when accelerated in electric field E_0 with frequency of elastic collisions ν_{ea}. The ionization process takes place [19] when energy of electrons surpasses the ionization energy level $\frac{m_e u_e^2}{2} > I_i$. In the first collision, the electron would lose a portion of its energy; it would accelerate till the next collision, where another portion of energy will be lost. If the electron collides with a positive ion or with a wall/electrode, the electron is lost. Let us, for instance, assume that the electron traveled $1\ \mu\text{m}$ during its lifetime and had 5 collisions. We also assume that each collision led to generation of one new electron-ion pair. The ionization coefficient in this case would be $\alpha = 5\ \text{electrons}/1\ \mu\text{m} = 5\times10^6\ \text{m}^{-1}$. Of course, this calculation is illustrative only, as the number of newly generated electrons in He-based atmospheric plasma is only $\alpha \approx 2700\ \text{m}^{-1}$ for quite high reduced electric field of $24\ \text{Td}$ [15].

The third type of collision outcome is electrons' attachment. When an electron with low energy hits a neutral molecule (Figure 1.(c)), it may attach to one of its orbits, under an assumption that total energy of such a system is below the ionization level. This mechanism is

responsible for formation of negative ions not only from atoms of simple gases, like helium or argon, but also from complex molecules, e.g. $H_2O + e \rightarrow H + OH^-$. In He-based plasma formation of negative ions is possible only at very high voltages and low pressures [20, 21, 22]. Since experimental conditions in an atmospheric plasma setup are way beyond these limits, formation of He^- ions in atmospheric plasmas is almost impossible. This is why we do not consider attachment process in further evaluations.

The fourth type of the collision outcomes is recombination of the species. Recombination is the major mechanism responsible for species loss in plasma. It takes place when a positive ion interacts with a negative ion [23] (Figure 1.(e)) or an electron (Figure 1.(d)). In either case, the charged species are converted into neutral molecules. When recombination happens with the help of an electron, a sum of energies of separate species before the collision is higher than energy of the resultant neutral molecule. This is why this process often happens in the presence of the "third body", which could be another free electron or emitted photon. The "third body" acquires the excess energy in the form of increase of its kinetic energy. Neither ions nor neutral molecules are able to change their kinetic energy fast enough to accumulate recombination energy, this is why these particles cannot be "third body" participants in the process.

Free electrons in plasma occur due to electron emission from the electrode material. The emission strongly depends on the electric field and temperature of the electrodes [24, 25]. At low electric fields thermionic emission is the major supplier of electrons from electrode surface. The electron flux due to emission is described (1) by the Richardson equation [26] with the constant in front of the temperature $A_0 = 4\pi m_e e / (2\pi\hbar)^3 = 1.20173 \times 10^6 \ \mathrm{A/m^2K^2}$ taken in the form proposed by Sommerfeld

$$j = A_0 T^2 (1 - R) \exp(-W/kT) \qquad (1)$$

The flux of emitted electrons j depends on temperature of the electrode T, reflection of electrons from a potential barrier at electrode's surface R, and work function W of the electrode's material. The work function defines a potential barrier at the metal surface that the electron has to overcome in order to leave the material's lattice.

Table 1
Work function and secondary emission for some materials [6]

Material	Work function eV	Secondary emission electron/atom
C	4.7	0.24
Cu	4.4	0.25
Al	4.25	0.26
Mo	4.30	0.26
W	4.54	0.25
Pt	5.32	0.22
Ni	4.5	0.25

It was discovered by Walter Schottky that the work function is lowered [27, 28] in the presence of electric field E by the value (2)

$$\Delta W = \sqrt{e^3/4\pi\varepsilon_0}\sqrt{E}\ [\mathrm{V}] = \sqrt{e/4\pi\varepsilon_0}\sqrt{E}\ [\mathrm{eV}] \qquad W = W_0 - \Delta W \qquad (2)$$

When electric field becomes greater than 10^8 V/m, electron field emission becomes the prevalent electron supplier [29]. In this case electrons' flux from the electrode is determined according to the Fowler-Nordheim equation (3), using Fermi energy of metal ε_F (Fridman uses $\varepsilon_F = 7$ eV for calculations [6])

$$j = \frac{e^2}{4\pi^2\hbar}\frac{1}{W_0 + \varepsilon_F}\sqrt{\frac{\varepsilon_F}{W_0}}\exp\left(-\frac{4\sqrt{2m_e}W_0^{3/2}}{3e\hbar E}\right) \qquad (3)$$

When electric field is high, the Schottky effect is also present, but it cannot be introduced into (3) the same way as it was introduced into (1), using (2). The reason for such complication is that the electron flux at high electric field is very sensitive to small changes in the field values, for

example, 4x increase in electric field corresponds to 10^{23}x increase in electron flux. This is why the correction is introduced in the form of a small parameter ξ

$$j = 0.062\frac{\sqrt{\varepsilon_F}}{(W_0 + \varepsilon_F)\sqrt{W_0}}\exp\left(-\xi\frac{685000\, W_0^{3/2}}{E}\right) \quad (4)$$

The correction parameter is defined in a table form [30]

Table 2
Schottky correction factor for Fowler-Nordheim equation

Quantity	Values									
$\Delta W/W_0$	0	0.2	0.3	0.4	0.5	0.6	0.7	0.8	0.9	1.0
ξ	1	0.95	0.9	0.85	0.78	0.7	0.6	0.5	0.34	0

Another electron source at the electrode is secondary electron emission. This event takes place when a positively charged ion approaches the electrode, altering electric field in the vicinity of the electrode and pulls out an electron. The secondary electron emission becomes distinguishable, when ions come close to the electrodes; this happens when positive plasma column travels more than half of the sheath thickness, being driven by oscillating electric field [31]. This type of emission may be calculated using the secondary emission coefficient

$$\gamma \approx 0.016(I - 2W_0) \quad (5)$$

We calculate the coefficient for helium-based plasma $(I = 24.58\text{ eV})$ in the vicinity of aluminum $(W_0 = 4.25\text{ eV})$ electrode, the result is $\gamma \approx 0.016(I_{He} - 2W_{Al}) = 0.25728.$

Thermal emission of electrons, electric pulling out of a cold metal and ionization of neutral molecules are the major sources of electrons in plasma; they provide electrons' cloud for plasma igniting and sustainment. During their lifetime, electrons participate in collisions with gas molecules and generate more free electrons. This process resembles an avalanche (Figure 2) –

one electron generates another electron, two electrons generate four etc., leading to formation of a cloud of electrons that have random directions and velocities.

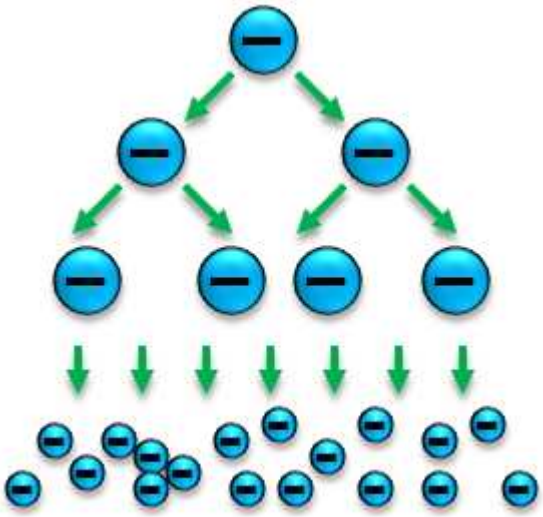

Figure 2. Electrons avalanche

Each collision leading to electron generation also produces a positive ion. Thus, emission and ionization are the main sources of plasma species, while recombination is the main loss mechanism in pure plasmas.

An important characteristic of plasma is the degree of ionization (6), which shows the relation between charged particles and total number of particles constituting plasma-gas. Degree of ionization is an important parameter to determine proper processing of chemicals. Most industrial plasmas are weakly ionized with degree of ionization [32] in the order of $DoI = 10^{-4}$.

$$DoI = \frac{n_i}{n_i + n} \tag{6}$$

Charged particles readily respond to electric field and constitute a displacement current for atmospheric plasmas. Due to increase in number of plasma species, the current also increases, which, in turn, raises plasma temperature through ohmic heating mechanism.

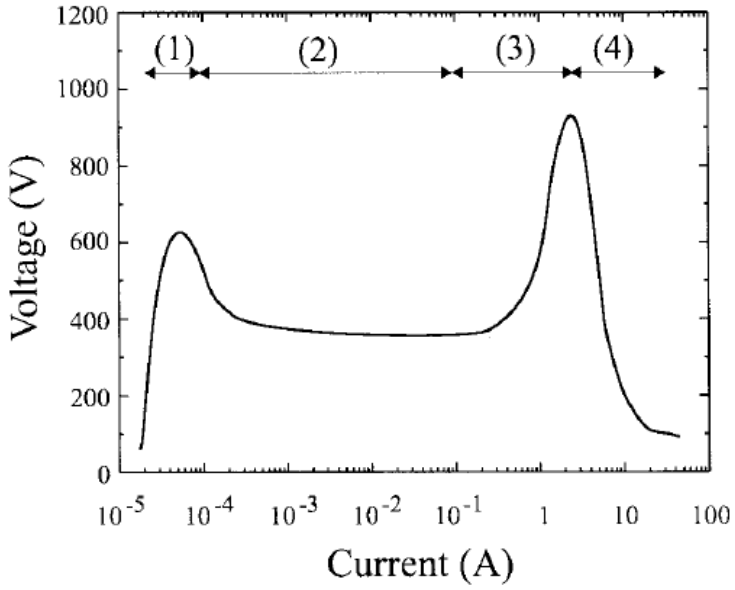

Figure 3. Voltage-current characteristic of dc plasma discharge at low pressure [33]

Raised plasma temperature not only results in larger thermionic currents, but also promotes the secondary emission. With the increased number of electrons due to the emission processes, the plasma loses stability and is prone to arcing. Since arcing is an unfavorable mode for industrial deposition systems, the degree of ionization is usually kept low to not compromise plasma stability.

Figure 3 shows a current-voltage plot of a typical plasma unit. As it is shown in the plot, there are four modes of plasma generation could be distinguished [34]. The first region corresponds to initial plasma generation where electrons are emitted from electrodes, form an avalanche, and generate the necessary amount of positive ions. This process is not very stable, because conductivity of plasma is very low with not many species generated. It requires a substantial voltage to support electric current through hardly conductive plasma. When voltage increases, plasma transfers into the glow mode, which is the second region on the plot. In the glow mode, plasma is almost self-sustained; it requires only small power input to compliment the difference between species produced in bulk plasma and species required for plasma

sustainment. This is why voltage-current curve is flat for this region. The glow mode allows for a wide range of electrical settings for the plasma setup. In particular, the current could be increased, pumping more energy into plasma species and heating them up. If the process continues, thermal instability transfers plasma into unstable glow discharge when secondary emission significantly increases. This process corresponds to the third section on the plot. The last section is arc discharge mode that is energized by secondary electron emission [35]. In this mode plasma becomes extremely conductive, allowing for very high currents to be passed through the discharge gap. While this mode is favorable for welding, cutting, and melting applications, for industrial coatings it is better to defer from this mode into the stable glow discharge.

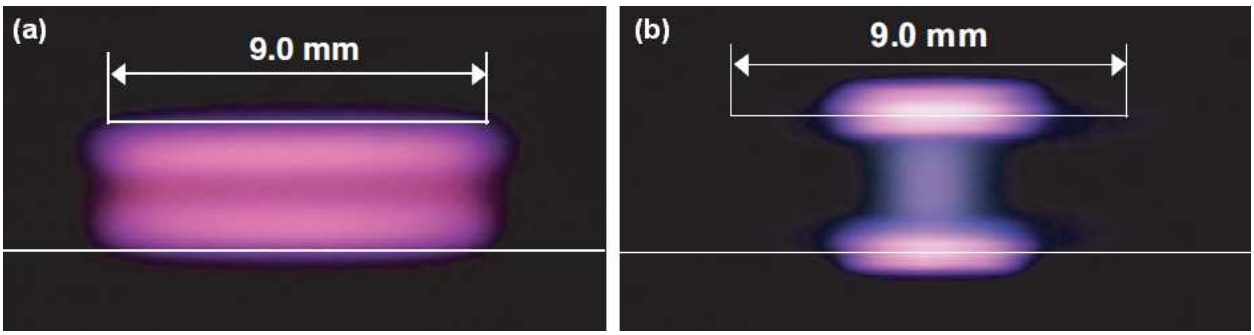

Figure 4. Plasma operated in (a) α-mode and (b) γ-mode [31]

There are two regimes distinguished in plasma operation that are related to the level of electrons' emission. When emission is low with secondary emission almost absent, plasma is said to be in α-mode. The increased emission, with most of the electron flux produced by secondary emission process, turns the plasma into γ-mode [36]. In γ-mode, the plasma is very unstable with arcs being a frequent event (Figure 4).

Plasma is generated with electric field applied to a neutral gas. In the simplest case, the electric field is driven by direct current. This setup offers an ease of operation and control, but modern technologies have specific requirements that cannot be fulfilled as easily.

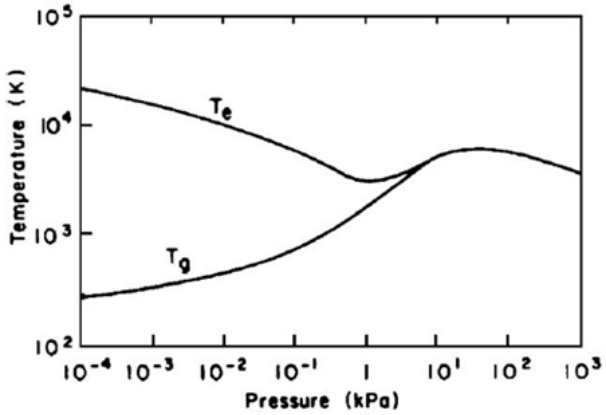

Figure 5. Relation between thermal and non-thermal regimes for dc plasma [37]

The usual DC plasma setup can be operated in non-thermal regime only at low pressures, when pressure increase, stability of the discharge suffers and plasma switches to thermal regime (Figure 5). Hence, plasma driven by AC current is the only suitable candidate for processing of materials at atmospheric pressure.

Plasma driven by AC current is known as RF (Radio Frequency) plasma. There is a lower limit of frequency when RF plasma still can be sustained; the limit is 100 kHz [5]. RF plasmas also suffer from instabilities, mainly due to significant increase of electron flux due to thermionic emission. A successful method to resolve this issue is introduction of dielectric boundary layers. The layers prevent electron flux from entering the plasma when high power input is applied to electrodes. The loss of species into the electrode material is also eliminated. This method helps to increase power content of plasma, at the same time stabilizing the discharge. Thus, RF plasma has multiple advantages over DC plasma when both are compared at atmospheric pressure – it can be sustained in the glow mode, it provides higher energy content to the species, and its

stability may be improved by dielectric boundary layers. Thus, our work focuses on RF plasma as the potential enhancement method for materials deposition.

Experimental Estimations

The problems associated with the CVD systems are overcome by implementation of plasma-assisted deposition. The deposition technique based on the atmospheric pressure plasma (APP) becomes a prevalent choice for everyday material processing [38-40]. With enhanced scalability and portability, the APP based devices employ stable precursors, low temperature processing, and significant reductions in operation cost.

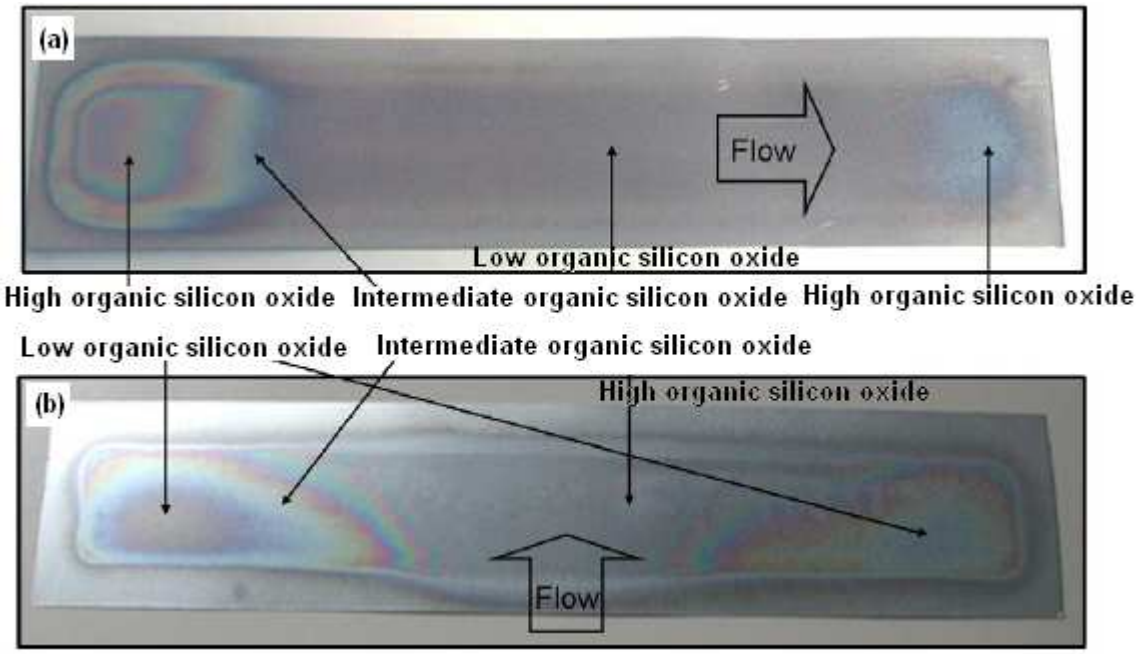

Figure 6. Non-uniformity of materials deposition with plasma flow in (a) longitudinal direction, (b) transverse direction [41]

The APP-based deposition systems that are available on the market feature a common trend in design resembling a “shower-head” geometry which allows the flow of plasma species and modified chemical precursor through multiple tiny outlets. The “shower-heads”, when

assembled into arrays for large-scale processing, result in non-uniformity of the coatings, as well as exhibit significant problems with clogging of the outlet channels [3].

The design of a plasma head proposed in this work is called a “linear plasma head”; it represents a slot between two parallel plates, forming a channel. The width of the head is adjustable depending on demands of a particular application. Plasma is generated inside of the head and exits the slot in a form of a wide “blade”. Chemical species requiring modification are injected right into the blade, having no contact with the head components, thus preventing the clogging. This unit is targeted for advanced coatings over large areas.

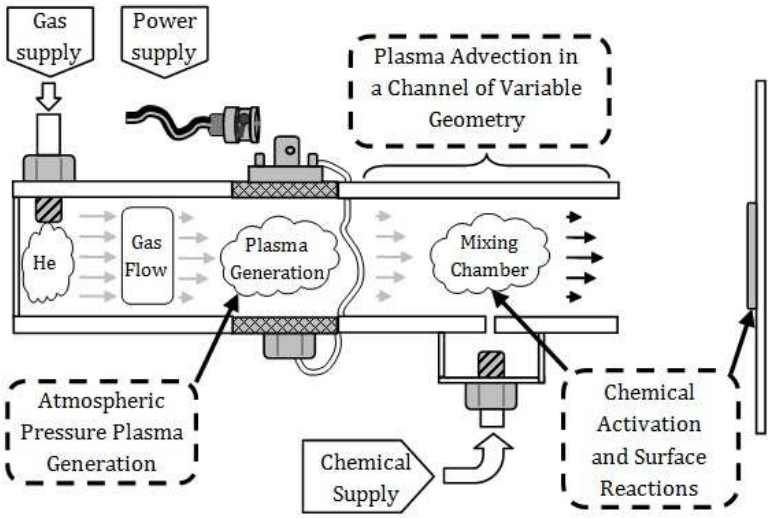

Figure 7. General sketch of the proposed LAPPD reactor. The actual design may feature different configuration and placement of the injectors and modified geometry of the channel for optimized fluidic behavior of the plasma gas

Practical testing of a linear plasma head developed by other research groups revealed that, in general, these units lack uniformity and accuracy of deposition (Figure 6). Because of these complications, we started a theoretical investigation looking for an improvement of the APP reactor design. The primary objectives of this research are applicability of the reactor for large size specimens (in particular, for roll-to-roll processing of materials), ease of maintenance

(no clogging), and ability to optimize the flow of the chemical agents and plasma species using fluidic tools. The Linear Atmospheric Pressure Plasma Deposition (LAPPD) system has been developed to address these issues.

The LAPPD head (Figure 7) consists of two parallel plates made of non-conducting material (Teflon) to form a channel for the flow of the carrier gas (helium). At a certain location in the channel, there are two electrodes (aluminum) placed in a parallel arrangement which induce capacitive plasma discharge, ionizing the flowing neutral gas. The setup is logically split into four sections for gas entrance, plasma generation, fluids mixing, and material deposition. In the first section, the carrier gas enters the setup and develops a laminar flow profile. Solution for this section does not include plasma species and is described with fluidic equations only. The result of the flow simulation is represented by a parabolic velocity profile. In the second section, the carrier gas passes through the space between the electrodes where it becomes ionized due to the RF electric field and leaves the generation section in the form of weakly ionized plasma.

With the help of gas advection, plasma proceeds along the channel into the third section, where a chemical precursor is being injected. The precursor activation takes place in the mixing chamber, with subsequent propagation of the chemicals towards a substrate. The fourth section encloses an open space starting from the plasma head and finishing with the substrate, in order to track the deposition process. The channel geometry could be altered to influence the advection rate and to concentrate plasma species in the specific area, enhancing the activation of the chemicals.

Plasma is generated at atmospheric pressure with temperatures close to 300 K. We utilize an RF-type of plasma as it provides a potential for dielectric layers implementation, leading to improved stability of the glow discharge. In the presented model we consider bare electrodes (no

dielectric layer). The frequency of 13.56 MHz is chosen for RF electric field as this is the internationally accepted industrial standard [2], [5], [42]. Bogaerts et al. [5] provide an estimation of minimal RF frequency for a stable glow discharge as 100 kHz; hence, our operation mode exceeds the minimal requirements. The gap size between the electrodes is in the millimeter range, setting low demands for input power. The typical gap used for our model is 1.6 mm, this size well correlates with the one used in [43] and provides an opportunity for results comparison. In order to determine the proper operation range, we estimate the gas breakdown voltage (7) for $L = 0.16\,\text{cm}$gap, according to [2], [6], and [33]

$$V_{\max} = \frac{BpL}{\ln(ApL) - \ln(\ln(1+1/\gamma_{se}))} = 1742.29\,\text{V} \tag{7}$$

We assumed the multiplier constants $\left(A = 2.8\,\text{cm}^{-1}\text{Torr}^{-1}\right.$ and $\left. B = 77\,\text{V}\cdot\text{cm}^{-1}\text{Torr}^{-1}\right)$ are taken for Helium [2]; the secondary electron emission constant $(\gamma_{se} = 0.26)$ is for Aluminum [6]; and the gas pressure is 1 atm $(p = 760\,\text{Torr})$. Thus, in the proposed operation mode of 400-700 V we expect a smooth plasma glow (the α-mode). Transition to the γ-mode is possible in the real setup [3], [31] when excessive electrons are pulled from the electrodes due to the secondary emission process [2], [42]. This regime is characterized by formation of sparks across the gap and by rapid growth of plasma temperature due to excessive electric currents in plasma. The material of electrodes has a little influence on the glow discharge when the plasma is operated in the α-mode, but its effect becomes quite pronounced when transition to the γ-mode occurs [44]. This fact leads to exact specification of the electrode material for our theoretical and numerical models. Young and Wu [45] mention that fluidic model of plasma is capable of catching the $\alpha - \gamma$ transition, though we do not account for such an effect in our approach, keeping the voltage relatively low.

The developed plasma model and acquired numerical results, presented in this work, are based on the design similar to the one used in our experimental evaluation. The proposed setup is based on a plasma head, featuring a generation chamber, tuned for capacitive plasma discharge and injection units for input of a chemical precursor.

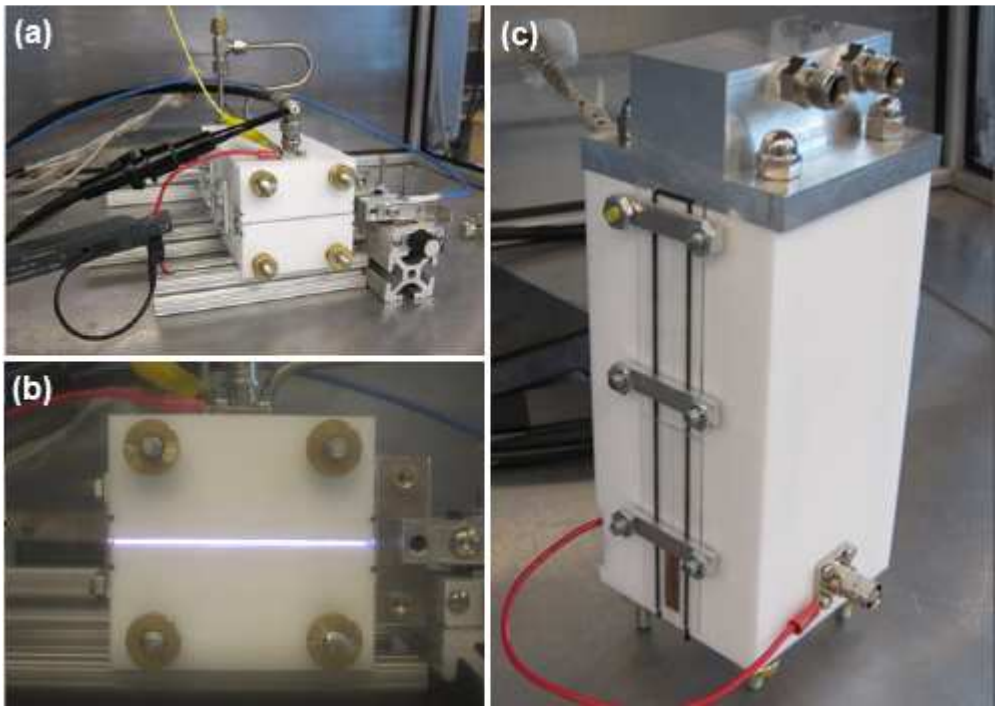

Figure 8. A proposed linear plasma head: (a) the unit ready for testing, (b) the unit generating helium-based plasma, (c) general design of the unit

Figure 8 represents the proposed linear plasma head. Image (a) shows the assembled plasma head prepared for experimental evaluations. The white Teflon walls are assembled with a thin gap between them. The gap forms a channel for the flow of neutral gas. Electrodes are placed about 1 cm before the outlet. Image (b) shows the plasma head at work, generating helium-based plasma, which can be seen in the channel between the walls. Image (c) shows the general view of the plasma head, with the top chamber providing connectors for neutral gas and uniformly distributing the gas at the channel inlet. The sides of the head are covered with quartz glass with an intension of optical analysis of the plasma bulk and sheath. For instance, the

plasma content can be accurately investigated with optical spectrometry, as it was done in the work of Lepkojus et al.[46] for Helium-based plasmas. Some other methods of optical characterization of plasmas, like laser-induced fluorescence, spontaneous and stimulated Raman, and multi-photon spectroscopy [17] are viable options as well .On the right bottom side there is a BNC connector to supply AC current to the electrodes.

The experimental investigation of the plasma head included tests with different plasma regimes, in particular, dependence between electrical input and α/γ -modes of plasma operation was explored, as well as voltage-current characteristics were recorded in order to determine the power efficiency of the setup. A total gas flow of 10-40 liters per minute (LPM) was assumed for these preliminary examinations. The plasma electrodes had the following size: the length is 2.54 cm and the width is 7.6 cm with inter-electrode spacing of 1 mm. The gap between the electrodes is designed to be adjustable, in order to accommodate different experimental settings.

Two designs for injection units were tested with the linear plasma head. The first design featured an injection unit for sidewise injection of chemicals. The injection was perpendicular to the flow of plasma. The interaction between plasma and chemical precursor was poor, mainly due to inability of the chemical flow to penetrate to the central portion of the plasma stream – the part of the plasma with the most active species. The deposition results (Figure 9.(a)) appear scattered with quality of the coating strongly dependent on the strength of coupling between chemical precursor and plasma species.

As a result of this test the location of the injectors was changed, leading to the second design concept. The concept assumes the injector to be in a form of a thin plate that is installed between electrodes, splitting the flow of neutral gas into two portions – above the injector and below the injector. As the further improvement of the design, the plate was proposed to be

conductive and to serve as a third electrode with plasma generation above the injector and below the injector and chemicals injection between two plasma “blades”.

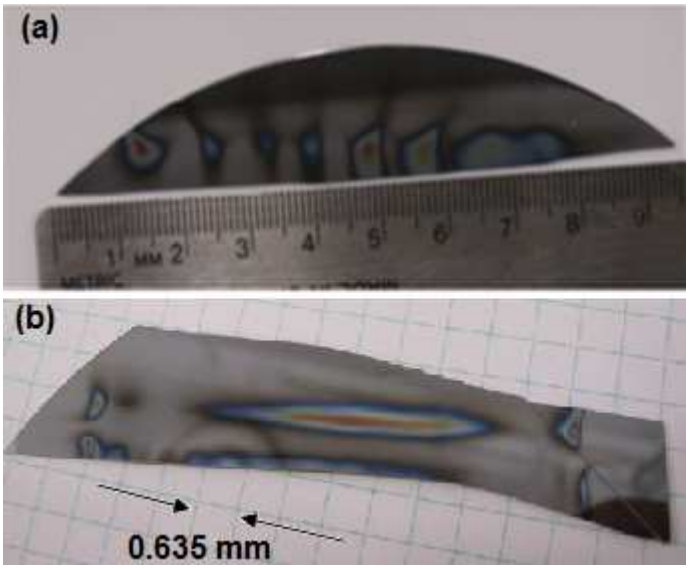

Figure 9. Coating formation on the c-Si substrate: (a) with side injection (b) with injection to the centerline of plasma stream

Deposition made with the second design is shown in Figure 9.(b). As it can be seen there are two lines of the modified precursor deposited on the c-Si substrate. The uniformity of the deposition is improved in comparison to the unit with sidewise injection. At the same time, the quality of the deposition (indicated by color change of the coating on the substrate) was not very high. This result was explained with fluidic modeling of two immiscible liquids using the geometry of the plasma head.

Figure 10 shows a calculation domain for simulation of mixing for two fluids. The simulation is done with ANSYS CFX. The horizontal portion of the domain represents a channel between two parallel sides of the head. The open body at the center of the channel is a flat injector, which serves as the third electrode. On the right side of the injector, there is an injection port; it has a shape of a slot in 3D; in the attempted 2D simulation, the injector is represented by

a thin channel, as it can be seen on the right side of the left image in Figure 10. Plasma electrical properties are not taken into account in this simulation; we focused on fluidic properties only.

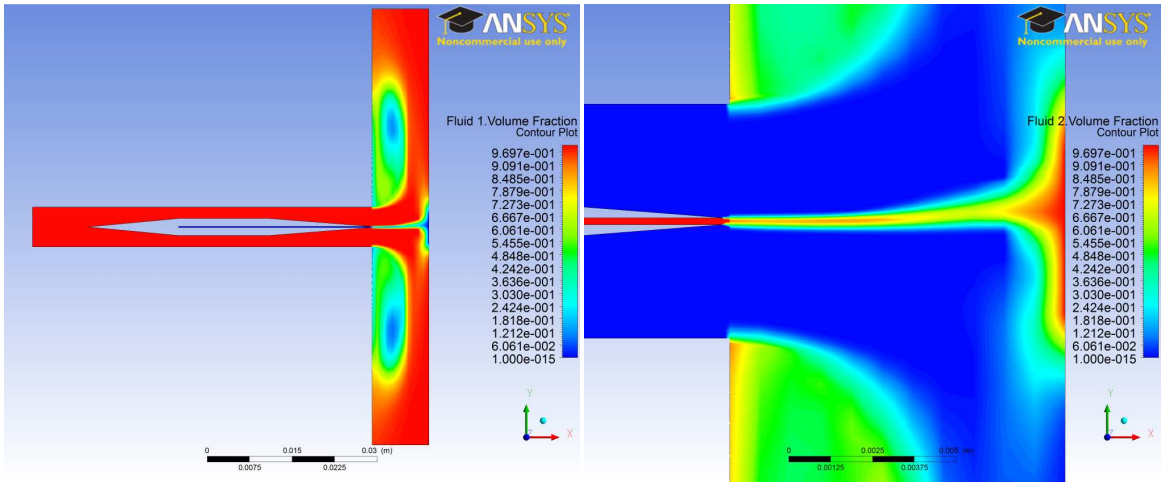

Figure 10. Computational domain for simulation of mixing of plasma-gas and injected chemical precursor. The left image shows volume fraction of plasma gas, the right image shows volume fraction of the chemical precursor

The right image in Figure 10 represents volume fraction of a gas substituting plasma with red being the highest concentration. The figure shows the second fluid – chemical precursor – which is injected from the injector body into the spacing between two streams of plasma-gas. In the original design we expected efficient mixing of the two fluids. The simulation shows that the central portion of the precursor did not engage with the plasma, only edges of the stream come into interaction and become modified. The modified precursor may be seen as yellow-green portion of the precursor stream. Since unmodified precursor does not attach to the substrate well enough and does not leave distinguishable coating, we can visually examine only those areas of the substrate that are covered with modified precursor (the yellow-green region at the substrate in Figure 10). According to simulation results, the examined concept of the plasma head would produce two parallel coated lines on the substrate. This result we found in the actual sample (Figure 9.(b)).

Fluidic simulation proves to be a useful tool for analysis of material deposition with APP. At the same time, the information on distribution of fluids is not sufficient to estimate the final results. In addition to fluidic investigation, we have to add distribution of plasma species in the flow, as well as their interaction with chemical precursor and, more important, distribution of modified precursor in the stream of plasma product, especially in the vicinity of the substrate. This knowledge would allow us to estimate concentration of material that is ready for deposition. Simulation of surface chemistry could provide probabilistic approach to the actual distribution of the modified precursor, based on physical and chemical properties of the substrate material. Investigation of plasma behavior in the flow of a neutral gas was started in order to answer these questions.

MODEL OF PLASMA GENERATION

Theoretical Model

General Description

Experimental evaluation of a plasma system is an intriguing task, especially when such parameters as electron energy distribution function (EEDF) [47] or species density and velocity are in question. In order to deeply examine the system, we perform theoretical and numerical modeling. It not only provides the properties of interest, but also allows us to predict plasma behavior when we change a certain parameter and determine the optimal range for the system operation.

The general approaches to model plasma behavior are Molecular Dynamics, Fluidic Theory, and Kinetic Theory. Molecular Dynamics is well suitable for plasma problems at small scales, especially when the problem may be resolved by tracking a small number of separate particles. When the number of particles increases, but still is low for continuous approaches, Particle-in-Cell technique comes into use; it tracks small volumes that contain a number of separate particles, using electromagnetic equations to resolve the dynamics of the volumes. The Fluidic Theory relies on a continuous definition of plasma density, species velocity, temperature, and other physical parameters. Fluidic Theory usually assumes that the energy of electrons follows a Maxwellian distribution; hence, the accuracy of this theory is generally an issue. This issue is resolved by introduction of the Boltzmann electron energy distribution function. In the general case, this approach is applied in Kinetic Theory, where species properties are functions of time, spatial coordinates, and velocity coordinates. Even though Kinetic Theory is the most accurate of continuous methods, its evaluation is associated with significant computational

overhead; this is why a compromise solution of a hybrid Fluidic/Kinetic model was devised. The hybrid model utilizes an approach of the Fluidic model at the same time featuring EEDF and rate parameters typical for Kinetic model. This model is used in our simulation and is thoroughly discussed in this work.

The theoretical model of plasma is qualitatively described in terms of governing equations and major derivations in such fundamental sources as [2] and [48]. Nevertheless, some details of this model are usually omitted in the literature under an assumption of their obvious nature. Thus, the current work pursues the following goals:

- Modeling of plasma generation in a capacitive RF discharge
- Estimation of convective plasma transport in a variety of geometrical configurations
- Explanation of some elementary plasma properties hardly available in the literature

In order to fulfill these goals, we consider a plasma reactor that has parallel arrangements of the electrodes (Figure 11). There are three sections distinguishable in the reactor: a generation chamber, a mixing chamber, and an open space between the reactor and a substrate.

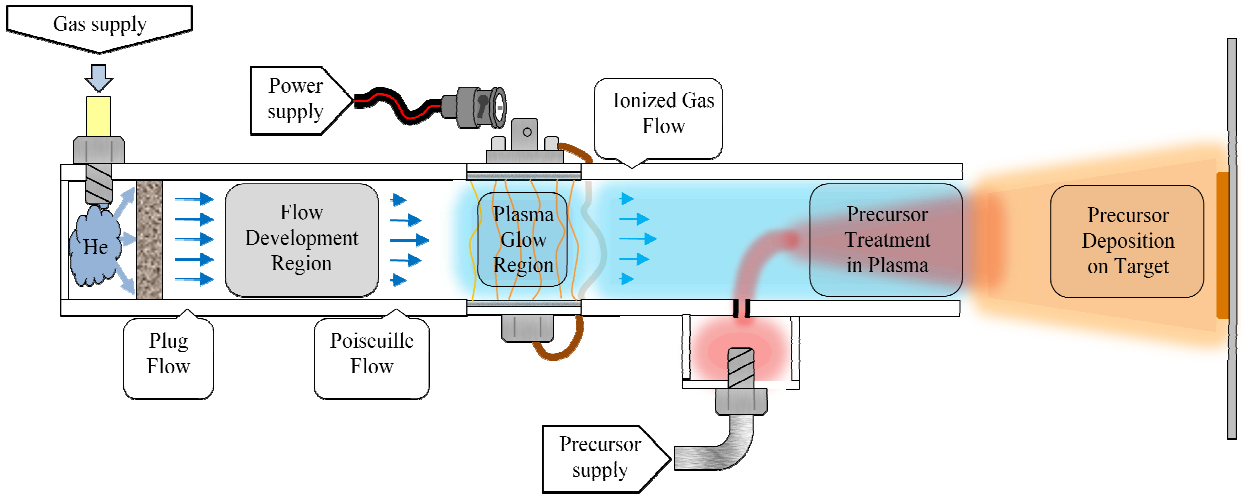

Figure 11. Schematics of plasma reactor

The plasma generation chamber consists of two parallel electrodes separated by a gap filled with carrier gas at atmospheric pressure. The electrodes are connected to the AC power source. It is possible to include the dielectric boundary layer for electrodes, even though it affects the gas breakdown [49]. The dimensions of the electrodes are sufficiently larger than the gap size; hence, we assume that the model can be converted to 1D where a computational domain is represented by the shortest line connecting two parallel electrodes. The characteristic times of plasma generation $\left(t_{gen} = 1/13.56\ \text{MHz} \approx 7.4\times10^{-8}\ \text{s}\right)$ and characteristic time of carrier gas flow $\left(t_{flow} = 0.0254\ \text{m}/10\ \text{m/s} \approx 2.54\times10^{-3}\ \text{s}\right)$ differ by four orders of magnitude $\left(t_{flow}/t_{gen} = 3.4\times10^{4}\right)$, with the plasma generation time being the smallest (here we assume the electrode dimensions of $2.54\text{cm}\times2.54\text{cm}$ and gas mean velocity $10\ \text{m/s}$). Such a difference allows us to neglect the plasma advection effects along the channel and focus primarily on plasma distribution within the 1D domain. We also neglect edge effects of the electric field and changes in temperature of the carrier gas, which is kept constantly at 300 K. The influence of the magnetic field is usually assumed to be negligible for this type of problems [43].

We employ fluidic theory as the main approach to modeling plasma behavior. This approach provides results with accuracy comparable to that of kinetic models [50]. It is an intuitively appealing method with parameters that are easy to measure experimentally, in opposition to experimental investigations of EEDF which is the main component of the kinetic theory. Kinetic models provide too much information that unnecessarily raises the requirements for the computing environment [51]. Fluidic models work with only three spatial dimensions instead of the six spatial-velocity dimensions of kinetic models, which is extremely advantageous for computation process. As the 2D model of the LAPPD head bears fluidic

features, it is natural to use fluidic approach for 1D plasma generation as a part of the larger model.

The atmospheric pressure plasma is characterized by low overall temperature, usually in the range of 300-1000 K; at the same time its species carry high energy content. Such occurrence is possible due to the significant difference in size of electrons and ions in the plasma. According to Suplee et al [52], the average ion size is 2000 times larger than that of an electron. The size of the species determines their mobility in an electric field, as well as their acceleration and inertia. Smaller electrons are easier to accelerate: they reach high velocities (200 times higher than ions, according to our observations) which is an indication of the electrons' high kinetic energy. This energy is expressed in terms of temperature of the species and reaches 5-6 eV for electrons (1 eV corresponds to 11605 K), while the helium ions temperature is close to the room value of 300 K. The fluidic model essentially contains two temperature/energy levels [37]; therefore, both types of species have to be modeled separately.

We do not include negative helium ions in our model as they are extremely hard to achieve. Researchers [20-22] have to utilize a special technique at high vacuum with energies of the species in the range of 3-70 keV, in order to create the negative ions [21, 22]. Even at high vacuum the yield of He^- is measured as 1.2% of that of He^+ [21], with a lifetime in the order of 10^{-5} s. In atmospheric pressure plasma the lifetime of these species would be significantly shorter with much lower yield due to the shorter mean free path. Thus, we exclude He^- from our model.

A dramatic difference in velocities between ions and electrons in APP determines its non-equilibrium state. Under such circumstances, EEDF based on a Maxwellian distribution cannot properly describe plasma kinetics. In fact, Meyyappan et al. [53] mention that Maxwellian EEDF

provides overestimated rate constants and plasma density, in comparison to Boltzmann-based EEDF. This fact clarifies the use of rate constants based on Boltzmann EEDF in our model.

Governing Equations

Following the general approach [2, 43, 48] we consider moments of Boltzmann equation (8) in order to build a set of governing equations. Boltzmann equation, being fundamental for plasmas, is not solved directly in our model. Instead, we make a connection to kinetic effects through the use of rate constants.

$$\frac{df}{dt} = \frac{\partial f}{\partial t} + \mathbf{v} \cdot \nabla_r f + \frac{\mathbf{F}}{m} \cdot \nabla_v f = \left(\frac{\partial f}{\partial t} \right)_c \tag{8}$$

In this equation, f stands for EEDF, t is time, $\bar{v}$ is velocity of species, $\mathbf{F}$ is a force acting on the species, m is the species mass, and $\left(\frac{\partial f}{\partial t} \right)_c$ is a collision term. The number of particles in the vicinity of the point $(\mathbf{x}, \mathbf{v})$ with spatial coordinates in the range of $(\mathbf{x}, \mathbf{x} + d\mathbf{x})$ and velocity coordinates in the range of $(\mathbf{v}, \mathbf{v} + d\mathbf{v})$ is described by the following relation

$$f(t, \mathbf{x}, \mathbf{v}) d\mathbf{x} d\mathbf{v} \tag{9}$$

The number density of the species can be found by averaging the EEDF over velocity space

$$n(t, \mathbf{x}) = \int f(t, \mathbf{x}, \mathbf{v}) d\mathbf{v} \tag{10}$$

Any velocity moment $\Phi(\mathbf{v})$ may be averaged to the mean value using the integration over velocity space

$$\langle \Phi(\mathbf{v}) \rangle = \frac{1}{n(t, \mathbf{x})} \int \Phi(\mathbf{v}) f(t, \mathbf{x}, \mathbf{v}) d\mathbf{v} \tag{11}$$

The momentum of the flow dyad Π_{ij} is defined through the second order momentum of the EEDF

$$\Pi_{ij} = m\int \Phi(\mathbf{v}) f(t,\mathbf{x},\mathbf{v}) v_i v_j d\mathbf{v} = mn\langle v_i v_j \rangle$$

$$\Pi_{ij} = mnu_i u_j + P_{ij} \tag{12}$$

In this equation u_i, u_j are the components of the mean velocity $u_i(t,\mathbf{x})$, m is the mass of the specie, and P_{ij} is the component of pressure tensor.

We calculate the first three moments of the Boltzmann equation to form a fluidic representation of plasma. Very detailed derivation of the moments can be found in [2, 48]. We follow [54] in order to find the moments. Boltzmann equation may be multiplied by some function $\Phi(\mathbf{v})$ and integrated with respect to velocity components

$$\int \frac{\partial f}{\partial t}\Phi d\mathbf{v} + \int \mathbf{v}\cdot\nabla_r f\,\Phi d\mathbf{v} + \int \frac{\mathbf{F}}{m}\cdot\nabla_v f\,\Phi d\mathbf{v} = \int \left(\frac{\partial f}{\partial t}\right)_c \Phi d\mathbf{v} \tag{13}$$

Because the first term on the left-hand side does not depend on x or t, the order of integration and differentiation could be exchanged. The integration is carried out using the average value $\langle\Phi(\mathbf{v})\rangle$ of function $\Phi(\mathbf{v})$.

$$\int \frac{\partial f}{\partial t}\Phi d\mathbf{v} = \int \frac{\partial(\Phi f)}{\partial t} d\mathbf{v} = \frac{\partial(n\langle\Phi\rangle)}{\partial t} \tag{14}$$

The second component on the left-hand side is the subject to similar approach

$$\int \mathbf{v}\cdot\nabla_r f\,\Phi d\mathbf{v} = \int v_i \cdot \frac{\partial}{\partial x_i}(\Phi f) d\mathbf{v} == \int \frac{\partial}{\partial x_i}(\Phi v_i f) d\mathbf{v} = \nabla_r\left(n\langle\Phi\mathbf{v}\rangle\right) \tag{15}$$

The third term on the left hand side represents force exerted on particles. We assume that EEDF rapidly decreases when the velocity of the particles approaches infinity. This assumption sets the modified integral of the term to zero with only the second term having non-zero value. We also assume that $\mathbf{F}$ is divergence free with respect to velocity, this allows bringing the components of

the force vector under the differential with respect to velocity. The last assumption is suitable for the electromagnetic force. With all the mentioned assumptions, the term modifies as follows

$$\int \frac{\mathbf{F}}{m} \cdot \nabla_v f \, \Phi d\mathbf{v} = \frac{1}{m} \int \left(\frac{\partial}{\partial v_i} F_i f \, \Phi \right) d\mathbf{v} - \frac{n}{m} \left\langle F_i \frac{\partial \Phi}{\partial v_i} \right\rangle = -\frac{n}{m} \left\langle F_i \nabla_v \Phi \right\rangle \tag{16}$$

The integrated collision term $I_c(t,x)$ becomes a function of time and space coordinates only, this is why it modifies in the following way

$$\int \left(\frac{\partial f}{\partial t} \right)_c \Phi d\mathbf{v} = \left(\frac{\partial \left(n \langle \Phi \rangle \right)}{\partial t} \right)_c \tag{17}$$

We combine the integrated terms into a general form of a moment of Boltzmann equation

$$\frac{\partial \left(n \langle \Phi \rangle \right)}{\partial t} + \nabla_r \left(n \langle \Phi \mathbf{v} \rangle \right) - \frac{n}{m} \left\langle F_i \nabla_v \Phi \right\rangle = \left(\frac{\partial \left(n \langle \Phi \rangle \right)}{\partial t} \right)_c \tag{18}$$

We would like to derive the moments of Boltzmann equation. Since the considered problem is 1D, we switch from the general form of the equation to particular vector components. The first moment of the Boltzmann equation is the continuity equation, it can be derived setting $\Phi = 1$

$$\frac{\partial \left(n \langle 1 \rangle \right)}{\partial t} + \frac{\partial}{\partial x} \left(n \langle v \rangle \right) - \frac{n}{m} \left\langle F_i \frac{\partial (1)}{\partial v} \right\rangle = \left(\frac{\partial \left(n \langle 1 \rangle \right)}{\partial t} \right)_c$$

$$\frac{\partial n}{\partial t} + \frac{\partial}{\partial x} \left(nu \right) = \left(\frac{\partial n}{\partial t} \right)_c \tag{19}$$

We write this equation for the species *I*, and substitute the collision term on the right-hand side with a sum of separate effects of ionization and recombination processes.

$$\frac{\partial n_i}{\partial t} + \frac{\partial}{\partial x} \left(n_i v_i \right) = \sum_j R_{ij} \tag{20}$$

The second moment of Boltzmann equation is conservation of momentum, it can be derived setting $\Phi = m\mathbf{v}$

$$\frac{\partial\left(n\left\langle mv\right\rangle\right)}{\partial t}+\frac{\partial}{\partial x}\left(n\left\langle mv^2\right\rangle\right)-\frac{n}{m}\left\langle F_i\frac{\partial(mv)}{\partial v}\right\rangle=\left(\frac{\partial\left(n\left\langle mv\right\rangle\right)}{\partial t}\right)_c$$

$$\frac{\partial(nmu)}{\partial t}+\frac{\partial\Pi_{ij}}{\partial x}-n\left\langle F_i\right\rangle=\left(\frac{\partial(nmu)}{\partial t}\right)_c$$

$$\frac{\partial(nmu)}{\partial t}+\frac{\partial mnu_iu_j}{\partial x}=-\frac{\partial P_{ij}}{\partial x}+n\left\langle F_i\right\rangle+\left(\frac{\partial(nmu)}{\partial t}\right)_c \tag{21}$$

$$\frac{\partial\left(n_im_iv_i\right)}{\partial t}+\frac{\partial}{\partial x}\left(n_im_iv_iv_i\right)=-\frac{\partial P_i}{\partial x}+q_in_iE-n_im_iv_iv_i$$

The third moment of Boltzmann equation describes conservation of energy. It can be derived setting $\Phi=m\mathbf{v}^2/2$

$$\frac{\partial\left(n\left\langle mv^2/2\right\rangle\right)}{\partial t}+\frac{\partial}{\partial x}\left(n\left\langle mv^3/2\right\rangle\right)-\frac{n}{m}\left\langle F_i\frac{\partial\left(mv^2/2\right)}{\partial v}\right\rangle=\left(\frac{\partial\left(n\left\langle mv^2/2\right\rangle\right)}{\partial t}\right)_C \tag{22}$$

Define the following entities

$$\left\langle v^2\right\rangle=u^2+\frac{3p}{mn}\qquad\left\langle v_iv^2\right\rangle=u^2u_i+\frac{3p}{mn}u_i+\frac{2}{mn}P_{ij}u_i+\frac{2}{mn}q_i \tag{23}$$

Here p is scalar pressure, q_i is heat flux. Substitute the entities into (22)

$$\frac{1}{2}\frac{\partial\left(mn\left\langle u^2+\frac{3p}{mn}\right\rangle\right)}{\partial t}+\frac{1}{2}\frac{\partial}{\partial x}\left(mn\left(u^2u_i+\frac{3p}{mn}u_i+\frac{2}{mn}P_{ij}u_i+\frac{2}{mn}q_i\right)\right)-\frac{n}{m}\left\langle F_i\frac{\partial\left(mv^2/2\right)}{\partial v}\right\rangle=\left(\frac{\partial\left(mn\left\langle u^2+\frac{3p}{mn}\right\rangle\right)}{\partial t}\right)_C$$

$$\frac{\partial\left(mnu^2\right)}{\partial t}+3\frac{\partial p}{\partial t}+\frac{\partial}{\partial x}\left(mnu^2u_i+3pu_i+2P_{ij}u_i+2q_i\right)-2nF_iu=\left(\frac{\partial\left(mnu^2+3p\right)}{\partial t}\right)_C \tag{24}$$

$$\frac{\partial\left(mnu^2\right)}{\partial t}+\frac{\partial\left(mnu^2u_i\right)}{\partial x}+3\frac{\partial\left(pu_i\right)}{\partial x}+2\frac{\partial\left(P_{ij}u_i\right)}{\partial x}+2\frac{\partial q_i}{\partial x}+3\frac{\partial p}{\partial t}-2nF_iu=\left(\frac{\partial\left(mnu^2+3p\right)}{\partial t}\right)_C$$

Denote kinetic energy of species *i* as $\omega_i=mn_iu^2/2$

$$\frac{\partial \omega_i}{\partial t}+\frac{\partial(\omega_i u_i)}{\partial x}+\frac{3}{2}\frac{\partial(pu_i)}{\partial x}+\frac{\partial(P_{ij}u_i)}{\partial x}+\frac{\partial q_i}{\partial x}+\frac{3}{2}\frac{\partial p}{\partial t}-nF_i u=\frac{1}{2}\left(\frac{\partial(mnu^2+3p)}{\partial t}\right)_C \tag{25}$$

We use $F_i = q_i E$ and Hooks law $q_i = -K_i \frac{\partial T}{\partial x}$

$$\frac{\partial \omega_i}{\partial t}+\frac{\partial(\omega_i u_i)}{\partial x}=-\frac{\partial(P_{ij}u_i)}{\partial x}+nuq_i E+\frac{\partial}{\partial x}\left(K_i\frac{\partial T_i}{\partial x}\right)-\frac{3}{2}\frac{\partial(pu_i)}{\partial x}-\frac{3}{2}\frac{\partial p}{\partial t}+\frac{1}{2}\left(\frac{\partial(mnu^2+3p)}{\partial t}\right)_C \tag{26}$$

The last three terms on the right are represented as a sum of energy rate terms

$$\frac{\partial \omega_i}{\partial t}+\frac{\partial}{\partial x}(\omega_i v_i)=-\frac{\partial}{\partial x}(P_i v_i)+q_i n_i v_i E+\frac{\partial}{\partial x}(K_i \nabla T_i)-\sum_j R_{ij}H_j \tag{27}$$

The moments are written for the species i, where i indicates electrons or positive helium ions. The n_i stands for number density of the species, x is a spatial coordinate, v_i is velocity of the species, $\sum_j R_{ij}$ is a generation/recombination term, P_i is partial pressure of the species, q_i is the sign of the species charge, E is electric field, ω_i is the species kinetic energy, T_i is temperature of the species, K_i is thermal conductivity of the species, and $\sum_j R_{ij}H_j$ is energy rate term. Since our problem is one-dimensional, in (20)-(27) we used only first components of the vector terms.

The moment (20) is an essential equation for the species distribution. The moment (21) is required for coupling of the species' velocity and number density. We follow an approach of [43, 45, 50, 55], introducing the drift-diffusion approximation (28) to our model. This approximation renders useless the moment (21), as the coupling between number density of species and their velocity is conveniently represented in the form of flux.

The drift-diffusion approximation is written in terms of species flux, according to [50]. The flux is formulated with drift (due to force provided by electric field) and diffusion (due to number density gradient) terms.

$$J = nv = sign(q)\mu nE - D\nabla n \tag{28}$$

Here μ is the mobility in $\left[\frac{m^2}{V.s}\right]$ and D is the diffusivity in $\left[\frac{m^2}{s}\right]$. Usually a ratio of electrons' diffusion to mobility is found from the Townsend experiment. Electrons motion is analyzed in an evacuated tube, where electrons are emitted from a source and their radial distribution is measured at certain distance from the emitter [56]. Diffusive flux of electrons is found from Fick's law by substitution of diffusion coefficient, electrons charge, and gradient of the number density

$$J_{diff} = -(-e)D\frac{dn}{dx} = D_e\nabla n_e \tag{29}$$

When an electric field is applied to a conducting media, the charge carriers move at a velocity that is proportional to the magnitude of the field. This velocity is called the drift velocity

$$v_d = \mu \cdot E \tag{30}$$

This definition is used to constitute drift current due to applied electric field

$$J_{drift} = v_d n_e e \tag{31}$$

At the equilibrium drift current and electrons diffusion are equal

$$J_{drift} = J_{diff} \tag{32}$$

At non-equilibrium conditions their superposition yields the total electrons' flux

$$J = n_e v_e = v_d n_e - D_e\nabla n_e \tag{33}$$

$$n_i v_i = n_i v_i^d - \frac{\partial}{\partial x}\left(n_i D_i\right) \qquad v_i^d = q_i \mu_i E \qquad q_i = \begin{cases} -1, \text{for e}^- \\ +1, \text{for He}^+ \end{cases} \tag{34}$$

Equation (34) contains a drift term (the first term on the right-hand side) with drift velocity v_i^d (where μ_i denotes the species mobility) and diffusion term (the 2nd term on the right hand side) with a diffusion coefficient D_i.

Since ions are bulky and slow, they cannot efficiently diffuse in the time-frame of one RF-oscillation; therefore, the diffusion term for ions is negligibly small and omitted in our simulation [43]. The drift-diffusion approximation (34) substitutes into the mass conservation equation (20) modifying its second term on the left-hand side

$$\frac{\partial n_i}{\partial t} + \frac{\partial}{\partial x}\left(n_i v_i^d - \frac{\partial}{\partial x}\left(n_i D_i\right)\right) = \sum_j R_{ij} \tag{35}$$

Mobility, diffusion, and generation/recombination rates are determined based on values of the local electric field. Even though there are methods to avoid solution of Poisson equation [57], we use the classic approach. The electric field is calculated by means of Poisson equation (36). There is a cloud of charged particles between the electrodes that distort the external electric field generated by electric potential $U\cos(\omega t)$. The right-hand side of (36) accounts for an impact of each particular charge to properly estimate the distortion.

$$\nabla^2 \phi = -\frac{e}{\varepsilon_0}\left(n_p - n_e\right) \qquad E = -\frac{\partial \phi}{\partial x} \tag{36}$$

In this equation, ϕ is an electric potential, $e = 1.6 \times 10^{-19}$ C is elementary charge, and $\varepsilon_0 = 8.85 \times 10^{-14}$ C/V·cm is vacuum permittivity constant.

The Poisson equation has a simple form in the 1D case. This is why we directly integrate it in (37), following [43] and [58]. The right-hand side integral in (37) represents the

accumulated field distortion that compliments to the external electric field to yield the local value of $E(x)$.

$$E(x) = E_0 + \frac{e}{\varepsilon_0}\int_0^x \left(n_p(\xi) - n_e(\xi) - n_n(\xi)\right)d\xi \tag{37}$$

E_0 is a constant of integration that is determined from the boundary condition (38). The boundary condition binds the electric field at the domain and the voltage (U) externally applied to the electrodes.

$$\int_0^L E(x)dx = -U\cos(\omega t) \tag{38}$$

The common definition of plasma assumes that its total charge is somewhat neutral. In reality, the charge of APP could be slightly offset. The boundary condition (38) has to account for non-neutral charge of APP which is done by an integral term $\tilde{I}$ in the expanded form of the boundary condition (39). This elementary fact is usually not mentioned in the literature, though it is crucial for accurate modeling of plasma.

$$\int_0^L E(x)dx = E_0 L + \int_0^L \left[\frac{e}{\varepsilon_0}\int_0^x \left(n_p(\xi) - n_e(\xi) - n_n(\xi)\right)d\xi\right]dx =$$
$$= E_0 L + \tilde{I} = -U_0\cos(\omega t)$$

$$E_0 = -\frac{1}{L}\left(U\cos(\omega t) + \tilde{I}\right) \tag{39}$$

The parameter L in (39) stands for the gap size.

In our model, we employ the concept of the Local Field Approximation (LFA). It assumes that all plasma parameters depend on locally calculated reduced electric field E/N, with number density of neutral gas $N = 2.6871\times10^{19}\ \mathrm{cm}^{-3}$. This assumption allows us to use rate

coefficients based on solution of the Boltzmann equation from the kinetic approach [45]. LFA is not very applicable in the cathode fall region of plasma [58]; nevertheless, it is common practice to apply the concept over the whole domain, as the error is usually negligible.

The system of the governing equations (40) is formed of modified mass conservation equations (35), written for each of the species separately, and integrated Poisson equation (37) which connects the plasma charge distribution to the electric field

$$\begin{aligned}
&\frac{\partial n_e}{\partial t}+\frac{\partial}{\partial x}\left(\mu_e E n_e-D_e\frac{\partial n_e}{\partial x}\right)=(\alpha-\eta)n_e\left|v_e^d\right|-k_{ie}^{rec}n_e n_p\\
&\frac{\partial n_p}{\partial t}+\frac{\partial}{\partial x}\left(\mu_p E n_p\right)=\alpha n_e\left|v_e^d\right|-k_{ie}^{rec}n_e n_p\\
&E(x)=E_0+\frac{e}{\varepsilon_0}\int_0^x\left(n_p(\xi)-n_e(\xi)-n_n(\xi)\right)d\xi
\end{aligned} \tag{40}$$

The general form of the collision term $\sum_j R_{ij}$ on the right-hand side of (35) is expanded in (40) with species generation (the first) and recombination (the second) terms. The ionization parameter (α), the electric mobility (μ_e, μ_p), and the diffusion coefficient (D_e) are functions of the local reduced electric field. In the ideal case, they have to be evaluated through experiment in Townsend discharge tube [59]. We simplify the parameters evaluation and calculate them over EEDF that is provided from the solution of the Boltzmann equation. The solution technique for the Boltzmann equation requires deep insight into electrons interactions [60-62]. We do not attempt such a detailed investigation, instead, we use a freeware package the BOLSIG+ [63] that solves the Boltzmann equation for special cases, calculates EEDF, and derives rate parameters, which are used in our model.

Rate Parameters

We provide an example of rate parameters derivation using the BOLSIG+ package. As an input, the BOLSIG+ requires cross-sections of collision events for the gas of interest, physical conditions of simulation (such as temperature of the gas, electric field values etc.), and parameters controlling the numerical process of simulation. We use cross-sections for helium gas that are provided in the package by default. For the "New Run" we choose "Linear E/N (Td)" option where the initial (1 Td) and the final (100 Td) values are specified. The number of runs is set to 100 and temperature of neutral gas to 300 K. In the "Numerics" section the number of energy levels is changed to 500, as it provides smooth and accurate result. The rest of the options are left at their default values. The output data is saved as "Separate tables vs. E/N". We assemble a table of the rate data in a spreadsheet processing package. All the parameters in the output file have self-explanatory names, except for the ionization coefficient which is referred to as "C9 He Ionization 24.58 eV; Townsend coefficient / N (m2)".

On a request, the BOLSIG+ fits most of the output variables with a polynomial; this option has to be selected when saving the data-file. As an example, the fit data provide non-zero ionization values for a low (less than 5 Td) reduced electric field, whereas the original data contain zero in these positions. We found that use of the fit data (ionization fit data is shown in Appendix A for $E/N < 5$) improves the plasma stability at low external voltage *U*, as well as in the region of weak electric field. Appendix A contains an example of typical data retrieved from the BOLSIG+ and used in our model.

Figure 12 represents the behavior of typical rate parameters which are converted into a suitable form used in our model. The mobility plot (Figure 12.(c)) includes ions' data in addition to that of electrons'. As it can be seen from this plot, the mobility of electrons and ions has two

orders of magnitude difference. This happens because of the larger size of ions which leads to lower drift velocity, according to (34). For He+ ions the rate parameters are taken from atomic data tables [64], where experimentally acquired ions mobility μ_p is represented as a function of reduced electric field E/N. These data are presented in Appendix B.

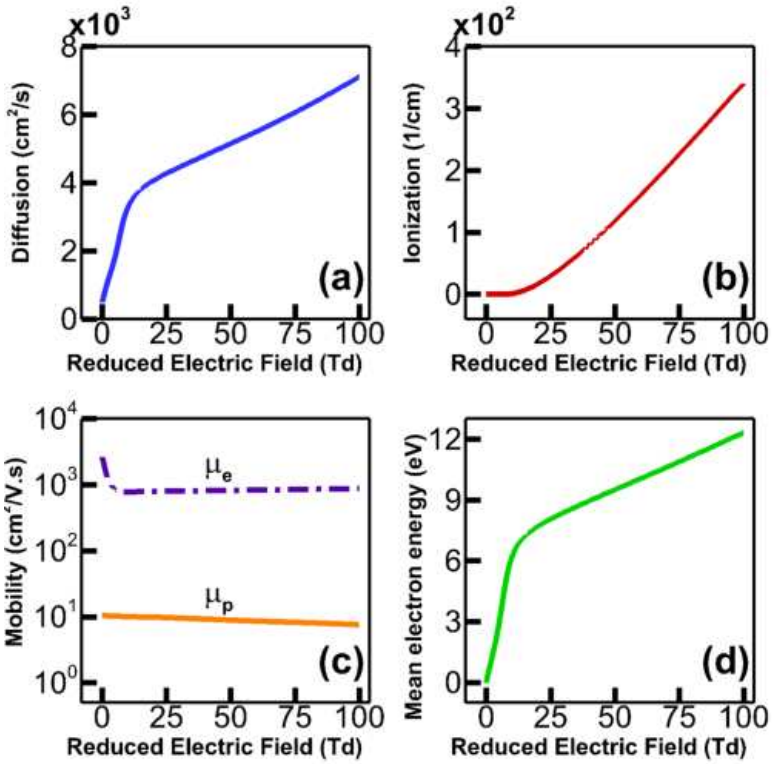

Figure 12. Typical rate parameters used in the model: (a) e^- diffusion (D_e), cm^2/s; (b) helium ionization (α), 1/cm; (c) e^- and He^+ mobility (μ_e, μ_p), $cm^2/V.s$; (d) e^- mean energy (ω_{mean}), eV. The horizontal axis shows reduced electric field (E/N), Td

The rate coefficients found from BOLSIG+ and atomic data tables are crucial for modeling generation, drift and diffusion processes. The recombination process calls for a recombination constant k_{ie} which is responsible for loss of species due to interactions between electrons and ions (as well as interactions between positive and negative ions, when the later are

present). In our model, the recombination coefficient is set to $k_{ie} = 10^{-7}\ \mathrm{cm}^3/\mathrm{s}$ and kept constant throughout the simulation [43], [58].

The rate parameters estimated in this section allows us to cover a wide range of possible interactions between helium and electrons. A set of such interactions could be found in Kong and Deng work [65].

Boundary Conditions

The boundary conditions for the system (40) are specified in terms of fluxes. Following the general approach [43, 45, 58], electrons are allowed to penetrate the electrodes without a reflection. The equivalent notations for this condition would be “perfect absorption” [43] or “zero reflection coefficient” [50]; Wester et al [58] also mention recombination of electrons with the material of the electrodes. The flux of electrons at the boundary is formed by the drift-diffusion process and thermal motion of electrons due to their high kinetic energy. The thermal flux is significantly larger than drift-diffusion flux [43], therefore we ignore the latter and specify electrons flux (41) through thermal motion only.

$$j_e = \begin{cases} -\dfrac{v_e^{kinetic} n_e}{4}, x = 0 \\ +\dfrac{v_e^{kinetic} n_e}{4}, x = L \end{cases} \tag{41}$$

Kinetic velocity of electrons $v_e^{kinetic}$ is determined through the electrons’ energy. Among the rate coefficients, the BOLSIG+ provides mean electron energy ω_{mean} (last column of the table in Appendix A). Temperature of electrons is estimated as $T_e = 2\omega_{mean}/3k_B^{eV}$ [6], with $k_B^{eV} = 8.617\times10^{-5}\ \mathrm{eV/K}$ being the Boltzmann constant. This data is tabulated for a range of reduced electric field. Kinetic velocity is calculated as $v_e^{kinetic} = \sqrt{8k_B^J T_e/\pi m_e}$, with

$m_e = 9.1\times10^{-31}$ kg being a mass of an electron and $k_B^J = 1.38\times10^{-23}$ J/K being the Boltzmann constant.

Let us estimate the difference between kinetic and drift velocities of electrons. As a reference, we assume reduced electric field value of $E/N = 1\,\mathrm{Td}$ with corresponding electric field $E = 26871\,\mathrm{V}$. Mean energy is $\omega_{mean} = 0.5641\,\mathrm{eV}$ (taken from Appendix A); electrons' temperature is $T_e \approx 4364\,\mathrm{K}$, and kinetic velocity is $v_e^{kinetic} \approx 410405\ \mathrm{m/s}$. Just for comparison, drift velocity (34) at the same conditions is $v_e^d \approx 4836\ \mathrm{m/s}$ - two orders of magnitude smaller than kinetic velocity. This is why kinetic flux of electrons is prevalent at the boundary.

In some cases, absolute absorption of electrodes allows number density to be set to zero at the boundary [45, 53]. We do not implement this additional condition, because kinetic flux alone is sufficient to keep electrons' number density at very low level in the vicinity of the electrodes. The secondary emission is often assumed negligible [66] for well-sustained glow discharges, thus we ignore its effect in this model.

For the positive ions, we specify only the drift flux towards the boundary (42). According to recent studies, helium ions are able to penetrate into the material of electrodes [67] and to become absorbed in this material [68]. In our model we do not account for such effect and use non-penetration condition for ions at the electrodes boundary. The drift flux of positive ions is reflected from the electrodes by the means of opposite fluxes specified at virtual nodes. The virtual fluxes have the same magnitude as the original ones, but the opposite direction. Such an approach results in zero total transfer of ions over the boundary.

$$j_p\big|_{x=0} = \begin{cases} v_p n_p & ,\text{if } v_p n_p < 0 \\ 0 & ,\text{if } v_p n_p > 0 \end{cases} \qquad j_p\big|_{x=L} = \begin{cases} v_p n_p & ,\text{if } v_p n_p > 0 \\ 0 & ,\text{if } v_p n_p < 0 \end{cases} \tag{42}$$

Physically, this process resembles the no-penetration condition for ions. A numerical scheme provides a connection between real and virtual fluxes at the boundary; this is why we do not specify additional details in this section.

Initial Conditions

The initial condition for the mass conservation equations is specified as a uniform distribution of the number density $\left(n_i = 10^{17}\ \mathrm{m}^{-3}\right)$over the computational domain. Number density is set to the same value for all the species, in order to maintain a neutral overall charge at the beginning of the calculation. The same type of initial condition is proposed by Young and Wu [45]. Meyyappan and Govindan [53] suggest the use of zero velocity and uniform mean energy, in addition to uniform number density distribution. We find this step excessive as species velocity and energy are unequivocally determined from the specified initial number density. The researchers also mention that the same converged solution can be obtained regardless of the initial condition. We could not confirm this statement in our tests. Additionally, in the Results and Discussion section, we discuss a range of parameters that lead to stable plasma generation. For initial conditions out of the range (specifically, for lower external voltage) we could not find stable plasma modes.

The initial distribution of the species over the domain affects the feasibility of the stable mode. If the species initially occupy only a part of the domain, the fast electrons are quickly lost into the nearest walls, leaving only the slow ions on the domain. The positive ions have no opportunity to decay as the electrons density becomes insufficient, because there is only one species generation mechanism through ionization supplied by electrons and the only loss mechanism through recombination with electrons. This case scenario has no interest for us. We also do not include field emission that could generate additional electrons to supplement an

avalanche process. Therefore, according to our observations, the only reasonable initial condition consists of uniform distribution of all the species with number density sufficient for starting the ionization process when electric field is applied.

Temperature and Energy Estimation

The third moment of Boltzmann equation (27) is used mainly for estimations of energy of the species and their temperature. The BOLSIG+ provides the mean energy of electrons (last column of the table in Appendix A) which allows the electrons temperature calculation. The temperature of the ions is changing slowly, responding to the time-averaged electric field. This is why, it is sufficient to calculate ions' temperature once per oscillation [43], solving heat diffusion equation (43).

$$k_{He}\frac{\partial^2 T}{\partial x^2} = -\frac{\omega}{2\pi}\int_{t}^{t+2\pi/\omega} j(\tau)E(\tau)d\tau \qquad (43)$$

In this equation, $k_{He} = 1.6\times10^{-4}\ \mathrm{W/cm\cdot K}$ is thermal conductivity of helium at standard temperature and pressure, $\omega = 13.56\,\mathrm{MHz}$ is frequency of alternating electric potential applied to the electrodes, and $j(t)$ is current density calculated as $j(t) = e\left(n_p v_p^d - n_e v_e^d\right)$ at a point *x*.

Since temperature and energy of the species are determined by workaround methods, the moment (5) can be excluded from further consideration. In the case of ions, the workaround method significantly improves the performance. Using the fact that rate parameters are calculated for constant temperature 300 K, the model does not catch the effect of temperature change of the neutral gas. Therefore, ions' temperature can be calculated only at the last oscillation, when plasma is in the steady mode.

Numerical Technique

In order to efficiently construct a numerical model, we perform undimensionalization of plasma parameters and properties. Some characteristic parameters are chosen based on geometry of the problem and physical properties of the setup. Thus, characteristic time $\hat{t}$ is the time required for one RF oscillation, characteristic electric potential is equal to the amplitude of the applied voltage $\hat{\varphi} = U_0$, and characteristic length is equal to the size of the gap $\hat{x} = L$. The other characteristic parameters are determined as derivatives of the defined ones.

We consider the continuity equation to find the characteristic parameter for number density of the species. The continuity equation for electrons is explored below. For positive ions all the derivations remain valid, yielding with similar result. This is why we do not show here derivations for the continuity equation of positive ions.

$$\frac{\partial n_e}{\partial t} + \frac{\partial}{\partial x}\left(\mu_e E n_e - D_e \frac{\partial n_e}{\partial x} \right) = (\alpha - \eta) n_e \left| v_e^d \right| - k_{ie}^{rec} n_e n_p$$

$$\frac{\hat{n}}{\hat{t}} \frac{\partial N_e}{\partial T} + \frac{1}{\hat{x}} \frac{\partial}{\partial X}\left(\frac{\hat{n}\hat{x}}{\hat{t}} N_e V_e^d - \frac{\hat{x}^2}{\hat{t}} \Lambda \frac{\hat{n}}{\hat{x}} \frac{\partial N_e}{\partial X} \right) = \frac{1}{\hat{x}} (\mathrm{A} - \Theta) \frac{\hat{n}\hat{x}}{\hat{t}} N_e \left| V_e^d \right| - \frac{1}{\hat{n}\hat{t}} K_{ie}^{rec} \hat{n}^2 N_e N_p$$

$$\frac{\partial N_e}{\partial T} + \frac{\partial}{\partial X}\left(N_e V_e^d - \Lambda \frac{\partial N_e}{\partial X} \right) = (\mathrm{A} - \Theta) N_e \left| V_e^d \right| - K_{ie}^{rec} N_e N_p \qquad (44)$$

Regardless the form of the characteristic number density, the continuity equations remain valid. Next, we explore Poisson equation.

$$\nabla^2 \phi = -\frac{e}{\varepsilon_0}\left(n_p - n_e \right)$$

$$\frac{\hat{\varphi}}{\hat{x}^2} \nabla^2 \Phi = -\frac{e}{\varepsilon_0} \hat{n} \left(N_p - N_e \right)$$

$$\nabla^2\Phi = -\frac{\hat{n}e\hat{x}^2}{\varepsilon_0\hat{\varphi}}\left(N_p - N_e\right) \tag{45}$$

The form of this equation can be simplified if we denote the characteristic number density as follows

$$\hat{n} = \frac{\varepsilon_0\hat{\varphi}}{e\hat{x}^2} = \frac{\varepsilon_0 U_0}{eL^2} \qquad \nabla^2\Phi = -\left(N_p - N_e\right) \tag{46}$$

We define characteristic electric field using known values for characteristic electric potential and characteristic length $\hat{E} = \hat{\varphi}/\hat{x} = U_0/L$. We also define characteristic current using a simple relation $\hat{j} = e\hat{n}\hat{v} = \varepsilon_0 U_0/\hat{t}L$. The last equation to consider is the heat distribution

$$k_{He}\frac{\partial^2 T}{\partial x^2} = -\frac{\omega}{2\pi}\int_t^{t+2\pi/\omega} j(\tau)E(\tau)d\tau \qquad k_{He}\frac{\hat{T}}{\hat{x}^2}\frac{\partial^2\Omega}{\partial X^2} = -\frac{1}{2\pi}\frac{1}{\hat{t}}\int_T^{T+2\pi/\omega}\hat{j}J(\xi)\hat{E}E(\xi)d\hat{t}\,\xi$$

$$\frac{\partial^2\Omega}{\partial X^2} = -\frac{\hat{x}^2\hat{j}\hat{E}}{2\pi k_{He}\hat{T}}\int_T^{T+2\pi/\omega} J(\xi)E(\xi)d\xi \tag{47}$$

Thus, the characteristic temperature is $\hat{T} = \frac{\hat{x}^2\hat{j}\hat{E}}{2\pi k_{He}}$. The heat diffusion equation becomes

$$\frac{\partial^2\Omega}{\partial X^2} = -\int_T^{T+2\pi/\omega} J(\xi)E(\xi)d\xi \tag{48}$$

The 1D problem considered in this article is only a part of a larger system that represents the whole LAPPD head. The plasma generation part of the system can be well described with 1D approximation, but the rest of the system has to be simulated in 2D with inclusion of additional effects. Such a simulation requires significant computational resources; this is why we found a parallel computational approach to be helpful for this problem. Application of parallel code to plasma generation provides us with a good opportunity to evaluate implementation and performance details, as well as to establish the general approach to the whole problem using the

simplicity of 1D representation. This approach can be expanded for the 2D case and used for simulation of the LAPPD head, although some modifications may appear necessary due to the geometrical reasons.

The solution process is performed on a cluster for parallel computations, that features distributed memory access [69]. We use OpenMPI library [70] to provide parallel capabilities to our code. In accordance to MPI-approach, the computational job is explicitly distributed and synchronized between MPI-nodes at the stage of programming [71].

Table 3
The variables used in the model with characteristic coefficients and physical units

Variable	Charact.	Unit	Variable	Charact.	Unit
Time	$\hat{t} = const$	$[\mathrm{s}]$	Recombination	$\hat{k} = 1/\hat{n}\hat{t}$	$[\mathrm{m}^3/s]$
Length	$\hat{x} = L$	$[\mathrm{m}]$	Ionization	$\hat{\alpha} = 1/L$	$[1/\mathrm{m}]$
El. potential	$\hat{\varphi} = U_0$	$[\mathrm{V}]$	Diffusion	$\hat{D} = L^2/\hat{t}$	$[\mathrm{m}^2/s]$
El. field	$\hat{E} = U_0/L$	$[\mathrm{V/m}]$	Temperature	$\hat{T} = \varepsilon_0 U_0^2/2\pi k_{He}\hat{t}$	$[\mathrm{K}]$
Number density	$\hat{n} = \varepsilon_0 U_0/eL^2$	$[1/\mathrm{m}^3]$	Current density	$\hat{j} = \varepsilon_0 U_0/\hat{t}L$	$[\mathrm{A/m}^2]$
Velocity	$\hat{v} = \hat{x}/\hat{t}$	$[\mathrm{m/s}]$	Power	$\hat{W} = \hat{j}\hat{E} = \varepsilon_0 U_0^2/\hat{t}L^2$	$[\mathrm{W/m}^3]$

We provide a general description of the solution procedure in this section. We assume that number density of species is specified either from initial conditions or from the previous time step of the simulation. Based on number density values, we formulate and solve the Poisson equation to update the electric field. The reduced electric field is calculated using the number density of the neutral gas; the field is further used for interpolation through tables of rate parameters for electrons and positive ions to update local values at the grid-nodes. The next step evaluates species' fluxes at the boundary and the final step calculates some additional parameters that are required for characterization of plasma.

When electric field, velocities, rate parameters, and boundary fluxes are updated, they are used in the formulation of the System of Linear Equations (SLE) which is solved for new values of species' number density. There is a plethora of algorithms available for the solution of the system on a single machine. For solution carried over a cluster of parallel computers, the problem must be decomposed. Each parallel machine receives its local portion of the domain. Based on this portion, it formulates and solves a local part of the SLE. In this case, a numerical method requires a modification.

Solution for Number Density

We use Finite Volumes method [72] as a numerical scheme for continuity equations. Additionally, we apply Scharfetter-Gummel scheme [43, 55, 73] to reduce "saw effect" that appears due to instability developed due to convective terms in the governing equations (40). SLE that is derived from the governing equations has a tri-diagonal matrix. Using advantages of such a matrix shape, we implement Thomas method which is known to be efficient in solution of tri-diagonal systems.

The upwind numerical scheme is applied for equations responsible for convective transfer of fluids. When regular finite volume approach is used, the convective term of the considered equation is descritized with finite differences based on the averaged value of a function at the boundary between two finite volumes. This approach is not sufficient for convective flow as it yields with instability which appears as a "saw" effect. The upwind scheme (Figure 13) modifies the descritization to account for direction of major change of the function due to imposed velocity field.

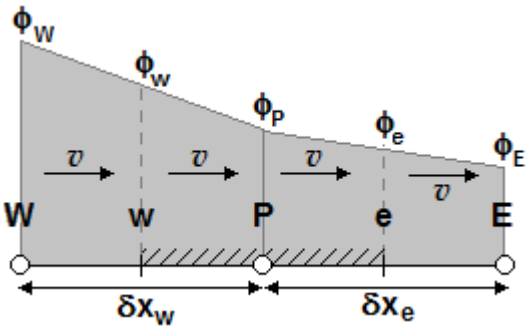

Figure 13. Upwind numerical scheme for 1D computational domain

Let us consider a typical differential equation for fluid convection/diffusion (49)

$$\frac{\mathrm{d}(\rho u\varphi)}{\mathrm{d}\,x}=\frac{d}{dx}\left(\Gamma\frac{d\varphi}{dx}\right) \tag{49}$$

This equation is integrated over a finite volume (w,e) which is shown in Figure 13.

$$\int_w^e \frac{\mathrm{d}(\rho u\varphi)}{\mathrm{d}\,x}dx=\int_w^e \frac{d}{dx}\left(\Gamma\frac{d\varphi}{dx}\right)dx \qquad (\rho u\varphi)_e-(\rho u\varphi)_w=\left(\Gamma\frac{d\varphi}{dx}\right)_e-\left(\Gamma\frac{d\varphi}{dx}\right)_w$$

$$(\rho u)_e\varphi_e-(\rho u)_w\varphi_w=\Gamma_e\frac{\varphi_E-\varphi_P}{\delta x_e}-\Gamma_w\frac{\varphi_P-\varphi_W}{\delta x_w} \tag{50}$$

The right-hand side of the equation is defined through the values of the domain nodes, while the left-hand side is defined in terms of intermediate values which have to be approximated through the nodes. The regular finite difference would assume a linear interpolation between the nodes and result with

$$\begin{aligned}\varphi_e&=(\varphi_P+\varphi_E)/2\\ \varphi_w&=(\varphi_P+\varphi_W)/2\end{aligned} \tag{51}$$

To correct this result, the upwind numerical scheme, suggests to not linearly interpolate the values of function at intermediate nodes, but to use the value of the function from that neighbor node which is placed upstream, considering the velocity of fluid. The general rule is as follows

$$\varphi_e = \begin{cases} \varphi_P, u_e > 0 \\ \varphi_E, u_e < 0 \end{cases}$$
$$\varphi_w = \begin{cases} \varphi_W, u_w > 0 \\ \varphi_P, u_w < 0 \end{cases} \quad (52)$$

For the case shown in Figure 13 the differential equation would descritize as follows

$$\left\{ -\frac{\Gamma_w}{\delta x_w} - (\rho u)_w \right\} \varphi_W + \left\{ (\rho u)_e + \frac{\Gamma_e}{\delta x_e} + \frac{\Gamma_w}{\delta x_w} \right\} \varphi_P + \left\{ -\frac{\Gamma_e}{\delta x_e} \right\} \varphi_E = 0 \quad (53)$$

The governing equations can be descritized using the upwind numerical scheme. Let us consider the continuity equation for electrons, for positive ions the approach is similar. We write step-by-step descritization, so that each modification is easy to track.

$$\frac{\partial n_e}{\partial t} + \frac{\partial}{\partial x}\left(v_e^d n_e - D_e \frac{\partial n_e}{\partial x} \right) = (\alpha - \eta) n_e \left| v_e^d \right| - k_{ie}^{rec} n_e n_p \quad (54)$$

Write it in terms of fluxes

$$\frac{\partial n_e}{\partial t} + \frac{\partial Q}{\partial x} = R$$
$$Q = v_e^d n_e - D_e \frac{\partial n_e}{\partial x} \quad (55)$$
$$R = (\alpha - \eta) n_e \left| v_e^d \right| - k_{ie}^{rec} n_e n_p$$

Integrate the equation over a finite volume at the node *i*

$$\int_{i-1/2}^{i+1/2} \frac{\partial n_e}{\partial t} dx + \int_{i-1/2}^{i+1/2} \frac{\partial Q}{\partial x} dx = \int_{i-1/2}^{i+1/2} R dx \quad (56)$$

We apply the mean integral theorem and assume that the nodes are equally spaced

$$\left(\frac{\partial n_e}{\partial t} \right)_i \delta x + Q_{i+1/2} - Q_{1-1/2} = R_i \delta x \quad (57)$$

The fluxes are written using upwind numerical scheme

$$
\begin{aligned}
&Q_{i+1/2} = \left(v_e^d n_e\right)_{i+1/2} - D_{e,i+1/2}\frac{n_{e,i+1}-n_{e,i}}{\delta x} = \\
&= v_{e,i+1/2}^d \begin{Bmatrix} n_{e,i},\ v_{e,i+1/2}^d > 0 \\ n_{e,i+1},\ v_{e,i+1/2}^d < 0 \end{Bmatrix} - D_{e,i+1/2}\frac{n_{e,i+1}-n_{e,i}}{\delta x}
\end{aligned}
$$

$$
\begin{aligned}
&Q_{i-1/2} = \left(v_e^d n_e\right)_{i-1/2} - D_{e,i-1/2}\frac{n_{e,i}-n_{e,i-1}}{\delta x} = \\
&= v_{e,i-1/2}^d \begin{Bmatrix} n_{e,i-1},\ v_{e,i-1/2}^d > 0 \\ n_{e,i},\ v_{e,i-1/2}^d < 0 \end{Bmatrix} - D_{e,i-1/2}\frac{n_{e,i}-n_{e,i-1}}{\delta x}
\end{aligned}
\tag{58}
$$

Substitute fluxes back into the equation and gather the terms in front of number density

$$
\begin{aligned}
&\left(\frac{n_{e,i}^{new}-n_{e,i}^{old}}{\delta t}\right)_i \delta x + v_{e,i+1/2}^d \begin{Bmatrix} n_{e,i},\ v_{e,i+1/2}^d > 0 \\ n_{e,i+1},\ v_{e,i+1/2}^d < 0 \end{Bmatrix} - D_{e,i+1/2}\frac{n_{e,i+1}-n_{e,i}}{\delta x} \\
&- v_{e,i-1/2}^d \begin{Bmatrix} n_{e,i-1},\ v_{e,i-1/2}^d > 0 \\ n_{e,i},\ v_{e,i-1/2}^d < 0 \end{Bmatrix} + D_{e,i-1/2}\frac{n_{e,i}-n_{e,i-1}}{\delta x} = R_i \delta x
\end{aligned}
\tag{59}
$$

$$
\begin{aligned}
&\frac{\delta x}{\delta t} n_{e,i} - \frac{D_{e,i+1/2}}{\delta x} n_{e,i+1} + \frac{D_{e,i+1/2}}{\delta x} n_{e,i} + \frac{D_{e,i-1/2}}{\delta x} n_{e,i} - \frac{D_{e,i-1/2}}{\delta x} n_{e,i-1} \\
&+ n_{e,i} \begin{Bmatrix} v_{e,i+1/2}^d,\ v_{e,i+1/2}^d > 0 \\ 0,\ v_{e,i+1/2}^d < 0 \end{Bmatrix} + n_{e,i+1} \begin{Bmatrix} 0,\ v_{e,i+1/2}^d > 0 \\ v_{e,i+1/2}^d,\ v_{e,i+1/2}^d < 0 \end{Bmatrix} \\
&- n_{e,i-1} \begin{Bmatrix} v_{e,i-1/2}^d,\ v_{e,i-1/2}^d > 0 \\ 0,\ v_{e,i-1/2}^d < 0 \end{Bmatrix} - n_{e,i} \begin{Bmatrix} 0,\ v_{e,i-1/2}^d > 0 \\ v_{e,i-1/2}^d,\ v_{e,i-1/2}^d < 0 \end{Bmatrix} = \frac{\delta x}{\delta t} n_{e,i}^{old} + R_i \delta x
\end{aligned}
\tag{60}
$$

Finally, the numerical scheme may be written in a shorter form (61)

$$
\begin{aligned}
&A_i n_{e,i-1} + C_i n_{e,i} + B_i n_{e,i+1} = F_i \\
&\begin{cases}
A_i = -\dfrac{D_{e,i-1/2}}{\delta x} - \begin{Bmatrix} v_{e,i-1/2}^d,\ v_{e,i-1/2}^d > 0 \\ 0,\ v_{e,i-1/2}^d < 0 \end{Bmatrix} \\
B_i = -\dfrac{D_{e,i+1/2}}{\delta x} + \begin{Bmatrix} 0,\ v_{e,i+1/2}^d > 0 \\ v_{e,i+1/2}^d,\ v_{e,i+1/2}^d < 0 \end{Bmatrix} \\
C_i = \dfrac{\delta x}{\delta t} + \begin{Bmatrix} v_{e,i+1/2}^d,\ v_{e,i+1/2}^d > 0 \\ 0,\ v_{e,i+1/2}^d < 0 \end{Bmatrix} - \begin{Bmatrix} 0,\ v_{e,i-1/2}^d > 0 \\ v_{e,i-1/2}^d,\ v_{e,i-1/2}^d < 0 \end{Bmatrix} + \dfrac{D_{e,i+1/2}}{\delta x} + \dfrac{D_{e,i-1/2}}{\delta x} \\
F_i = \dfrac{\delta x}{\delta t} n_{e,i}^{old} + R_i \delta x
\end{cases}
\end{aligned}
\tag{61}
$$

The same approach is applied to positive ions, except all diffusion coefficients are zero, because there is no diffusion for ions in the model.

Based on the method proposed in [74] we develop a numerical scheme that could be applied for the efficient solution of the plasma model using a cluster for parallel computations. The 1D governing equations describing the model are descritized based on the three nodes pattern. This pattern results in a tri-diagonal matrix which is relatively easy to solve on a single machine; the most advantageous method in this case is Thomas method. When we transfer the model to the cluster for parallel computations the solution method is not directly applicable. Thus, the parallel model requires a special approach with additional derivations in order to transform the matrix and apply one of the numerical algorithms designed for the solution of system of linear equations (SLE).

There are few numerical methods that are often used for evaluation of SLEs. There is one approach that allows implementation of Thomas method for the parallel problems with a modified system matrix. We would like to consider such a modification and develop the necessary theoretical understanding. The following derivations are self-consistent; they can be applied to any tri-diagonal system, as long as the system is not singular and is positive defined. Thus, the notation used in the derivation is specific to this part of the work only; it has no relation to plasma parameters. The initial matrix divided between 3 processors (3 blocks) has the following form

Here v_i are vectors that represent rows of the system matrix, x_i are unknowns that need to be found, coefficients A_i, B_i, C_i, F_i are the coefficients of the descritized governing equation calculated for the node i

$$A_i x_{i-1} + C_i x_i + B_i x_{i+1} = F_i \tag{62}$$

Figure 14 shows a matrix corresponding to this system. The matrix is split between parallel processes.

$$\begin{array}{l}
v_0 = \\ v_1 = \\ v_2 = \\ v_3 = \\ v_4 = \\ \hline v_5 = \\ v_6 = \\ v_7 = \\ v_8 = \\ v_9 = \\ \hline v_{10} = \\ v_{11} = \\ v_{12} = \\ v_{13} = \\ v_{14} =
\end{array}
\left(\begin{array}{cccccccccccccc}
C_0 & B_0 & 0 & 0 & 0 & 0 & 0 & 0 & 0 & 0 & 0 & 0 & 0 & 0 \\
A_1 & C_1 & B_1 & 0 & 0 & 0 & 0 & 0 & 0 & 0 & 0 & 0 & 0 & 0 \\
0 & A_2 & C_2 & B_2 & 0 & 0 & 0 & 0 & 0 & 0 & 0 & 0 & 0 & 0 \\
0 & 0 & A_3 & C_3 & B_3 & 0 & 0 & 0 & 0 & 0 & 0 & 0 & 0 & 0 \\
0 & 0 & 0 & A_4 & C_4 & B_4 & 0 & 0 & 0 & 0 & 0 & 0 & 0 & 0 \\ \hline
0 & 0 & 0 & 0 & A_5 & C_5 & B_5 & 0 & 0 & 0 & 0 & 0 & 0 & 0 \\
0 & 0 & 0 & 0 & 0 & A_6 & C_6 & B_6 & 0 & 0 & 0 & 0 & 0 & 0 \\
0 & 0 & 0 & 0 & 0 & 0 & A_7 & C_7 & B_7 & 0 & 0 & 0 & 0 & 0 \\
0 & 0 & 0 & 0 & 0 & 0 & 0 & A_8 & C_8 & B_8 & 0 & 0 & 0 & 0 \\
0 & 0 & 0 & 0 & 0 & 0 & 0 & 0 & A_9 & C_9 & B_9 & 0 & 0 & 0 \\ \hline
0 & 0 & 0 & 0 & 0 & 0 & 0 & 0 & 0 & A_{10} & C_{10} & B_{10} & 0 & 0 \\
0 & 0 & 0 & 0 & 0 & 0 & 0 & 0 & 0 & 0 & A_{11} & C_{11} & B_{11} & 0 \\
0 & 0 & 0 & 0 & 0 & 0 & 0 & 0 & 0 & 0 & 0 & A_{12} & C_{12} & B_{12} \\
0 & 0 & 0 & 0 & 0 & 0 & 0 & 0 & 0 & 0 & 0 & 0 & A_{13} & C_{13} \\
0 & 0 & 0 & 0 & 0 & 0 & 0 & 0 & 0 & 0 & 0 & 0 & 0 & A_{14}
\end{array}\right)
\left(\begin{array}{c}
x_0 \\ x_1 \\ x_2 \\ x_3 \\ x_4 \\ \hline x_5 \\ x_6 \\ x_7 \\ x_8 \\ x_9 \\ \hline x_{10} \\ x_{11} \\ x_{12} \\ x_{13} \\ x_{14}
\end{array}\right)
=
\left(\begin{array}{c}
F_0 \\ F_1 \\ F_2 \\ F_3 \\ F_4 \\ \hline F_5 \\ F_6 \\ F_7 \\ F_8 \\ F_9 \\ \hline F_{10} \\ F_{11} \\ F_{12} \\ F_{13} \\ F_{14}
\end{array}\right)
\begin{array}{c}
\\ \\ \\ \\ \\ \\ \\ \\ \\ \\ \\ \\ \\ \\ \\
\end{array}$$

Figure 14. System of linear equations divided into blocks for calculation on parallel processors

Following the algorithm proposed by [74] we determine the major parameters required during the derivation – size of a block n, number of processors n_p, and index of the first row of each block in the system matrix j_k

$$n = 5, n_p = 3$$

$$j_k = kn, \quad k = 0..n_p - 1 \qquad j_0 = 0 \qquad j_1 = 5 \qquad j_2 = 10$$

We switch from the global coordinate system to local coordinates of each block (index $i = 0...n-1$ would represent a row within a block), denoting the block with index $k = 0...n_p - 1$. The parameter j_k is determined as $j_k = kn$ and determines the relation between local and global

coordinate systems in the system matrix. The indices are start from 0 and finish with $n-1$ to replicate the index notation of C-language. The next sections describe the algorithm taking a block *k* as an example.

The general idea of the modification is to remove dependence between neighbor blocks. Since the blocks become independent, they can be solved on a local processor in parallel with the same solution done on other processors for other blocks of the system matrix. In tridiagonal matrix the dependence is implemented in two first and two last rows of each block. For example, the blocks k and $k+1$ share variables x_k, x_{k+1}; the variable x_k enters the rows $n-2, n-1$ of the block k and row 0 of the block $k+1$. The same way, the variable x_{k+1} enters row $n-1$ of the block k and rows $0,1$ of the block $k+1$. The modification algorithm passes through blocks and assembles two "boundary equations" for each block as a linear combination of the rows constituting the block. The boundary equations from each block are assembled into a system of linear equations, which has smaller size equal to $2n_p$, because there are n_p blocks with two boundary equations each. This system of boundary equations (SBE) has the tridiagonal form and can be solved with Thomas method. Since the SBE has a small size it can be solved very efficiently. For instance, a SLE of 10000x10000 elements may be split between 100 processors, then each bock would have 100x10000 elements and SBE would be 200x200 elements. Next, using the fact that the matrix is tridiagonal, we can reduce the size of the blocks to 100x100, as the rest of the block is filled with zeroes. This way, the initial 100000x100000 system transforms into 100 smaller systems of 100x100 elements and one SBE of 200x200 elements.

The solution of SBE represents the exact values of the variables x_k, x_{k+1} for each block. When these values are known, each block is modified with transformation of two first rows and

two last rows, with only $n-2$ variables requiring the solution. Thus instead of solving 100x100 SLE from the previous example, we need to solve 98x98 SLE. The solution of the local SLEs is done in parallel mode, utilizing the advantages provided by parallel approach.

Now, we would like to explain the modification method in more detail. Let's consider the block k as the current block that is sent for modification. We define an upper boundary as the interface between blocks k and $k-1$ and a lower boundary as the interface between blocks k and $k+1$. We initialize the upper and lower boundary vectors $v_{lk}^{(j_k)}$ and right hand side elements $F_{lk}^{(j_k)}$. In the global coordinates these entities are written as follows

$$v_{lk}^{(j_k+1)} = v_{j_k+1} \text{ - this is the second row at each block} \qquad F_{lk}^{(j_k+1)} = F_{j_k+1} \tag{63}$$

$$v_{lk}^{(j_k+n-2)} = v_{j_k+n-2} \text{ - this is the 2}^{\text{nd}} \text{ row from the end of the block} \qquad F_{lk}^{(j_k+n-2)} = F_{j_k+n-2}$$

The same entities in the local coordinates

$$v_{lk}^{(1)} = v_1 = \begin{pmatrix} A_1 & C_1 & B_1 & 0 & 0 & 0 & 0 & 0 & 0 & 0 & 0 & 0 & 0 & 0 \end{pmatrix} \quad F_{lk}^{(1)} = F_1 \tag{64}$$

$$v_{uk}^{(n-2)} = v_{n-2} = \begin{pmatrix} 0 & 0 & A_{n-2} & C_{n-2} & B_{n-2} & 0 & 0 & 0 & 0 & 0 & 0 & 0 & 0 & 0 \end{pmatrix} \quad F_{uk}^{(n-2)} = F_{n-2}$$

For the lower boundary, iterate the summation of the elements, gathering a linear combination of the rows 2 to *n*-1 within the block. The following are the elements in the global coordinates

$$a_i = \frac{v_{i,i-1}}{v_{lk,i-1}} \qquad \bar{v}_{lk}^{(i)} = \bar{v}_i - a_i \bar{v}_{lk}^{(i-1)} \qquad F_{lk}^{(i)} = F_i - a_i F_{lk}^{(i-1)} \tag{65}$$

In local coordinates it can be written like

$$F_{lk}^{(2)} = F_2 - a_2 F_1$$

$$\bar{v}_{lk}^{(2)} = \bar{v}_2 - a_2 \bar{v}_1 \tag{66}$$

$$\bar{v}_{lk}^{(2)} = \begin{pmatrix} -a_2 A_1 & \underline{A_2 - a_2 C_1} & C_2 - a_2 B_1 & B_2 & 0 & 0 & 0 & 0 & 0 & 0 & 0 & 0 & 0 & 0 \end{pmatrix}$$

The coefficient $a_i = a_2$ is chosen such as coordinate $v^{(i)}_{lk,i-1}$ (in this case it is $A_2 - a_2 C_1$) would turn zero. The general sequence for the lower boundary is

$$\bar{v}^{(2)}_{lk} = \left(-a_2 A_1 \quad \underline{A_2 - a_2 C_1} \quad C_2 - a_2 B_1 \quad B_2 \quad 0 \quad 0 \quad 0 \quad 0 \quad 0 \quad 0 \quad 0 \quad 0 \quad 0 \quad 0 \quad 0\right)$$

$$\bar{v}^{(3)}_{lk} = \left(a_2 a_3 A_1 \quad 0 \quad \underline{A_3 - a_3\left(C_2 - a_2 B_1\right)} \quad C_3 - a_3 B_2 \quad B_3 \quad 0 \quad 0 \quad 0 \quad 0 \quad 0 \quad 0 \quad 0 \quad 0 \quad 0 \quad 0\right)$$

$$\bar{v}^{(4)}_{lk} = \left(-a_2 a_3 a_4 A_1 \quad 0 \quad 0 \quad \underline{A_4 - a_4\left(C_3 - a_3 B_2\right)} \quad C_4 - a_4 B_3 \quad B_4 \quad 0 \quad 0 \quad 0 \quad 0 \quad 0 \quad 0 \quad 0 \quad 0 \quad 0\right)$$

$$a_2 = \frac{A_2}{C_1} \qquad a_3 = \frac{A_3}{C_2 - a_2 B_1} \qquad a_4 = \frac{A_4}{C_3 - a_3 B_2} \tag{67}$$

$$F^{(2)}_{lk} = F_2 - a_2 F_1 \qquad F^{(3)}_{lk} = F_3 - a_3 F_2 + a_3 a_2 F_1$$

$$F^{(4)}_{lk} = F_4 - a_4 F_3 + a_4 a_3 F_2 - a_4 a_3 a_2 F_1$$

Summarizing the lower boundary condition, we can write

1. Calculate: $a_1 = 0,\ a_i = \dfrac{A_i}{C_{i-1} - a_{i-1} B_{i-2}},\ i = 2 \ldots n-1$
2. Calculate: $F^{(n-1)}_{lk} = \sum_{i=1}^{n-1}\left[\left(-1\right)^{n-1-i}\left(\prod_{j=i+1}^{n-1} a_j\right) F_i\right]$
3. Calculate: $\bar{v}_{lk,kn} = \bar{v}_{lk,0local} = \left(-1\right)^{n-2}\left(\prod_{j=2}^{n-1} a_j\right) A_1$ - see the *note* on the sign at the end

$$\bar{v}_{lk,(k+1)n-1} = \bar{v}_{lk,n-1} = C_{n-1} - a_{n-1} B_{n-2}$$

$$\bar{v}_{lk,(k+1)n} = \bar{v}_{lk,n} = B_{n-1}$$

The element $\bar{v}_{lk,(k+1)n}$ is omitted for the last block. For the upper boundary equations, iterate the summation of the elements, gathering a linear combination of the rows n-3 down to 0 within the block. Elements in global coordinates are

$$b_i = \frac{v_{i,i+1}}{v_{uk,i+1}} \qquad \bar{v}_{uk}^{(i)} = \bar{v}_i - b_i \bar{v}_{uk}^{(i+1)} \qquad F_{uk}^{(i)} = F_i - b_i F_{uk}^{(i+1)} \tag{68}$$

It can be written in local coordinates as follows

$$F_{uk}^{(n-3)} = F_{n-3} - b_{n-3} F_{n-2}$$

$$\bar{v}_{uk}^{(n-3)} = \bar{v}_{n-3} - b_{n-3} \bar{v}_{uk}^{(n-2)} \tag{69}$$

$$\bar{v}_{uk}^{(n-3)} = \begin{pmatrix} 0 & A_{n-3} & C_{n-3} - b_{n-3} A_{n-2} & B_{n-3} - b_{n-3} C_{n-2} & -b_{n-3} B_{n-2} & 0 & 0 & 0 & 0 & 0 & 0 & 0 & 0 & 0 & 0 \end{pmatrix}$$

The coefficient $b_i = b_{n-3}$ is chosen such as coordinate $v_{lk,i+1}^{(i)}$ (in this case it is $B_{n-3} - b_{n-3} C_{n-2}$)

turns zero.

The general sequence for upper boundary is

$$\bar{v}_{uk}^{(n-2)} = \begin{pmatrix} 0 & 0 & A_{n-2} & C_{n-2} & B_{n-2} & 0 & 0 & 0 & 0 & 0 & 0 & 0 & 0 & 0 & 0 \end{pmatrix}$$

$$\bar{v}_{uk}^{(n-3)} = \begin{pmatrix} 0 & A_{n-3} & C_{n-3} - b_{n-3} A_{n-2} & B_{n-3} - b_{n-3} C_{n-2} & -b_{n-3} B_{n-2} & 0 & 0 & 0 & 0 & 0 & 0 & 0 & 0 & 0 & 0 \end{pmatrix}$$

$$\bar{v}_{uk}^{(n-4)} = \begin{pmatrix} A_{n-4} & C_{n-4} - b_{n-4} A_{n-3} & B_{n-4} - b_{n-4}\left(C_{n-3} - b_{n-3} A_{n-2}\right) & 0 & b_{n-4} b_{n-3} B_{n-2} & 0 & 0 & 0 & 0 & 0 & \ldots \end{pmatrix}$$

$$\bar{v}_{uk}^{(n-5)} = A_{n-5} \ldots \underline{\begin{pmatrix} C_{n-5} - b_{n-5} A_{n-4} & B_{n-5} - b_{n-5}\left(C_{n-4} - b_{n-4} A_{n-3}\right) & 0 & 0 & -b_{n-5} b_{n-4} b_{n-3} B_{n-2} & 0 & 0 & 0 & \ldots \end{pmatrix}}$$

$$F_{uk}^{(n-3)} = F_{n-3} - b_{n-3} F_{n-2} \qquad F_{uk}^{(n-4)} = F_{n-4} - b_{n-4} F_{n-3} + b_{n-4} b_{n-3} F_{n-2} \tag{70}$$

$$F_{uk}^{(n-5)} = F_{n-5} - b_{n-5} F_{n-4} + b_{n-5} b_{n-4} F_{n-3} - b_{n-5} b_{n-4} b_{n-3} F_{n-2}$$

$$b_{n-3} = \frac{B_{n-3}}{C_{n-2}} \qquad b_{n-4} = \frac{B_{n-4}}{C_{n-3} - b_{n-3} A_{n-2}} \qquad b_{n-5} = \frac{B_{n-5}}{C_{n-4} - b_{n-4} A_{n-3}}$$

We can summarize the upper boundary condition as follows

1. Calculate: $b_{n-2} = 0,\ b_i = \frac{B_i}{C_{i+1} - b_{i+1} A_{i+2}},\ i = n-3 \ldots 0$

2. Calculate: $$F_{uk}^{(0)} = \sum_{i=0}^{n-2}\left[(-1)^i\left(\prod_{j=0}^{i-1} b_j\right)F_i\right]$$

3. Calculate: $$\bar{v}_{uk,kn-1} = \bar{v}_{uk,-1local} = A_0$$

$$\bar{v}_{uk,kn} = \bar{v}_{uk,0} = C_0 - b_0 A_1$$

$$\bar{v}_{uk,(k+1)n-1} = \bar{v}_{uk,n-1} = (-1)^{n-2}\left(\prod_{j=0}^{n-3} b_j\right)B_{n-2}$$ - see the note on sign at the end

The element $\bar{v}_{lk,kn-1}$ is omitted for the first block.

$A =$

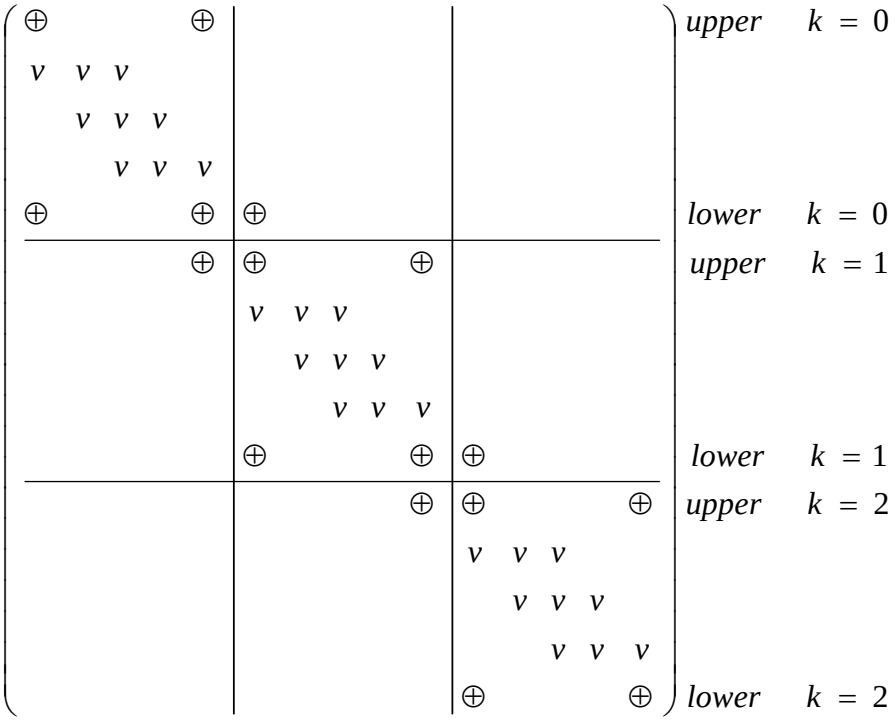

Figure 15. System of linear equations – dependent variables

We should *note* about the proper *sign*. Out of n rows in the block, we skip #0 and take #1 as the initial row for the lower interface and skip #n-1 and take as the initial #n-2 for the upper interface, the rest we iterate. The rest is n-2 equations; therefore we have to make n-2 iterations for each calculation of interface in the block. For odd number of iterations the sign is negative; it

is positive for even number of iteration. Thus, the number n-2 determines the sign of the last element in the iteration sequence for both interfaces.

The initial SLE is modified using the described approach so that the shared variables of each block become the unknowns of the SBE. These variables are schematically shown in Figure 15. The minimal size of the block is 5 rows, the minimal size of the matrix solved with Thomas method is 3 rows. Thus, the minimal matrix that can be modified according to the described algorithm and can generate a SBE solvable with Thomas method consists of 15 rows and split between 3 processors.

If we remove the regular equations and condense the matrix shown in Figure 15, leaving only unknowns that come into the SBE, we would get a tri-diagonal system. The minimal size of the block is determined by the fact that we skip one equation from the top of the block and one equation from the bottom of the block, taking the 2nd equation (from the top/bottom) as the initial approximation for each interface. We rewrite the condensed system using the actual terms that were defined in the modification algorithm

$$A^* = \left(\begin{array}{cc|ccc|cc} \bar{v}_{u0,2^*} & \bar{v}_{u0,3^*} & & & & & \\ \bar{v}_{l0,1^*} & \bar{v}_{l0,2^*} & \bar{v}_{l0,3^*} & & & & \\ \hline & \bar{v}_{u1,1^*} & \bar{v}_{u1,2^*} & \bar{v}_{u1,3^*} & & & \\ & & \bar{v}_{l1,1^*} & \bar{v}_{l1,2^*} & \bar{v}_{l1,3^*} & & \\ \hline & & & \bar{v}_{u2,1^*} & \bar{v}_{u2,2^*} & \bar{v}_{u2,3^*} & \\ & & & & \bar{v}_{l2,1^*} & \bar{v}_{l2,2^*} & \end{array}\right) \times \left(\begin{array}{c} x_0 \\ x_{n-1} \\ \hline x_n \\ x_{2n-1} \\ \hline x_{2n} \\ x_{3n-1} \end{array}\right) = \left(\begin{array}{c} F_{u0}^{(0)} \\ F_{l0}^{(n-1)} \\ \hline F_{u1}^{(0)} \\ F_{l1}^{(n-1)} \\ \hline F_{u2}^{(0)} \\ F_{l2}^{(n-1)} \end{array}\right) \qquad (71)$$

The terms are calculated as follows (for each particular block k)

Right side: $$F_{lk}^{(n-1)} = \sum_{i=1}^{n-1}\left[(-1)^{n-1-i}\left(\prod_{j=i+1}^{n-1} a_j\right)F_i\right] \qquad F_{uk}^{(0)} = \sum_{i=0}^{n-2}\left[(-1)^{i}\left(\prod_{j=0}^{i-1} b_j\right)F_i\right] \qquad (72)$$

Lower: $$\bar{v}_{lk,1^*} = (-1)^{n-2}\left(\prod_{j=2}^{n-1} a_j\right)A_1 \qquad \bar{v}_{lk,2^*} = C_{n-1} - a_{n-1}B_{n-2} \qquad \bar{v}_{lk,3^*} = B_{n-1} \qquad (73)$$

Upper: $\bar{v}_{uk,1^*} = A_0 \qquad \bar{v}_{uk,2^*} = C_0 - b_0 A_1 \qquad \bar{v}_{uk,3^*} = (-1)^{n-2}\left(\prod_{j=0}^{n-3} b_j\right) B_{n-2}$ (74)

Coefficients: $a_1 = 0,\ a_i = \dfrac{A_i}{C_{i-1} - a_{i-1}B_{i-2}},\ i = 2...n-1$ (75)

$$b_{n-2} = 0,\ b_i = \frac{B_i}{C_{i+1} - b_{i+1}A_{i+2}},\ i = n-3...0$$

Solution of this systems yields with the first and the last x_i at each block. These x_i's are sent back to the blocks where they belong, the found *x*'s allow conversion of each local SLE into an independent SLE and solution of the modified system within the block.

Additionally, we should mention, the represented approach may be used in a recursive form. A system of equations with multi-million variables cannot be efficiently solved using only the described algorithm. For such large systems the logical topology of the parallel cluster needs to be changed into the tree-type arrangement. The initial system of equations is split between groups of parallel processors. Each group is connected to one processor that works as a master unit for the group. This unit receives boundary equations from the connected group and assembles them into the SBE. All master units can be considered as a system of the second level; each SBE is considered in the same way, as the block of the initial SLE for the system of the first level. Thus, SBEs, being the analog of the blocks, may be treated with the same modification algorithm and yield with boundary equations of the second level. The processors of the second level are also arranged into groups, each group is connected to a processor of the third level. The boundary conditions of the second level are sent to the third level processor, where the SBEs of the third level are assembled. These SBEs have much smaller size in comparison to the second level SBEs and, especially, in comparison to the initial SLE. The process is repeated to as many

levels as necessary to significantly reduce the system size. The structure resembles a tree; where each level represents branches and the top-most processor represents a root. Starting from the root, the SBE of the highest level is solved, the solution is sent to SBEs of the next lower level. The corresponding SBEs are modified to independent form and solved, sending their results to the lower level. The process repeats until it reaches the lowest level where blocks of initial SLE are modified and solved independently. Each level allows a solution of the system in parallel regime. This recursion approach may be used for the solution of large systems of linear equations featuring tri-diagonal matrices.

Parallel Approach

In the parallel approach, all MPI-nodes are essentially the same in abilities and function; therefore, it is up to our implementation to distinguish the following types of MPI-nodes: Master, Solver, and Printer; each type has a name according to its assigned function. The computational domain, containing plasma data, is divided into sections of equal size which we refer to as sub-domains. The sub-domains are distributed between Solvers. Each sub-domain includes a certain number of grid-nodes that contain local data, as well as a virtual grid-node on each end of the sub-domain. The virtual grid-nodes resemble the first or last grid-node of the neighbor sub-domain, when the nodes are located at an interface between two sub-domains. In the case of the boundary, they provide virtual fluxes, handling (non)penetration of species into the electrodes.

At the beginning of the calculations, Master process reads initial data from input data files. It prepares the necessary data structures and calculates some additional parameters – derivatives of the input data. This initial data is sent to all the Solvers and to the Printer. In order to estimate rate-parameters for the plasma, the electric field has to be calculated. Thus, the second stage of the calculation is solving the Poisson equation, estimation of reduced electric

field and calculation of rate coefficients. Since the whole process can be done in parallel form using only Solver nodes, Master and Printer are idling.

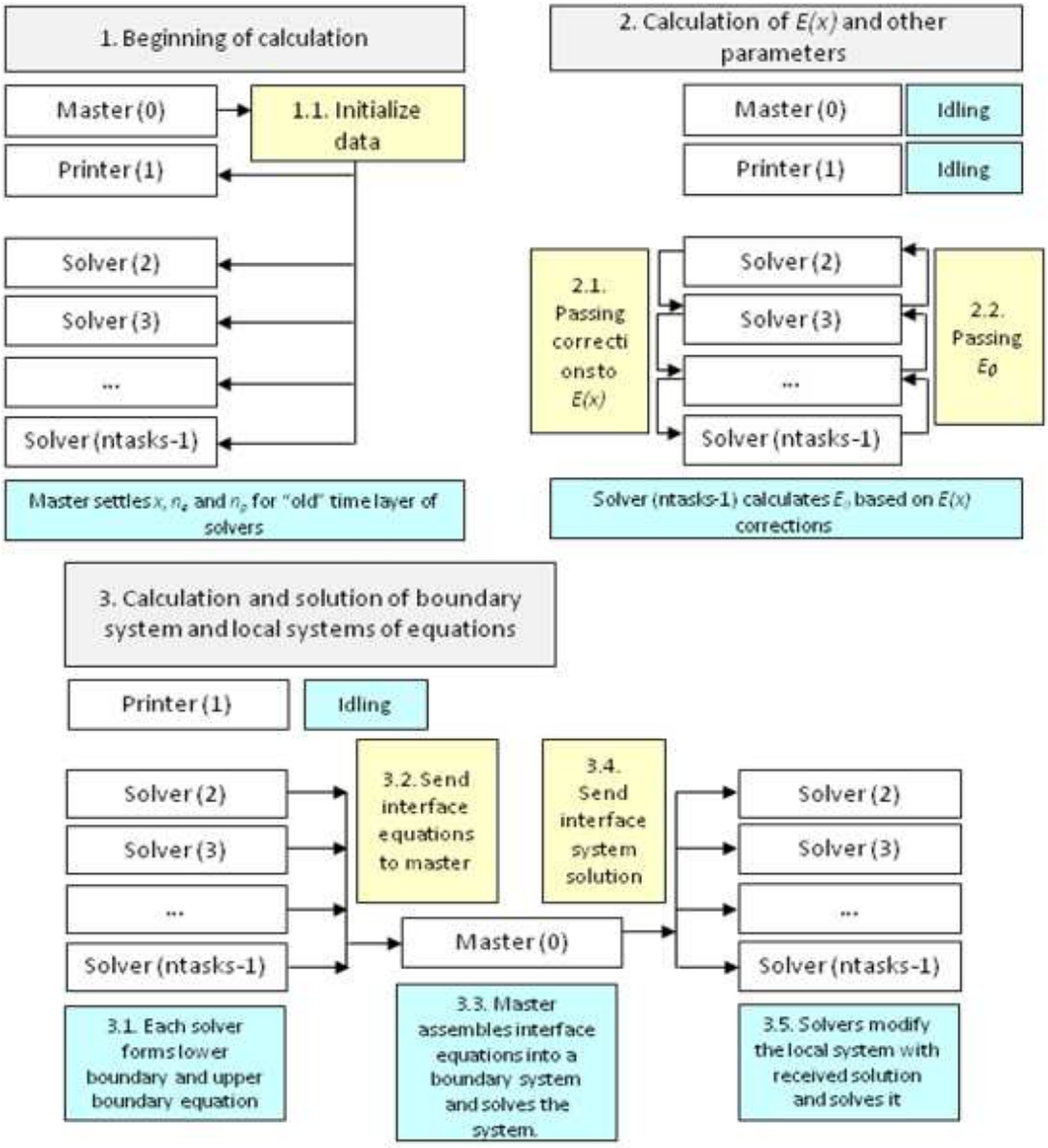

Figure 16. Diagram of the parallel algorithm

Solution for the electric field requires collaboration of all the Solvers; this is why complete parallelization is not possible for the applied algorithm. Calculation of rate parameters, on the other hand, is based on the local value of the reduced electric field at each particular node. This part of the calculation can be efficiently parallelized. The last step of the solution cycle is

the calculation of the number density of species through solving the system of continuity equations. Solvers populate local parts of SLE (please, refer to a diagram shown in Figure 15) that have cross-dependence. The dependence is present, because the diffusion terms of (33) require information from neighbor sub-domains.

Thus, in Figure 16, the SLE is distributed between the Solvers, but the subsystems cannot be solved locally because of the dependence. We utilize a “Memory efficient parallel tridiagonal solver” developed by Austin et al. [74] to remove the dependence between local parts of SLE. This algorithm is executed at Solvers building two linear Boundary Equations at each Solver. The Boundary Equations encapsulate specifics of the local portions of the SLE. They are sent to Master, where all such equations are assembled into the System of Boundary Equations (SBE). SBE features an interesting property: its matrix is also tri-diagonal. Hence, the Thomas algorithm is applicable for its solution. The solution of SBE represents updated number densities at the first and the last grid-nodes of each sub-domain. The updated values are sent to the corresponding Solvers (Figure 16), where the subsystems become modified and independent of their neighbors; hence, they can be solved in a regular way.

To summarize the parallel approach, the function of Master is to read input parameters at the beginning of the simulation, prepare initial data and distribute them through Solvers and Printer. The rest of the time Master idles, waiting for SBE from Solvers. When SBE is received (Figure 17), the solution of the system is evaluated and sent to Solvers, providing a good synchronization mechanism. At the final stage, Master finalizes all operations and provides performance data.

The primary function of Printer (Figure 17) is to provide input/output capabilities when there is a request for result writing/plotting. It idles most of the time during the simulation. At

specific moments of simulation time, Solvers send results of calculations to Printer and continue on their work. Printer processes the result, calculates additional data, and writes output to data-files without holding Solvers. This type of arrangement accelerates the performance of the code.

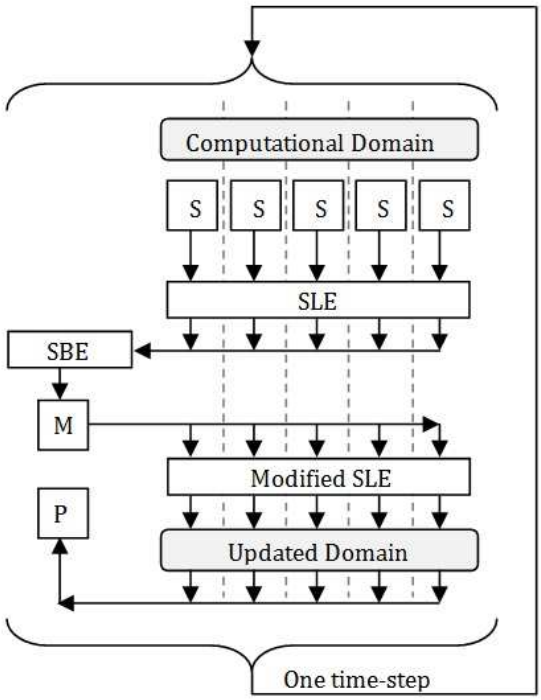

Figure 17. General representation of parallel algorithm for 1D plasma simulation. Symbols M, S, P denote Master, Solver, and Printer, correspondingly

Solution for Electric Field

When SLE is solved, the updated number density is used to renew the electric field. The Poisson equation is integrated numerically using an advantage of parallel computing to the full extent. The integration is performed simultaneously at all sub-domains, where local integrals of (37) are evaluated. In the process of local integration, the local electric field receives values that effectively resemble the shape of the electric field but lack the proper leveling (Figure 18.(a)).

In order to set the correct level, the value of the last (right) grid-node of each sub-domain is sent to the last Solver in the group. The local integrals are also sent to the last Solver, where the integration constant E_0 is estimated from the boundary condition (39). The last Solver

estimates the proper level and sends it to other Solvers to adjust the local electric field (Figure 18.(b)).

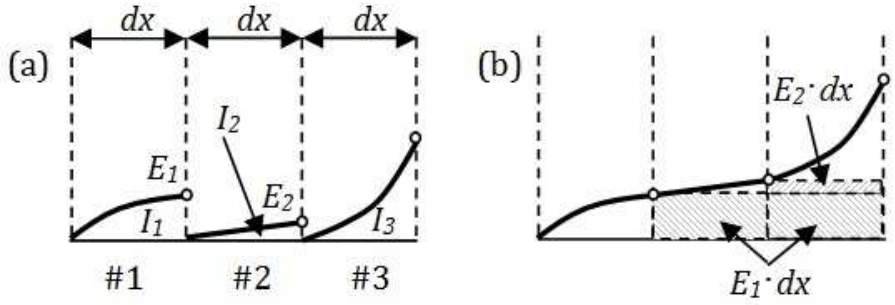

Figure 18. Parallel integration of Poisson equation: (a) the electric field before the adjustment; (b) the electric field after the adjustment

In our parallel implementation, the local integration data from all Solvers are collected at one (the last) Solver, which performs the necessary calculations and distributes the result through the rest of Solvers. As an alternative, we tried to pass the integration data in the "pipeline" arrangement. This approach was found to be less efficient, as the communication overhead was considerably higher.

The integration of electric field could be accomplished with different numerical methods, starting with rectangles' rule and finishing with Simpson method. During numerical evaluation we found that rectangular rule does not provide the necessary accuracy to the solution, which significantly distorts the resultant data. Surprisingly, Simpson method, providing higher accuracy, also yields inaccurate results. The trapezoidal rule was found the most efficient algorithm for integration of electric field. While it is simple enough to be rapidly resolved on the provided hardware, it provides sufficient accuracy and very good symmetrical result.

Solution for Ions' Temperature

The calculation of ions temperature is done at Printer by integrating (43) over the domain and starting from the center of the domain, where $\partial T/\partial x = 0$. The first integration yields the first derivative of temperature as a function of *x*. We use the temperature derivative at the wall (at the point T_w in the inset of Figure 19) to formulate thermal flux in accordance with Fourier law. The flux is transferred through the electrode and analyzed in the form of Newton's cooling law at the electrode/coolant interface (point T_{wc} in the inset of Figure 19) with heat convection coefficient $h_{air} = 681.23 \times 10^{-4}\ \mathrm{W/cm^2 \cdot K}$.

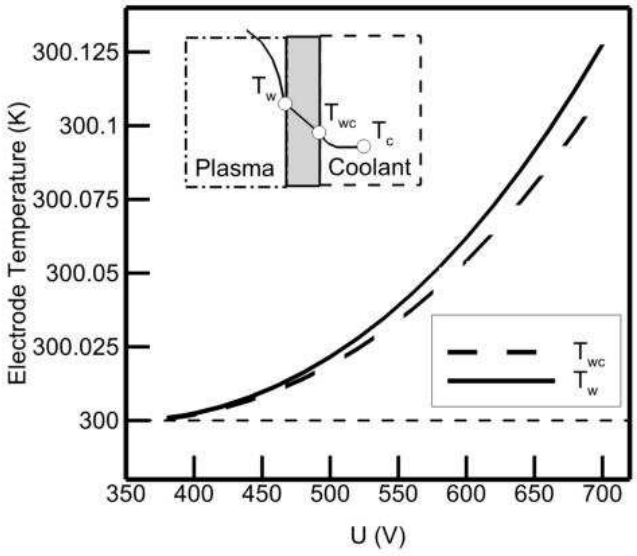

Figure 19. Electrodes' temperature estimated from temperature of ions calculated for a range of voltages 380V – 700 V

Temperature of the coolant is maintained at constant level 300 K. From Newton's law of cooling we derive the temperature of the electrode/coolant interface (T_{wc}). Next, we use Fourier law to estimate temperature of the electrode/plasma interface (T_w), with thermal conductivity of electrode $k_{Al} = 2.37\,\mathrm{W/cm \cdot K}$. The second integration starts from the wall and propagates

towards the center of the domain, yielding with temperature profile, and accounting for heat exchange between plasma and electrodes, as well as electrodes and coolant.

Estimation of Parallel Efficiency

We would like to estimate whether parallel implementation improves the efficiency of computations. In order to investigate an impact of the parallel paradigm, we attempt profiling of the code performance. The calculation operations, the MPI-communication, and input/output operations are subject to time logging. At the end of the simulation, all timing data are collected at Master, where they are averaged and further processed.

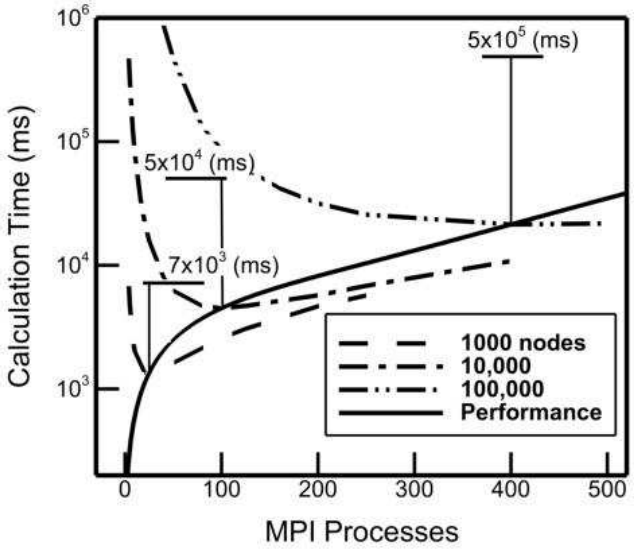

Figure 20. Performance of parallel computations for different number of grid-nodes in comparison to a single machine. The horizontal bars with numbers indicate computation time of a single machine. The vertical lines connect single time values with the optimal point of the corresponding parallel computation.

The data analysis is carried out in two modes. First, we compare overall performance of the parallel version to that of the single version. Second, we estimate a total-share taken by each type of parallel process (calculation, communication, i/o-operations) relative to total wall time.

The single machine used for performance metering has the same characteristics as the machines at a parallel MPI-cluster. The parameters of calculation are set to the same values for both, parallel and single cases with the same algorithms used, except for single/parallel differences. Thomas algorithm is quite efficient in solution of tri-diagonal systems; hence, we assume the single and the parallel code to be sufficiently optimized. Figure 20 represents a comparison of parallel and single modes evaluated for different problem size, which results in three cases, providing a general trend of performance change ("Performance" curve in Figure 20).

Each parallel case results in a performance curve that has a (minimum) point where the most favorable conditions are met for the given size of the problem. To the left of the optimal point, the performance curve bends up with a steep gradient due to computational overhead. To the right of the optimal point, the curve bends up due to communication overhead. The typical advantage of the parallel evaluation over the single evaluation is measured in terms of "speed-up" and shown in Table IV.

Table 4
Comparison of parallel and single performance

Problem size	MPI Processes (N_p)	Speed-up (S_p)	Parallel Fraction (P)
100	5	2.149254	66.84 %
1000	25	5.196733	84.122 %
10.000	100	11.20303	91.994 %
100.000	400	22.81252	95.856 %

The speed-up data can be used to measure an effectiveness of parallel implementation in terms of parallel fraction (P) of the code. The maximum speed-up achievable in the process of parallel computations is equal to number of used processors [75]. Amdahl law (76) provides a relation between speed-up (S_p), number of parallel processes (N_p), and the parallel fraction of the code (P).

$$S_p = \frac{1}{\left[P/N_P + (1-P)\right]} \qquad P = \frac{1/S_p - 1}{1/N_P - 1} \tag{76}$$

The estimations of parallel fraction (the 4th column of Table IV) yield with approximate range of 66% to 96%. According to Karniadakis and Kirby [76], the parallel fraction is a function of problem size, rather than a constant number. Therefore, we use the lowest value (67%) as a good estimation of a parallel portion of our code. There is a terminal value for the parallel fraction, as the speed-up reaches the saturation point when number of processors becomes sufficiently large. At this condition, the numerical code cannot run faster, as the gains from parallel execution of the code are well balanced by the losses from parallel communication [77]. We could reach such points for constant problem size, but not for scaling problem size, as 400 processors that we had available were not enough for detailed investigation of the speedup saturation.

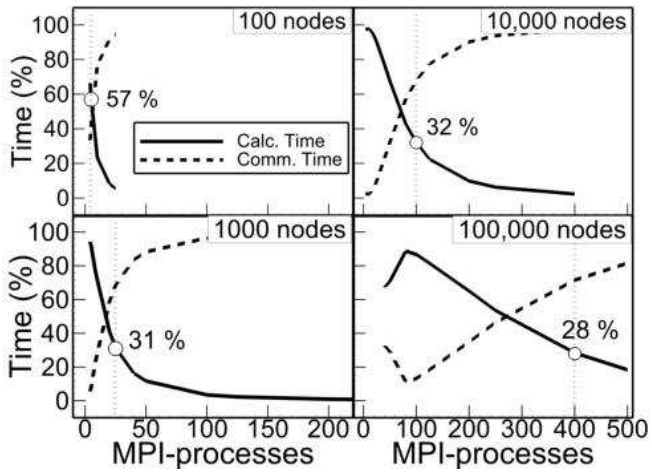

Figure 21. Averaged calculation time (solid) and communication time (dashed) of the simulation. The circle indicates the point of optimal performance. The vertical axis shows calculation/communnication time relative to the total wall time of the simulation

Another measure of the effectiveness of the parallel implementation is a share of the computation time and communication time. Figure 21 represents such a share for different

number of grid-nodes. Interestingly, the optimal number of MPI-processes for the given problem size appears to be such that the computational time takes about 30% of the total time, with the rest used for communication events. This fact is explained by almost linear scaling of calculation and communication time for large problem size. The only exception from this trend is the problem size 100. In this case, the number of grid-nodes and number of involved MPI nodes are too small which makes MPI-communication to scale heavily non-linear with number of MPI-processes.

Results and Discussion

The results presented in this section, describe the Atmospheric Pressure Plasma behavior in the generation chamber. The discussed 1D model of plasma provides multiple variables (generally functions of x) for analysis, such as number density, rate parameters, energy content, temperature of species etc. These data are prepared as input parameters for 2D model of the plasma head. Since 2D model mainly deals with plasma advection, mixing, and delivering of species and chemicals to the substrate, the timeframe of this model is determined by flow of the neutral gas. The 1D model has a different time-scale, which is based on oscillations of the RF electric field and is much shorter than the time-scale of 2D model. Therefore, the practically useful data are the variables collected during one complete oscillation of RF and averaged over the oscillation period; these data we refer to as time-averaged. Another type of averaging is typically required for stability analysis; the time-averaged data, as a function of location x, are additionally averaged over the gap size. These data we refer to as time-space-averaged data.

Estimation of Voltage Range

The applicable voltage range for this model is determined by the minimum and the maximum voltage values. We accept the maximum voltage value calculated from gas breakdown estimation (7). Young and Wu [45] discussed a possibility of modeling thermal instability of a glow discharge using fluidic type of a model. Thermal instability occurs when temperature of plasma reaches high values, which is coincident with voltage increase. Thus, there is critical voltage that gives rise to instability. This voltage may set the lower limit for the upper range of applicability. We performed an estimation of the electrode temperature (Figure 22) for a range of voltages that we use in our simulation; the maximum temperature rise at the electrode is found to be 0.125 K. At such low temperature change, we found it unnecessary to further investigate thermal instability. The lower limit of the voltage range is determined by effectiveness of the generation process. Let us consider a general form of mass conservation equation (77), where the drift-diffusion term is represented in terms of a flux *Q*. The drift velocity of electrons in the first term on the right-hand side of (77) is substituted with its expanded form (34).

$$\frac{\partial n_e}{\partial t} + \frac{\partial Q}{\partial x} = \alpha n_e \left|\mu_e E\right| - k_{ie}^{rec} n_e n_p \tag{77}$$

We can ignore the convective-diffusive term, as it just redistributes the existing species over the domain, and focus on the right hand side of (77) with an intention to estimate the minimal voltage required for generation of new species. We formulate the criterion (78) which corresponds to effective generation of plasma

$$\alpha\left|\mu_e E\right| - k_{ie}^{rec} n_p > 0 \tag{78}$$

This is a rough estimation, since it does not account for dynamic effects, but it provides approximate value of the lower voltage limit.

Both ionization and species mobility are functions of the electric field (Appendix A), whereas the recombination coefficient and number density of positive ions are constants provided at initial condition. We specify typical values $\left(n_p = 10^{11}\,\mathrm{cm}^{-3}, k_{ie} = 10^{-7}\,\mathrm{cm}^3/\mathrm{s}\right)$ for these constants and denote the first term of (78) as a function of electric field $f(E) = \alpha\left|\mu_e E\right|$. We move the second term of (78) to the right-hand side and substitute the constants into (79).

$$f(E) > 10^4 \text{ Hz} \tag{79}$$

The function $f(E)$ is numerically evaluated through the range of values provided in Table in the Appendix A. Figure 22 represents behavior of the function $f(E)$ over the long range of voltages, whereas the inset shows a magnified portion of a region, where the criterion (79) takes place.

It is worth mentioning that estimation of the minimal voltage, according to the shown method, is performed in terms of variables averaged over the oscillation period. Thus, the minimal voltage found from (79) is an RMS-value. Figure 22 accounts for this fact and represents the actual value of voltage in place of the RMS. The minimal voltage predicted by criterion (79) is $V_{\min} = 378.7$ V

Time-Averaged Results

We perform simulation of plasma generation in a range of voltages 300-700 V. At each voltage value we investigate the possibility of the plasma reaching the steady state. Figure 23 shows a typical result of such investigation. Time-space-averaged number density is plotted against RF-cycles showing the trend for stability (600 V) or instability (350 V). The simulation calculated at 380 V shows a slight decrease on this plot. However, this voltage is validated at 2000 RF cycles, where it exhibits steady behavior. At the same time, voltages equal to or lower

than 370 V lead to permanent decrease in number density, regardless the length of the simulation. This investigation confirms the minimal voltage value of approximately 378 V

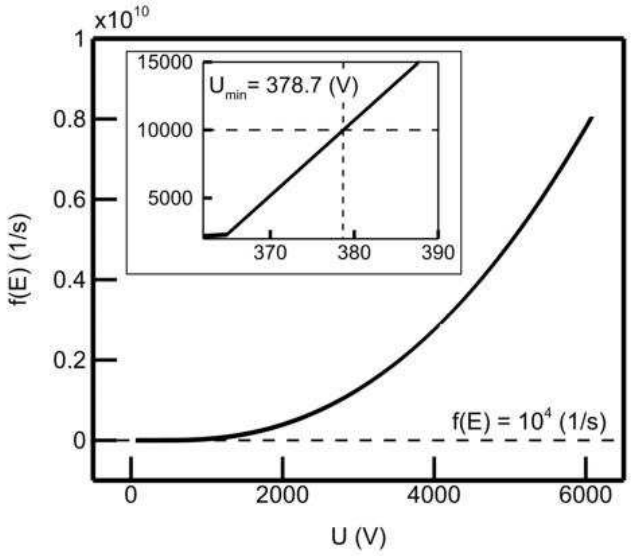

Figure 22. Minimal voltage search. The main plot shows general behavior of a characteristic function $f(E)$ of the electric field plotted versus the applied voltage. The inset shows a magnified portion of the curve, where the minimal voltage is found

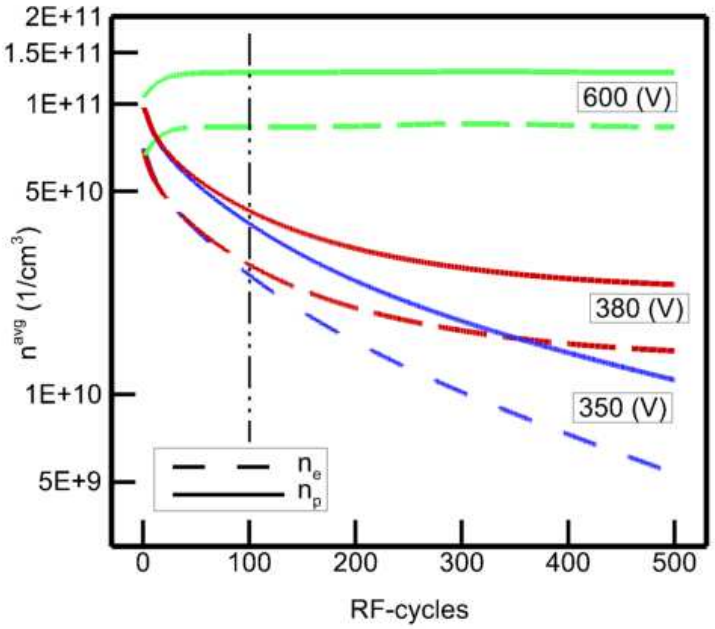

Figure 23. Stability of plasma discharge

An interesting observation is that the number density of electrons in Figure 23 consistently starts from a lower initial value. We believe that this effect owes its existence to non-physical initial condition. The species are uniformly distributed over the domain. When the electric field is suddenly applied, electrons, being faster particles, escape into the nearest electrodes. This loss immediately offsets the initial number of electrons. Ions are slow, and they do not penetrate the electrode; this is why their initial quantity does not change so drastically.

Figure 24 provides time-space-averaged number density of electrons and positive ions in the range of voltages 378-700 V. Depending on the specific process responsible for activation of a chemical precursor, a different number of electrons and ions is required in the mixing chamber. The data plotted in Figure 24 helps to estimate the minimal voltage that supplies sufficient amount of the species at each particular case. The averaging is carried out after 3000 RF cycles for each involved voltage.

When the averaged number density of plasma species is found, it is good to know how the species are distributed between the electrodes. Number density of the species (Figure 25) expectedly provides high values at the center of the domain and lower values at the edges. Electrons have zero number density at the wall, since there is absolute absorption. The quantity of positive ions exceeds that of electrons at every location on the domain; this surplus constitutes slightly positive total charge of plasma.

Since the total charge of the plasma is positive, the electric field (Figure 26) takes a specific shape responding to the growth of distortion, in accordance with Poisson equation. The absolute values of electric field are symmetric with respect to zero level which perfectly correlates with the symmetry of the sinusoidal waveform of the applied voltage.

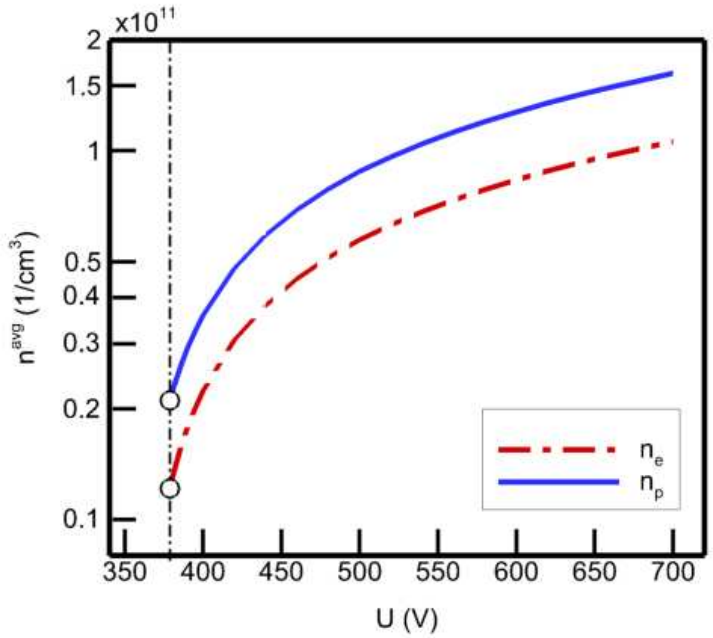

Figure 24. Mean number density achieved in the stable mode vs. externally applied electric potential

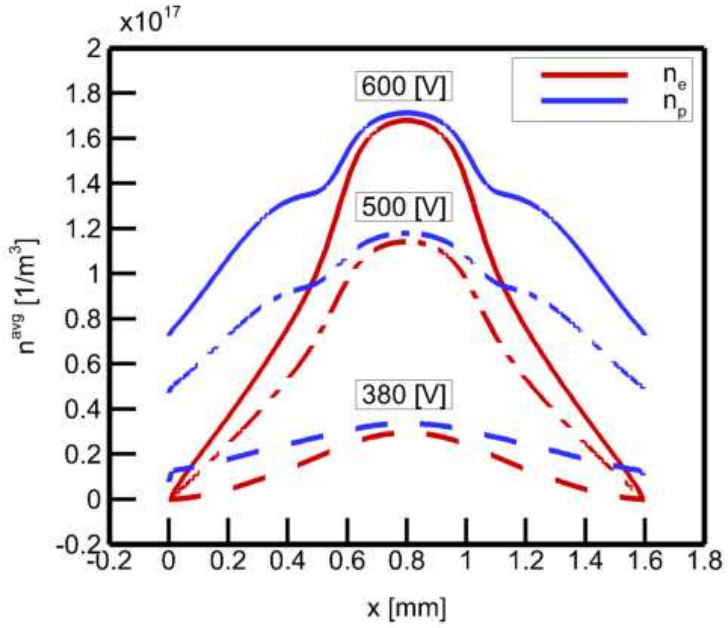

Figure 25. Distribution of time-averaged number density of electrons and He^+ ions over the gap

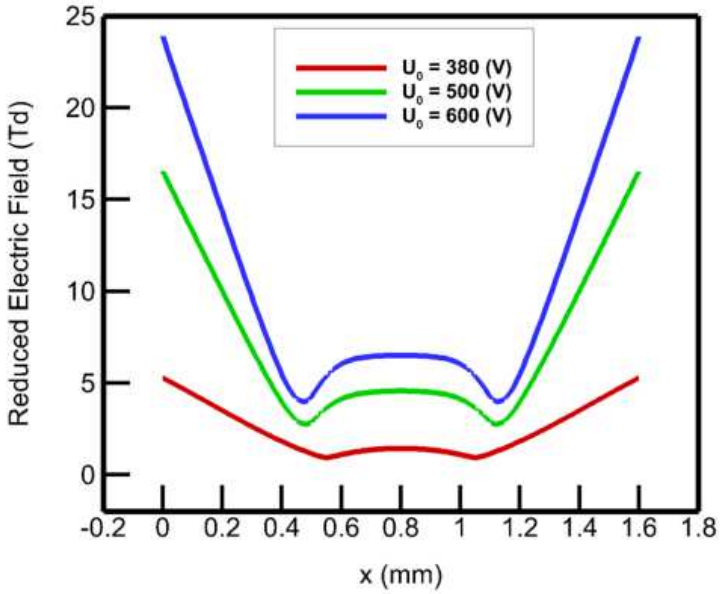

Figure 26. Distribution of time-averaged reduced electric field over the gap

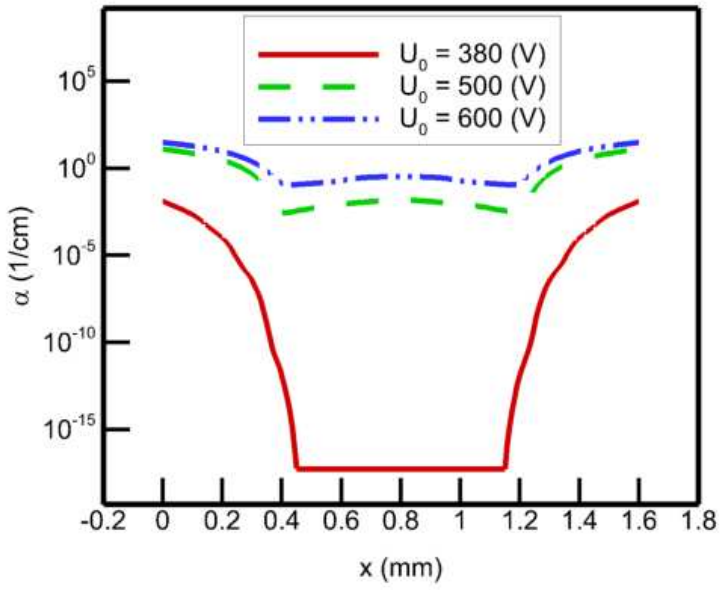

Figure 27. Time-averaged ionization curve

Ionization curve (Figure 27) exhibits a good match to electric field. The relation between ionization coefficient (α) and reduced electric field (E/N) is not linear (Figure 12.(b)), which naturally transfers into the curvy shape of ionization at the central part of the domain, where electric field is small and almost constant. The highest ionization values are observed at the edges of the domain, which is a consequence of high electric field in this region. A rather peculiar phenomenon for ionization curve occurs at low voltages (380 V), when the electric field at the central part of the domain is not high enough to provide recognizable ionization, but ionization at the edges is sufficient to sustain plasma.

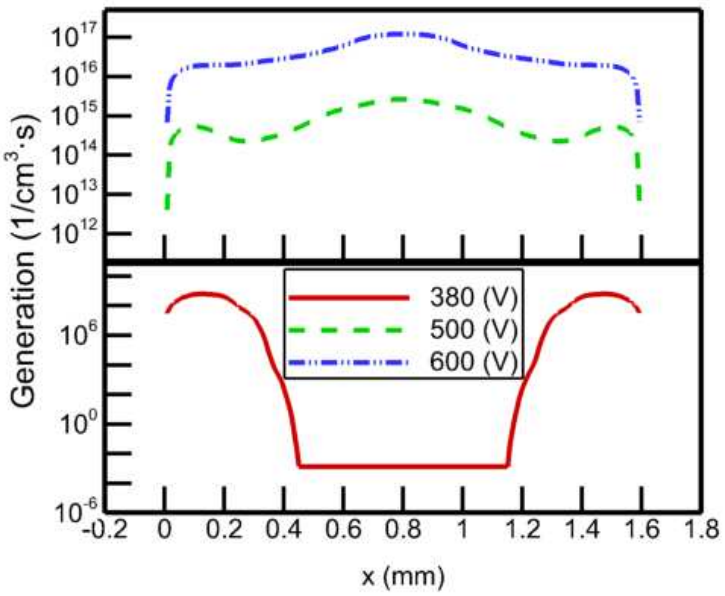

Figure 28. Time-averaged generation term

The generation term (Figure 28) shows high values at the center, where large number density of electrons is multiplied by relatively small ionization coefficient resulting in moderate number of generated species, as well as at the edges (the peaks are especially pronounced for lower voltages, like 380 V and 500 V in Figure 28), where not high number density is

complimented by large ionization coefficient yelding a good number of new species. The generation at the edges is the major electron supply at low voltages.

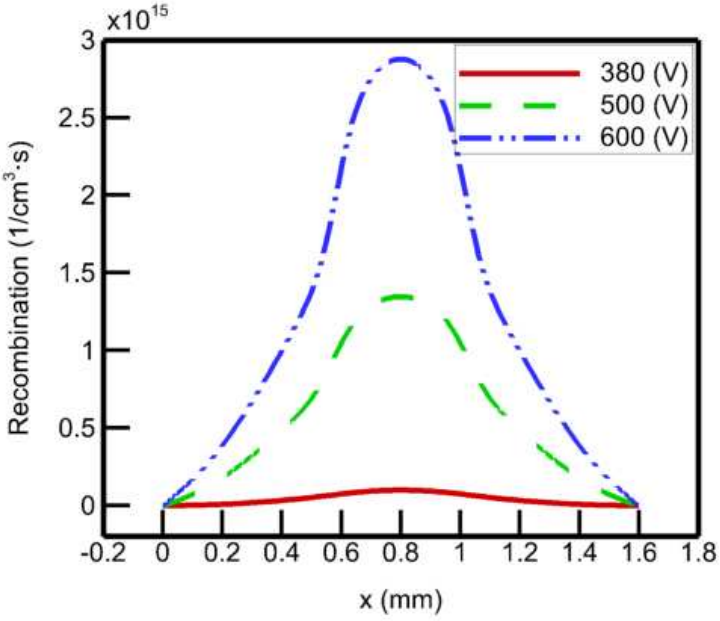

Figure 29. Time-averaged recombination term

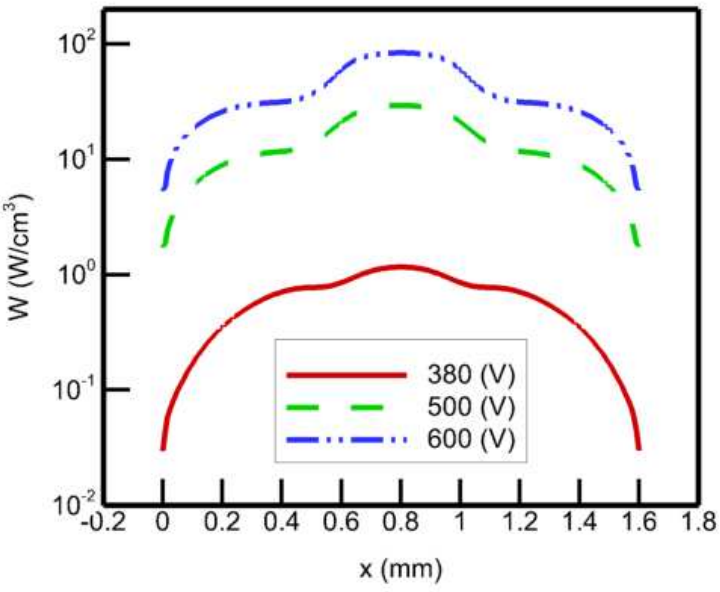

Figure 30. Time-averaged power dissipation

Recombination term (Figure 29) expectedly exhibits a large peak at the center of the domain, where number densities of both species are at the maximum. This is not surprising considering the fact that recombination term consists of multiplication of the two. Behavior of recombination term generally does not change with alteration of applied voltage.

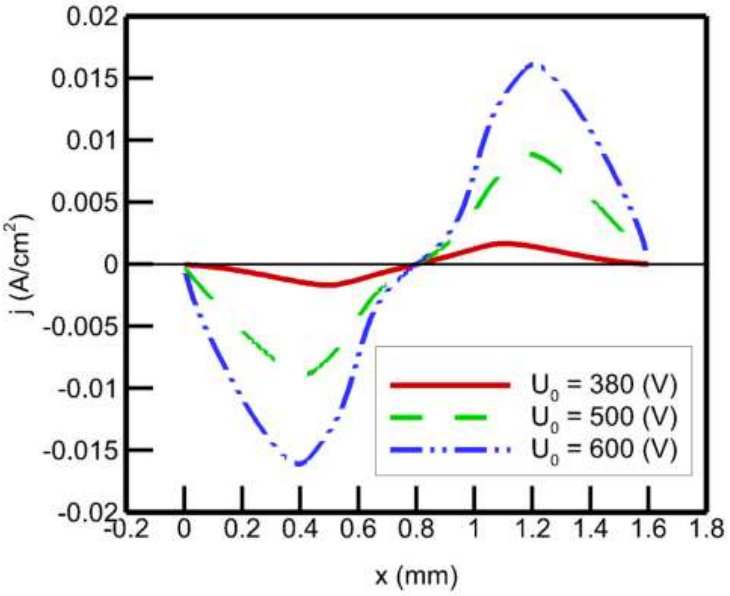

Figure 31. Distribution of time-averaged current density in the gap

Power dissipation (Figure 30) depends mostly on the current density (Figure 31) and the electric field (Figure 26). The shape of electric field and current density shown in this section are not good indicators of the expected shape of the power dissipation. The reason is that these values are already time-averaged, whereas the power dissipation is calculated from instant values of electric field and current density and then time-averaged. The averaged form of power dissipation is represented by the right-hand side of (43). This case clearly illustrates that average value of an integral is not equal to the integral of average values.

The values of current density (Figure 31) are determined through time-averaging of $j(t) = e\left(n_p v_p^d - n_e v_e^d\right)$. In this expression, the second term is dominant, because velocity of electrons is few orders of magnitude larger than that of ions, while their number density is in a comparable range. Within the first half of the RF-cycle, electrons accelerate towards one electrode; within the second half of the cycle, they accelerate towards the opposite electrode. In both cases, the highest time-averaged velocity is reached in the vicinity of the electrodes and the lowest time-averaged velocity is at the center. When velocity is multiplied by number density, which exhibits the opposite behavior, the highest result (peaks in Figure 31) is found around ¼ and ¾ of the domain.

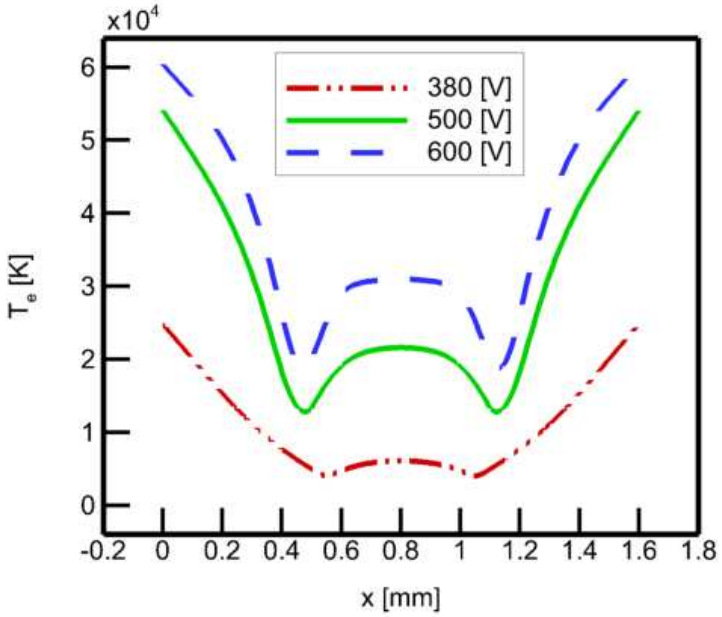

Figure 32. Distribution of temperature of electrons in the gap

Temperature of electrons (Figure 32) is computed from mean energy taken from BOLSIG+. The central hill is formed due to electrons passing this region twice per RF-cycle, losing their energy in the form of heat dissipation. The high temperature at the edges is due to

high electric field at this location. Such result is explained by mean energy growth (Figure 12.(d)) with increase of electric field. Therefore, high electrons' temperature is expected in the vicinity of the electrodes.

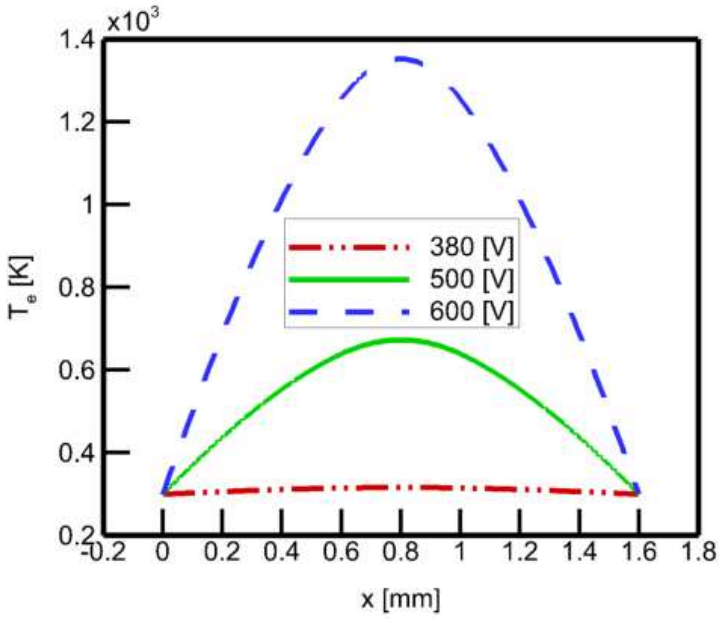

Figure 33. Distribution of ions temperature in the gap

Temperature of ions (Figure 33) is calculated at the last RF-cycle of the simulation as a solution of thermal diffusion equation (43). One can notice that the temperature at the center of the domain may reach high values, but the actual heat flux over electrodes remains small. This is why temperature of the electrodes (Figure 22) does not experience a significant increase. Overall temperature of APP is determined by ions with contribution of electrons' temperature in the form of ohmic heating (43).

Transient Results

We found surface plots (Figure 34) helpful for understanding of plasma transient behavior, as they immediately highlight defects and anomalies in plasma. The plots represent

evolution of plasma parameters in time, with the vertical axis corresponding to the gap between the electrodes and the horizontal axis corresponding to the simulated time [43]. Data collected in these plots are instantaneous rather than averaged; therefore, specific details of each oscillation are well pronounced.

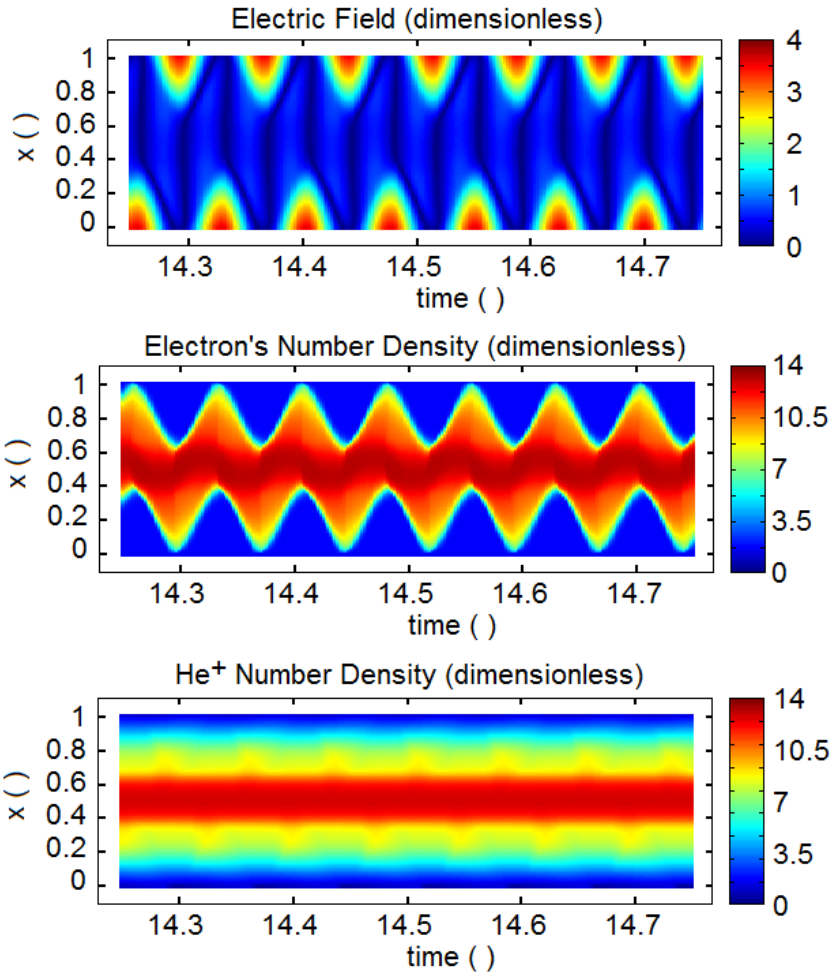

Figure 34. Evolution of plasma. The vertical axis is dimensionless x along the gap. The horizontal axis is dimensionless time

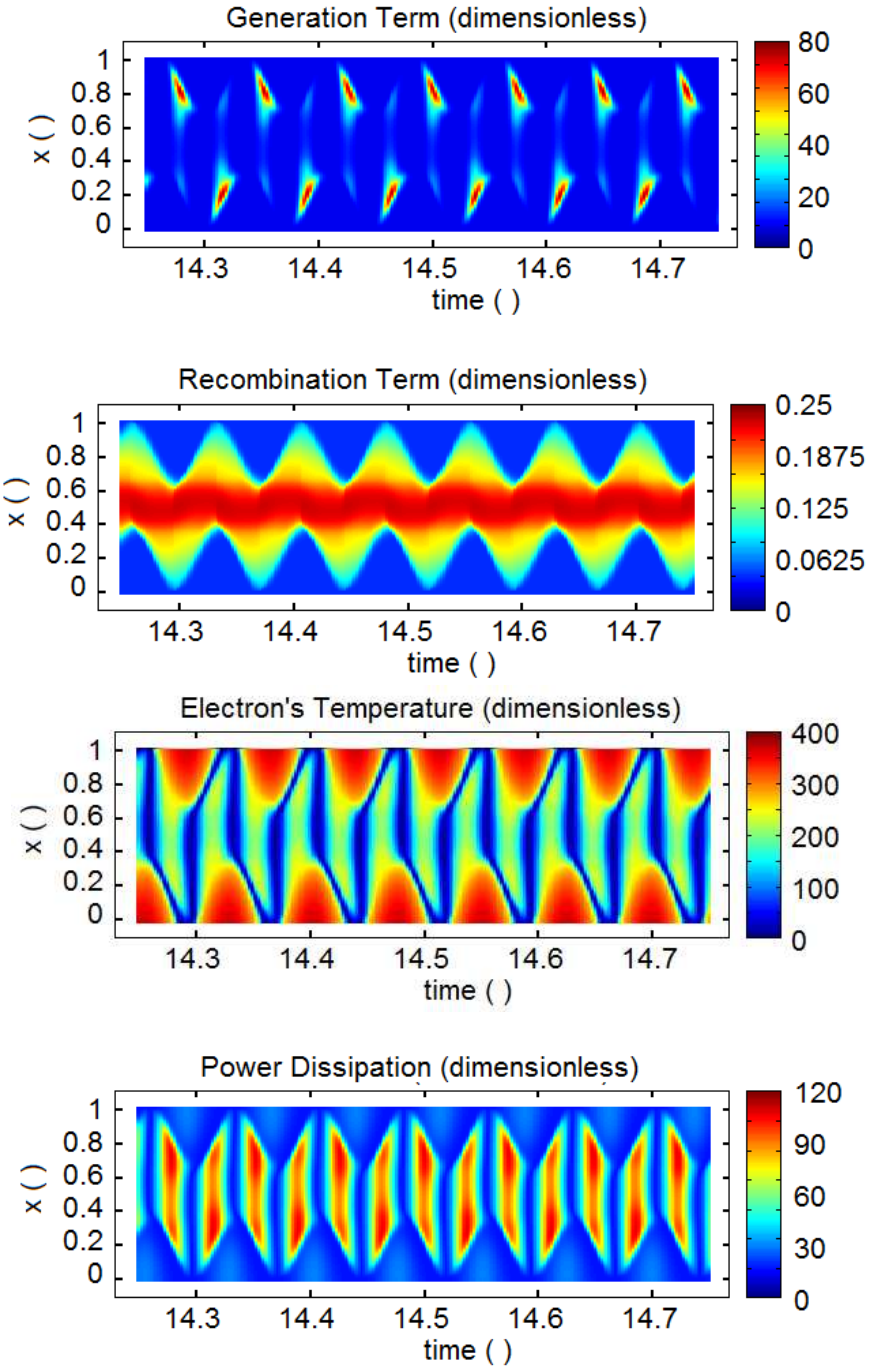

Figure 34. Evolution of plasma. The vertical axis is dimensionless x along the gap. The horizontal axis is dimensionless time(continued)

A good example of using surface plots is the investigation of the generation process.

When the pattern of generation (Figure 34) is compared to that of number density, one could

realize that the peak of generation does not correlate with the peak of number density. We consider dimensionless time of 14.3 in Figure 34. The generation term has a peak right after this time mark. We take a cross-section of the generation and number density when generation is at maximum (right after time mark of 14.3) and plot them next to each other (Figure 35). According to Figure 34, the highest number density of electrons is around $x = 0.6$ and the highest generation happens around $x = 0.2$.

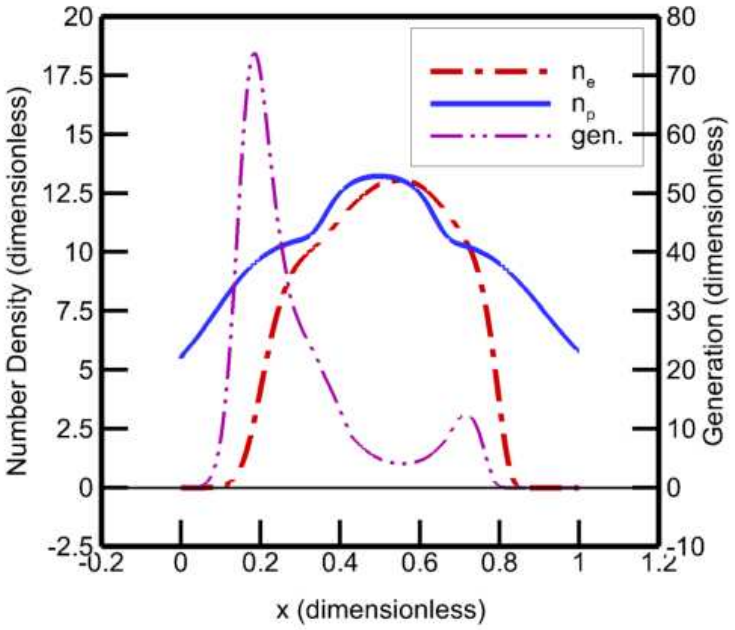

Figure 35. Generation term aligned with the species number density. This is a cross-section taken from surface plots (Figure 34) at the peak of generation, right after $t = 14.3$

At $x = 0.2$ the difference between ions' and electrons' number density is high leading to significant distortion of the electric field. In accordance with Poisson law, the distortion transfers to the high electric field and subsequently to the high velocity of the species. Thus, flux of electrons at $x = 0.2$ is larger than that at $x = 0.6$, where electrons have the peak population. Another factor influencing the maximum generation is the high ionization coefficient as a

consequence of the high electric field at $x = 0.2$. The combination of these factors results in non-correlation of the peaks of the generation term and species' number density.

Engineering Insights

One of the parameters that favor experimental investigation is the sheath thickness. There are different methods proposed for theoretical estimation of the sheath. For example, the Lieberman [78] and Godyak/Sternberg [79] models are well correlated to experimental measurements [80], in the case of low pressure plasmas. For atmospheric pressure plasmas, the Young and Wu [45] model suggests using 90% of maximum electric field value as a criterion for estimation of the sheath position. We found that this criterion provides not pleasing results with rapid changes in the sheath curve due to disturbances generated by moving species.

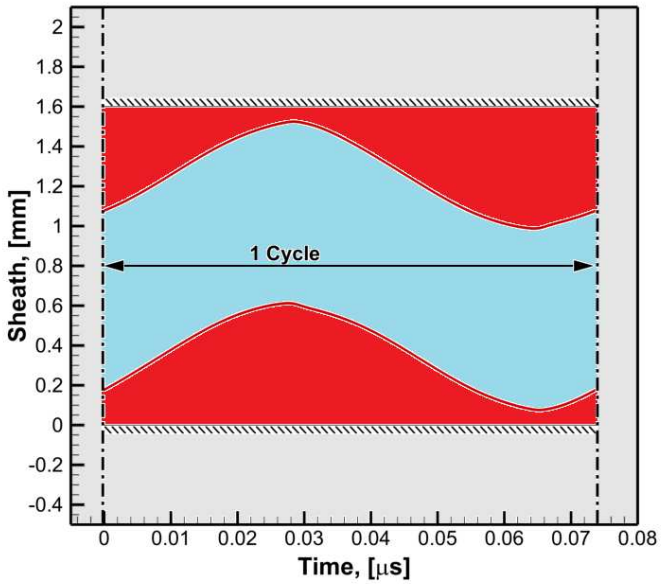

Figure 36. Sheath thickness within oscillation when plasma is at the steady mode

Chirokov [43] proposes to set the position of sheath at the point where number density of electrons is smaller than space-averaged instantaneous number density. Figure 35 represents

results obtained according to Chirokov's approach. We found this criterion quite reasonable. It provides smooth results and splits the domain into three parts, two of which (shaded in Figure 36) contain very small amount of electrons with sufficiently large number of positive ions, and one (central white in Figure 36) contains major portion of electrons and ions.

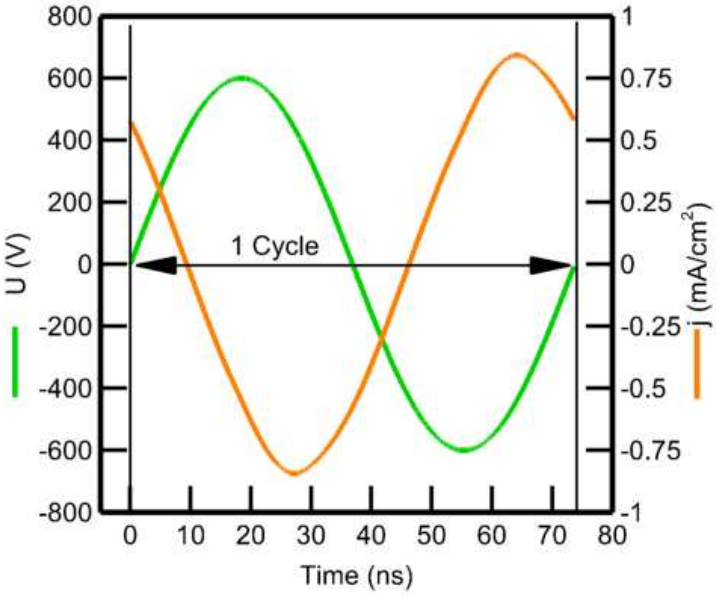

Figure 37. Phase shift of current at the electrodes relative to the applied voltage (600 V) in plasma at the steady mode

Another parameter that can be acquired experimentally is the phase shift (Figure 37) of the current relative to the applied voltage. We calculate the current density value at the electrodes using the boundary conditions. The electrode's current density, being multiplied by the area of the electrode, provides the current that could be compared to experimental results.

The phase shift observed in simulated plasma is equal to $\varphi \approx 5/4\,\pi$ at 600 V. This value corresponds to the ratio of $\text{Reactance}/\text{Resistance} = Tan(\varphi) = 0.938$. The simulated plasma is almost equally proportioned between capacitive and resistive modes, with resistive mode pronounced slightly more.

The 1D model of plasma allows for some basic engineering estimation that could help in building a real plasma setup. For example, temperature of electrodes (Figure 22) provides thermal mode of plasma operation at a certain voltage. These data assist in decisions on the necessity of cooling measures for the proposed plasma head.

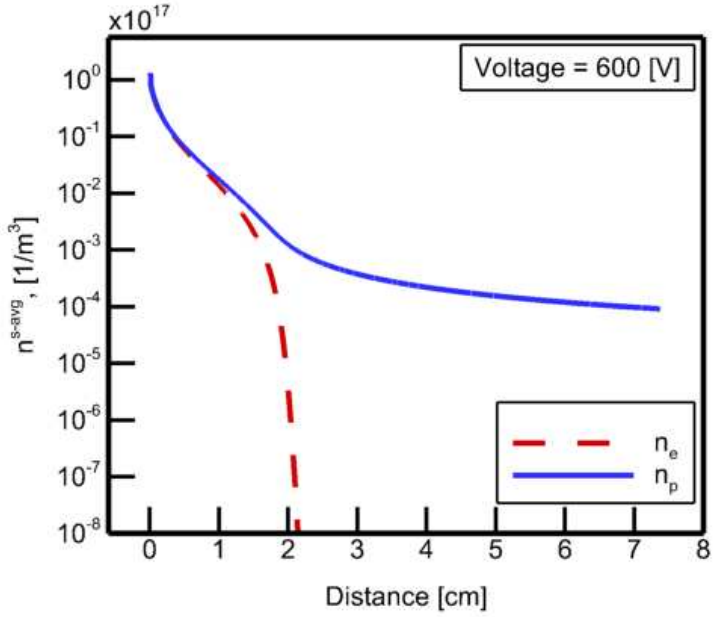

Figure 38. Plasma fade estimation when electric field turns off at the 100th RF-cycle.

Another useful estimation can be done when the electric field is turned off after plasma reached the steady mode of operation. To better illustrate this example, we pick the external voltage of 600 V and simulate plasma behavior for 100 RF-cycles. According to Figure 23, plasma at this voltage reaches the steady state within the specified number of cycles. At the 100th RF-cycle we turn off the external voltage and continue the simulation until number density of species falls below a certain limit. It takes about 5000 RF-cycles to provide data depicted in Figure 38.

To further emphasize the essence of this test, we assume that neutral gas flows with velocity of 10 m/s. The plasma is caught by the neutral gas and is advanced along the channel

due to convective forces. Despite the absence of external electric potential, the electric field is still generated in the advancing plasma because of the differences in charge distribution. The recombination process continues until electrons and ions are still present at the domain. Additional loss of electrons occurs due to their absorption at the wall. Thus, the quantity of electrons decreases rapidly and reaches a very low number at just over 2 cm of the free flight (Figure 37 does not show further electrons decrease as their number density becomes too small). It is possible to pull electrons out of plasma for longer distance using special techniques [81], but in regular case, electrons beam is short in comparison to that of ions.

Ions participate in the recombination process as long as electrons are available. When the quantity of electrons becomes very small, the recombination has almost no effect on the number of ions remaining on the domain. Provided that there is no other ions' loss mechanism, these species fly in a relatively large number for a quite long distance. Figure 38 estimates the ions' jet length is greater than 7 cm. This case has an artificial nature, but it still can be used for a rough estimation of plasma life when a plume of plasma leaves the gap between the electrodes. From a practical standpoint, this consideration could be quite helpful at the design stage.

MODEL OF PLASMA CONVECTION

General Description

Plasma convection along the channel formed by parallel walls of the plasma head is governed by convective motion of the neutral gas. We did not consider motion of neutral gas in 1D model of plasma generation, because the difference in characteristic time of the two processes is tremendous. While the gas moves along the characteristic length of the gap between the electrodes, the generation process evolves thousands of iterations. Thus, we may assume that plasma parameters such as the number density, the electric field generated by the applied potential and by charged species, the rate coefficients, energy of the species, and others can be averaged and advected along the channel using the time-frame of the gas flow; at the same time, accounting for electric response of plasma, and for velocity field imposed by the flowing gas.

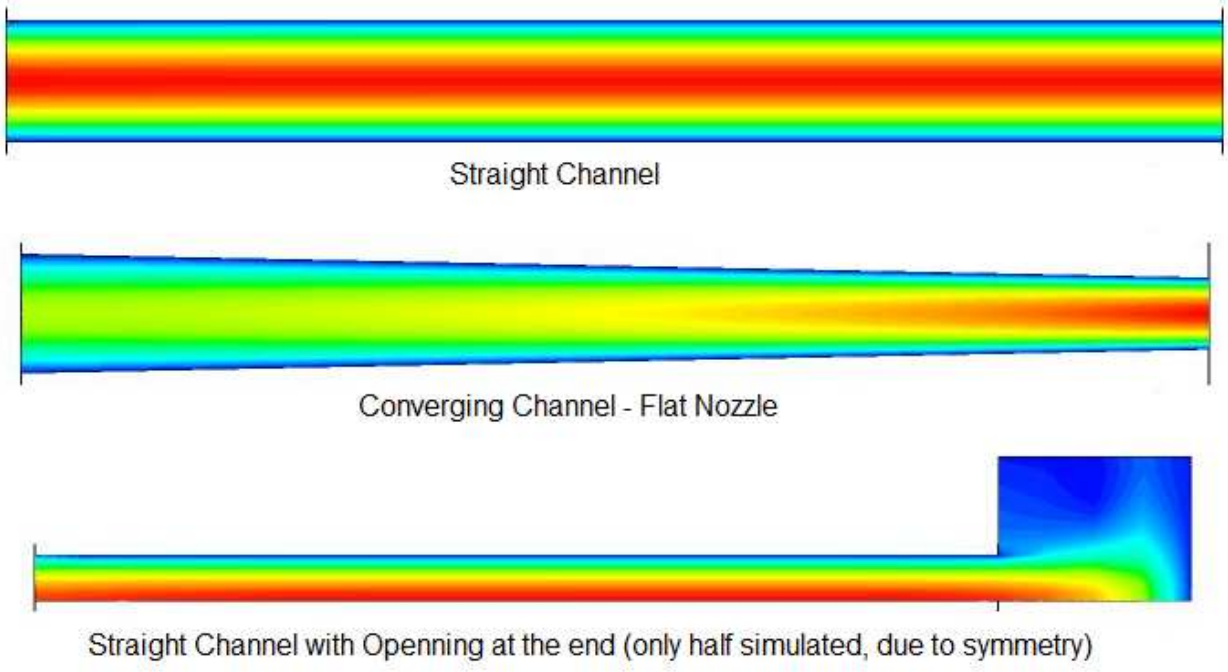

Figure 39. Typical geometry of the channel proposed for numerical investigation

The velocity field of the neutral gas is calculated using ANSYS, as there is no reason to expand the numerical solver of the plasma problem to solve Navier-Stokes equations. The computational domain is constructed using ANSYS ICEM, the fluidic calculation is done via ANSYS CFX. There are two typical geometries considered for the plasma channel (Figure 39). The geometry of the channel could be altered within a wide range. It is also possible to implement turbulence model, as the final result must contain only the velocity field, which would account for any additional effects. Plasma species can be imagined like a cloud of particles that is driven by the gas flow, regardless of its laminar or turbulent nature, but due to the collective behavior of the plasma particles as a reaction to the imposed and self-generated electric field, the trajectories of plasma species would not necessarily coincide with those of neutral molecules. At the same time, ionization and recombination processes contribute to a change in number density of plasma species. The loss of the species to the walls also provides a physical mechanism different from the behavior of neutral gas. This is why, in addition to the solution of the fluidic problem, we have to solve Poisson equation on top of the advected distribution of plasma, calculate rate parameters and adjust the number density of the plasma accordingly.

The velocity field is internally stored in ANSYS in a specific form with some parameters accessible to the user, and some parameters hidden. The extraction of the field components provides spatial coordinates of the nodes with values of velocity, velocity gradient, pressure, temperature and some other parameters specified at the given locations. Very important information on connectivity of the nodes is missing and cannot be extracted from ANSYS. This results in the velocity field being just a random cloud of nodes without any physical connection. The nodes could be sorted and matched to some type of a pattern to resemble a type of a mesh, but it is not a simple task when unstructured mesh is in use.

We would like to use unstructured mesh in our convective model, as it approximates complicated geometry [82] with much better accuracy than regular mesh. The aspect ratio of the triangles in a triangular unstructured mesh can be improved significantly in comparison to that of the regular mesh. At the same time the calculation process becomes more complicated as we have to work in terms of each particular mesh element and not in terms of separate nodes aligned with coordinate axis. Thus, we have to develop a specific approach to the computational domain and to the numerical algorithm to handle this model.

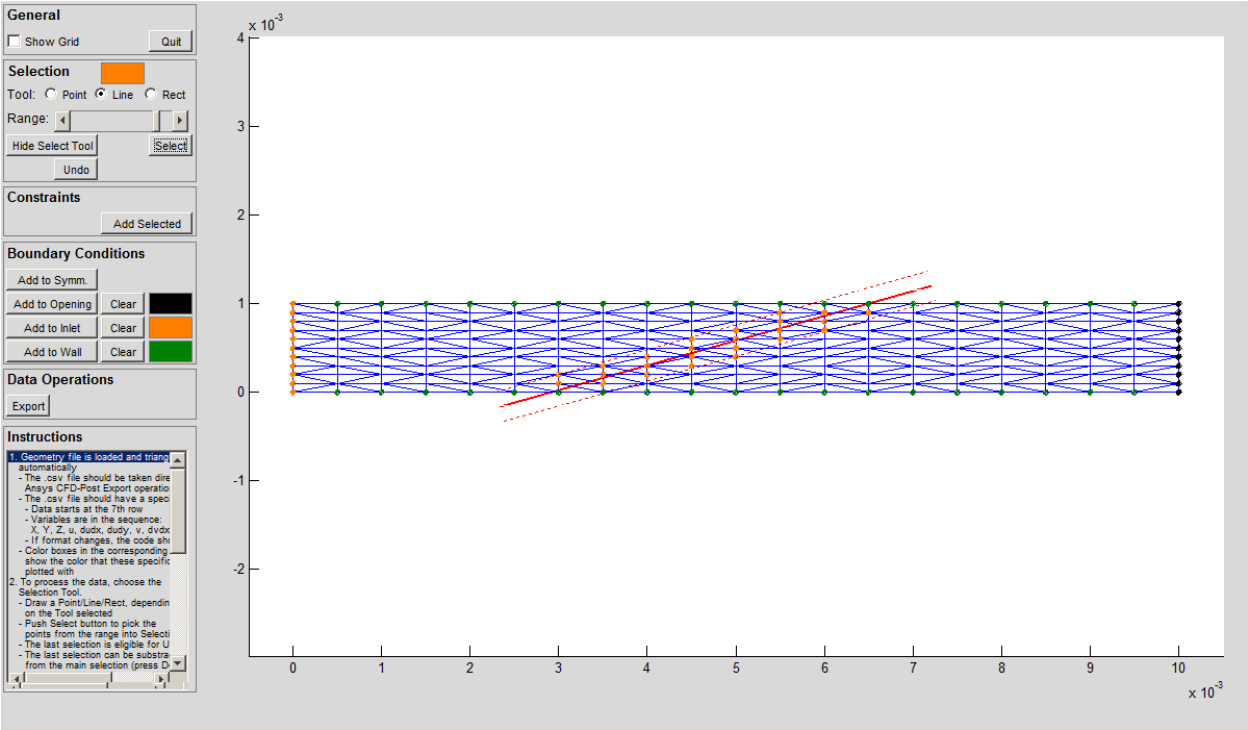

Figure 40. The developed software module for triangulation and processing of ANSYS results prior to input to the numerical code

Since the input velocity field is represented as a random cloud of nodes, we have to construct triangular elements and find the connectivity information. In order to perform this task, we develop a separate software module using Matlab [83]. The primary objectives of the module are to input the random cloud of nodes, to order the nodes and triangulate them utilizing the

Delaunay [84] triangulation method, to set the boundary information to those elements that contain a domain boundary as one of their edges, finally, to export the updated information about the velocity field in a special data file that can be used by our numerical code for advanced calculations.

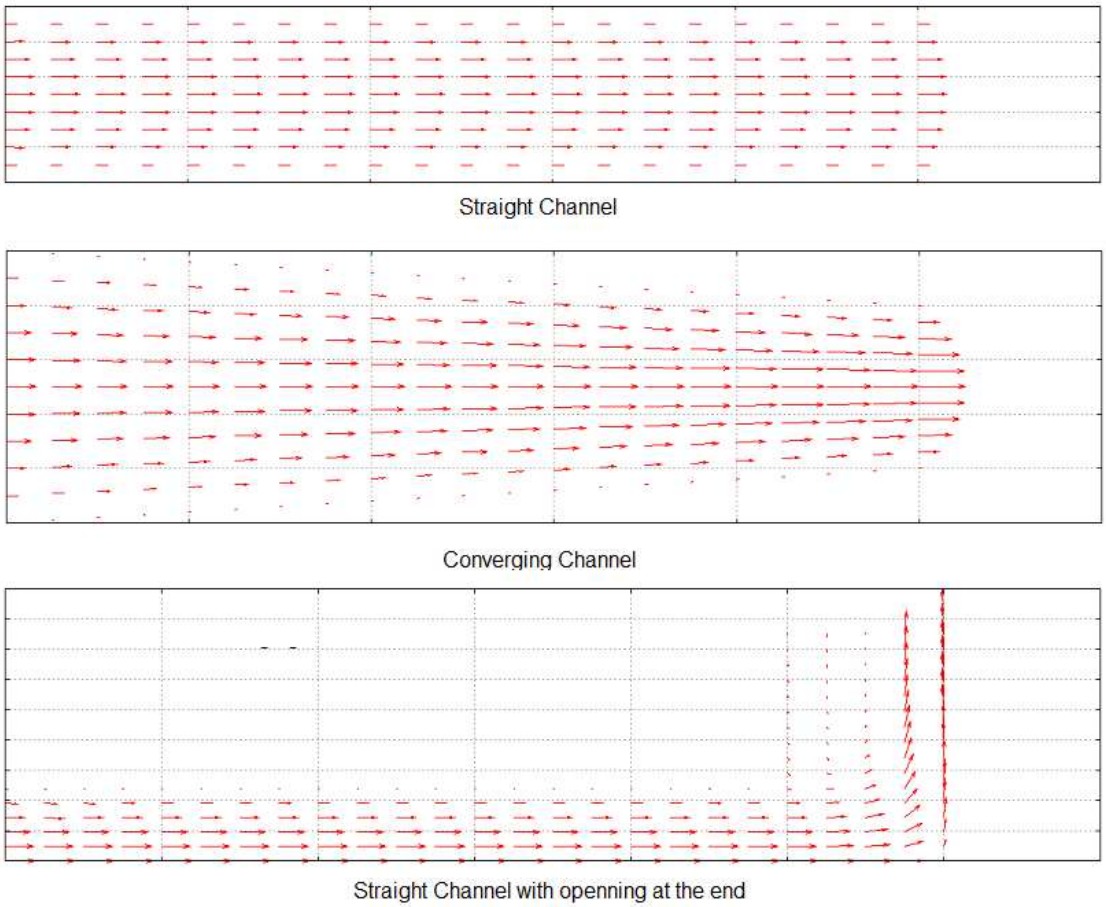

Figure 41. Typical channel geometry with velocity field, as it is seen in the numerical code

Figure 40 shows the main window of the developed module with loaded data for straight channel. The data is automatically triangulated with the Delaunay algorithm. The different colors of the nodes on the mesh correspond to defined boundary conditions for Inlet, Walls, and Outlet. The red solid line with parallel dashed lines represents a selection tool – all the nodes that fall in

the range shown by the dashed lines would be selected and available for modification, assignment of boundary condition, or setting the confinement information for the domain.

There are few selection tools developed to widen the range of accuracy for the selection procedure. The software module features interactive user environment where mouse and keyboard may be used to enter the necessary data, which is depicted in the real time. Additional components are easy to add to the module as the code, written in Matlab, is open for further development.

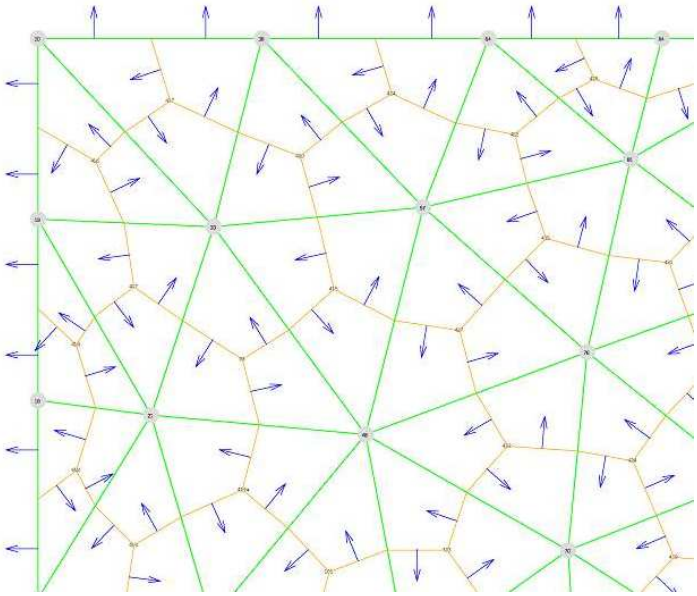

Figure 42. Unstructured mesh with finite elements (orange) and normal vectors (blue)

The data supplied by the software module includes the physical data on velocity field in the considered geometry, as well as connectivity information and boundary conditions. This data is analyzed by a numerical code written in *C*-language. The first result of such an analysis is the proper input of the geometry of the calculation domain and proper interpretation of the velocity data. This result can be validated by plotting of the input data in the numerical code, as it is shown in Figure 41, where typical geometries for the plasma channel are shown in the form of vector-field.

The nodes topology is brought in order by Matlab software module, the numerical code converts these data into a set of finite volumes. Each triangle of the unstructured mesh is subject to pre-processing, which calculated the center of the triangle and the centers of its edges. The edges' centers connect to the triangle's center, thus splitting a mesh element into three parts (Figure 42). Each part belongs to the vertex that is in the closest proximity. Hence, each vertex is surrounded by such parts of the mesh triangles. All parts combined around the vertex, create a 2D finite volume which could be seen as a shape enclosed with orange borders in Figure 42. For example, the orange sectors in Figure 42 correspond to the portion of finite volume that belongs to the vertex v_2, the green sectors – to the vertex v_1, and the blue sectors – to the vertices v_0. There different ways to build finite volumes on unstructured 2D mesh [85, 86]. In addition to the method we have chosen, the finite volumes could be represented by the mesh triangles with the physical properties determined at the centers of the volumes.

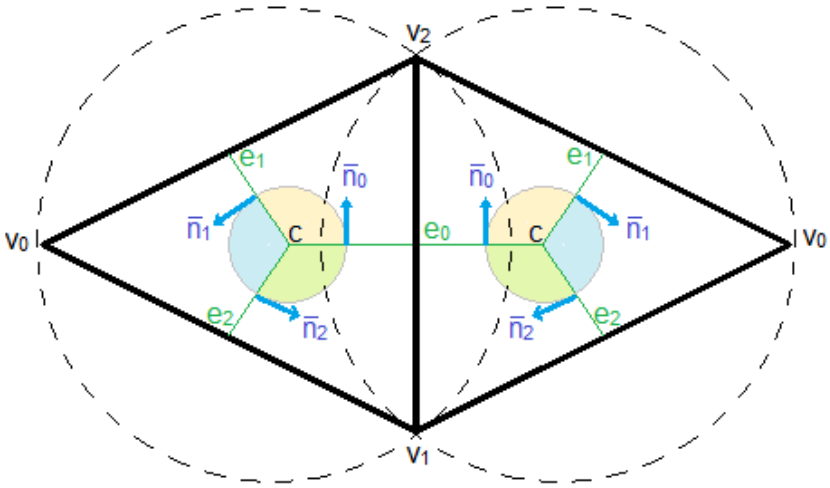

Figure 43. Typical mesh triangles and indexing of geometrical elements

The normal vectors (the blue vectors in Figure 42 and Figure 43) are calculated at the borders of the finite volumes, in order to project the species fluxes to the boundary of the finite

volume. The direction of the vectors is chosen such as it follows the direction of counting the vertices (clockwise or counter-clockwise). When direction of vertices counting reverses, as it is shown in the right triangle of Figure 42 relative to the left triangle in the same figure, the normal vectors automatically account for the change. The local indexing is chosen in such a way that an edge, a line (the border) connecting the edge to the center of the triangle, and the corresponding normal vector all receive an index of the opposite vertex. Thus, the contribution of the fluxes – positive or negative – for each particular part of the finite volume is determined according to the direction of the normal vector, which is constant relative to the vertex that contains the considered part.

The local indices have the following relations. For the vertex $i_0 = 0,1,2$, the other two vertices are determined by $i_1 = (i_0 + 1) \bmod 3$ and $i_2 = (i_0 + 2) \bmod 3$. The same are the indices for the edges connected to the vertex i_0. For the edges the same relations determine the two vertices forming the edge, while the index of the edge corresponds to the opposite vertex. Let us consider a line connecting the center of an edge and the center of the triangle, e.g. $e_0 c$, the two edges *not* connected to this line are also determined by $i_{e1} = (i_{e0} + 1) \bmod 3$ and $i_{e2} = (i_{e0} + 2) \bmod 3$. This relation would be useful when we discuss dynamic blending in the next chapters.

After the geometrical part of the computational domain and velocity field are initialized, we set initial number density and electric potential at the Inlet of the domain. In order to accomplish this task, we use the averaged data provided from 1D model of plasma generation. The rest of the physical plasma parameters are not important as they can be calculated during the simulation based on the species' number density and distribution of electric potential.

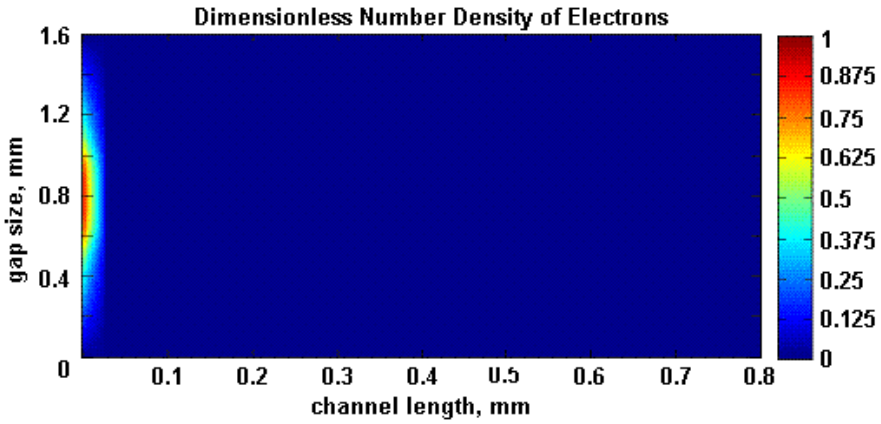

Figure 44. Initial number density of electrons

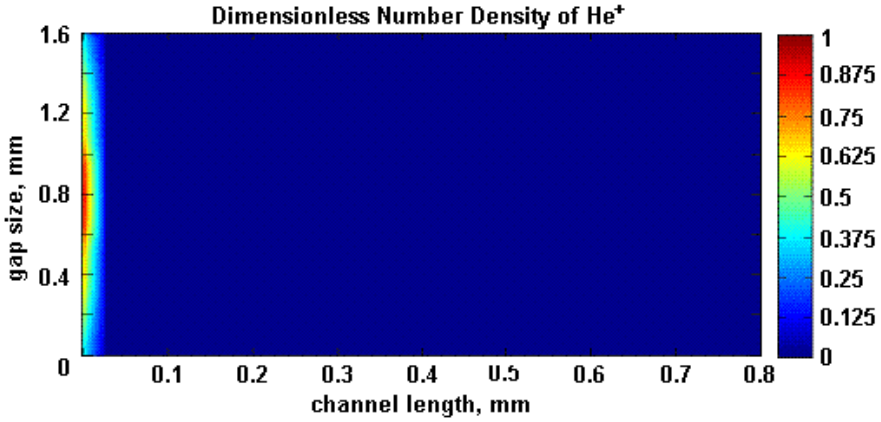

Figure 45. Initial number density of positive ions

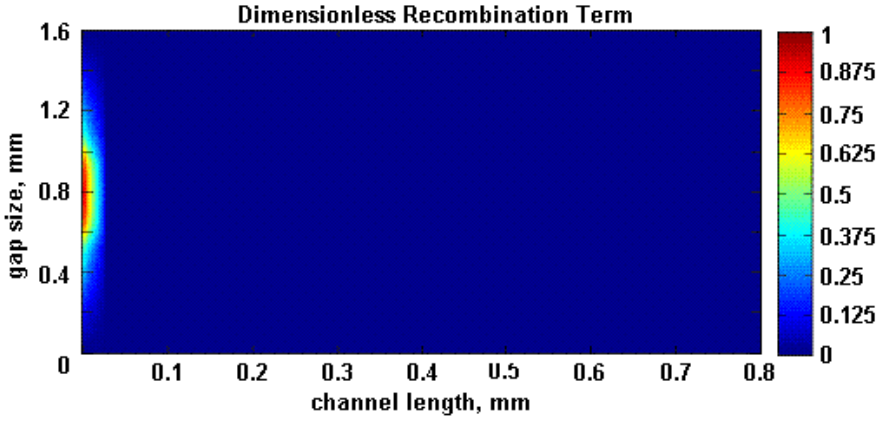

Figure 46. Initial distribution of recombination term

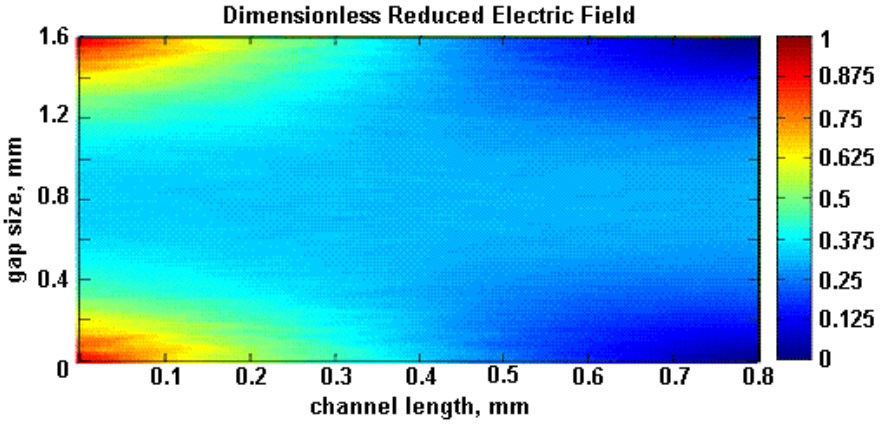

Figure 47. Initial distribution of reduced electric field

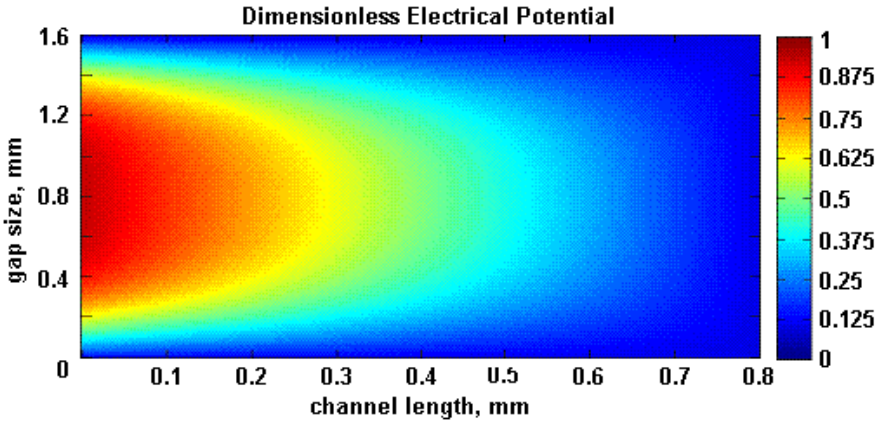

Figure 48. Initial distribution of electric potential

The initial data shown in Figures 44-48 is calculated on a domain discretized with the use of the unstructured mesh that consists of 2500 nodes and 4752 triangles. The initial data calculated on 1D domain of 1000 nodes is fit to the inlet of the 2D problem and interpolated between the inlet nodes. Other plasma parameters at initial moment of time could be seen in Appendix C. The average profiles shown for 1D problem can be observed for number density of the species (Figure 44 and Figure 45) and for recombination (Figure 46). The reduce electric field (Figure 47) and the electric potential (Figure 48) are calculated based on the initial

distribution of the potential provided from 1D problem. The Poisson equation is solved in order to find electrical properties at the domain at the initial moment of time.

Numerical Technique

The numerical technique applied for 2D case of plasma advection can be selected from a multitude of available models and approaches. The most common are central difference descritization and upwind numerical approximation. Regardless the numerical model, the finite volume approach requires calculation of the species number density at the interfaces between the finite volumes. The value at the interface is used for determination of the flux that is crossing the boundary leaving one finite volume and entering another one. Tracking the fluxes and properly inserting them into the governing equations yields with redistribution of the species on the domain. The interfacial value can e calculated in accordance with one or few numerical schemes that are used in the problem. The central difference descritization calculates the number density based on exact interpolation at the point of interest. This approach is not beneficial when gradients of the conserved values are high. In fact, the scheme leads to the saw effect which is often referred to as instability of the central difference scheme.

In order to cure the instability, the interfacial value of number density can be calculated with the use of the node which is placed upwind in relation to the considered point. This scheme has a name of upwind numerical approximation. The first order approximation is obtained by assuming that the number density is constant everywhere within the finite volume, including the boundaries between the elements. The interfacial value, in this case, is determined as the largest value of the two finite volumes. The second order scheme is based on linear interpolation of the conserved variables around the upwind node. At the considered point, the velocity vectors are

considered, which helps to determine which node is the upwind one. The mean gradient at the upwind node is used to interpolate the upwind number density to the considered point. In the general case, such interpolation yields with higher interfacial value than central difference scheme. The saw effect is completely eliminated by the upwind approximation, but the approximation introduces excessive numerical diffusion, which is culprit of accuracy.

The advantages of the central and the upwind numerical schemes may be combined, and the disadvantages significantly reduced, when the two schemes are used together. The contribution of each scheme is determined by a weighting factor $0 \le \alpha \le 1$. The combination of the schemes is referred to as blending. This approach may be used with a static blending factor or with a dynamic one. In the later case the accuracy usually increases, while the calculation time decreases. More details on the discussed approaches are shown in the next chapters.

Interpolation in the Mesh

Due to the use of unstructured mesh in our model, we have to implement special numerical techniques for solution of both, continuity equation and Poisson equation. The governing equations remain valid with the exception that they are written in a general form (gradients and divergence in place of partial derivative).

$$\frac{\partial}{\partial t} n_e + \nabla\left(\mu_e E n_e - D_e \nabla n_e\right) = \left(\alpha - \eta\right) n_e \left|v_e^d\right| - k_{ie}^{rec} n_e n_p \qquad (80)$$

$$\frac{\partial}{\partial t} n_p + \nabla\left(\mu_p E n_p\right) = \alpha n_e \left|v_e^d\right| - k_{ie}^{rec} n_e n_p$$

$$\nabla^2 \phi = -\frac{e}{\varepsilon_0}\left(n_p - n_e\right) \qquad E = -\nabla \phi$$

The numerical scheme for the continuity equation is based on analysis of fluxes that cross the boundaries of finite volumes. Let us consider a finite volume presented in Figure 49. The

figure shows a small portion of unstructured mesh, where six triangles connect to a vertex $\bar{\mathbf{v}}$. Each triangle has a center at the point $\mathbf{c}$ which is calculated as an average of coordinates of the three vertices of the triangle and represents a center of mass. The points $\mathbf{e}$ represent the centers of edges of the triangles. These centers are calculated as the average of coordinates of two vertices forming the edge.

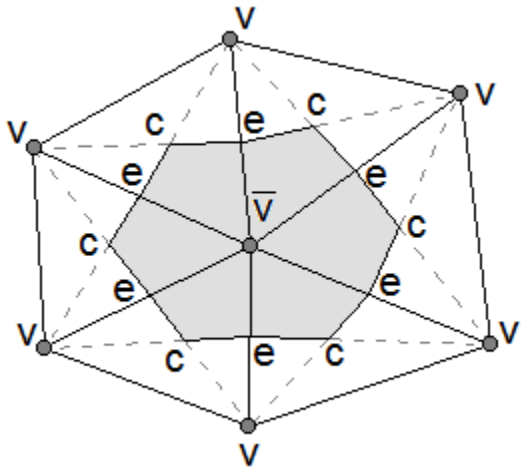

Figure 49. A typical finite volume on the unstructured mesh

Centers of the surrounding triangles are connected to the centers of the edges; thus, forming an enclosed volume which we call a finite element for the unstructured mesh. The vertex $\bar{\mathbf{v}}$ is the center of the finite volume that is shaded in the figure; it represents physical properties averaged over the volume of this element. The surrounding vertices $\mathbf{v}$ belong to neighbor finite volumes. The finite volumes connect to each other through common edges $\mathbf{ce}$. We consider a flux crossing edges $\mathbf{ce}$. This flux would redistribute the mass of the fluid, trying to equilibrate the nodal values of number density. When the flux crosses the boundary between finite volumes, it needs to be subtracted from one finite volume and added to another one. This process ensures mass conservation and provides the way for fluid redistribution on the domain.

We account for the velocity field provided from ANSYS by modifying the governing equations

$$\frac{\partial}{\partial t} n_e + \nabla\left(\mathbf{v} n_e - D_e \nabla n_e\right) = (\alpha - \eta) n_e \left|\mathbf{v}_e^d\right| - k_{ie}^{rec} n_e n_p$$

$$\frac{\partial}{\partial t} n_p + \nabla\left(\mathbf{v} n_p\right) = \alpha n_e \left|\mathbf{v}_e^d\right| - k_{ie}^{rec} n_e n_p \tag{81}$$

$$\mathbf{v} = \mathbf{v}_{conv} + \mu_e \mathbf{E}$$

The velocity is built based on superposition of the convective flow and the flow generated by the imposed electric field. The diffusion of species may also be presented in terms of diffusion velocity and added to the governing equations to keep uniformity of description, but computationally this approach would be disadvantageous. Thus the diffusion flux is calculated on a separate basis.

To provide more detailed explanation of the method we would like to consider one of the mesh triangles with vertices $\mathbf{v_1} = \begin{pmatrix} x_1 \\ y_1 \end{pmatrix}$, $\mathbf{v_2} = \begin{pmatrix} x_2 \\ y_2 \end{pmatrix}$, and $\mathbf{v_3} = \begin{pmatrix} x_3 \\ y_3 \end{pmatrix}$. Using the vertices we create a local basis in the triangle, choosing one of the vertices (for instance, v_1) as an origin and two vectors $\mathbf{v_1 v_2} = \begin{pmatrix} x_2 - x_1 \\ y_2 - y_1 \end{pmatrix}$ and $\mathbf{v_1 v_3} = \begin{pmatrix} x_3 - x_1 \\ y_3 - y_1 \end{pmatrix}$ as the coordinate axis. Any point $\mathbf{p} = \begin{pmatrix} x \\ y \end{pmatrix}$ can be represented through coordinates (ξ, η) in the constructed basis.

In order to determine the values of (ξ, η), we build a vector $\mathbf{v_1 p} = \begin{pmatrix} x - x_1 \\ y - y_1 \end{pmatrix}$ and represent as a linear combination of the basis vectors

$$\mathbf{v_1 p} = \xi \cdot \mathbf{v_3 v_1} + \eta \cdot \mathbf{v_2 v_1} \tag{82}$$

We take the following dot-products of equation (82)

$$\begin{aligned}\mathbf{v_1p}\bullet\mathbf{v_3v_1} &= \xi\cdot\mathbf{v_3v_1}\bullet\mathbf{v_3v_1}+\eta\cdot\mathbf{v_2v_1}\bullet\mathbf{v_3v_1}\\ \mathbf{v_1p}\bullet\mathbf{v}_2\mathbf{v_1} &= \xi\cdot\mathbf{v_3v_1}\bullet\mathbf{v}_2\mathbf{v_1}+\eta\cdot\mathbf{v_2v_1}\bullet\mathbf{v}_2\mathbf{v_1}\end{aligned} \tag{83}$$

This system is solved for (ξ,η) with the following result

$$\begin{aligned}\xi &= X_\xi\cdot x+Y_\xi\cdot y+C_\xi\\ \eta &= X_\eta\cdot x+Y_\eta\cdot y+C_\eta\end{aligned} \tag{84}$$

$$\begin{aligned}D &= (x_2-x_3)y_1+(x_3-x_1)y_2+(x_1-x_2)y_3\\ X_\xi &= (y_2-y_1)/D \qquad X_\eta = (y_1-y_3)/D\\ Y_\xi &= (x_1-x_2)/D \qquad Y_\eta = (x_3-x_1)/D\\ C_\xi &= (x_2y_1-x_1y_2)/D \quad C_\eta = (x_1y_3-x_3y_1)/D\end{aligned}$$

A function $f(x,y)$, defined in the triangle, with known values f_1, f_2, and f_3 at the vertices is linearly interpolated within the triangle using the following interpolation scheme

$$f = f_1+(f_3-f_1)\xi+(f_2-f_1)\eta \tag{85}$$

This function can be represented in terms of coordinates (x,y), using relation (67)

$$f = f_1+(f_3-f_1)\left[X_\xi\cdot x+Y_\xi\cdot y+C\right]+(f_2-f_1)\left[X_\eta\cdot x+Y_\eta\cdot y+C_\eta\right] = F_x x+F_y y+F_c \tag{86}$$

$$\begin{aligned}F_x &= (f_3-f_1)X_\xi+(f_2-f_1)X_\eta\\ F_y &= (f_3-f_1)Y_\xi+(f_2-f_1)Y_\eta\\ F_c &= f_1+(f_3-f_1)C_\xi+(f_2-f_1)C_\eta\end{aligned}$$

Thus, number density n, velocity $\mathbf{v}=\begin{pmatrix}u\\ v\end{pmatrix}$, and diffusion coefficient D of the species may be interpolated in the considered triangle

$$\begin{aligned}n(x,y) &= N_x x+N_y y+N_c\\ u(x,y) &= U_x x+U_y y+U_c\\ v(x,y) &= V_x x+V_y y+V_c\\ D(x,y) &= D_x x+D_y y+D_c\end{aligned} \tag{87}$$

One of important properties of the linear interpolation in the triangle is that any interpolated function has a constant gradient within the triangle

$$f = F_x x + F_y y + F_c$$
$$\nabla f = \begin{pmatrix} \partial f/\partial x \\ \partial f/\partial y \end{pmatrix} = \begin{pmatrix} F_x \\ F_y \end{pmatrix} = const \tag{88}$$

This property would be helpful in further derivations when we interpolate fluxes

Fluxes in the Mesh

A flux at any location (x, y) in the triangle is determined by the following relation

$$\mathbf{Q}(x, y) = n(x, y) \cdot \mathbf{v}(x, y) - D(x, y) \cdot \nabla n \tag{89}$$

The first term in (8) accounts for the flux due to drift and convection, the second term accounts for diffusive transport. Since all the functions used in (89) are interpolated (87) within the triangle, we substitute their interpolated representations into (89) and use the fact that the gradient is constant within the triangle to resolve the negative term in (89)

$$\mathbf{Q} = \begin{pmatrix} (N_x x + N_y y + N_c)(U_x x + U_y y + U_c) - (D_x x + D_y y + D_c) N_x \\ (N_x x + N_y y + N_c)(V_x x + V_y y + V_c) - (D_x x + D_y y + D_c) N_y \end{pmatrix} \tag{90}$$

Expression (90) is rearranged with respect to (x, y)

$$\mathbf{Q}(x, y) = \mathbf{a_1} y^2 + \mathbf{a_2} y + \mathbf{a_3} xy + \mathbf{a_4} x + \mathbf{a_5} x^2 + \mathbf{a_6} \tag{91}$$

$$\mathbf{a_1} = \begin{pmatrix} N_y U_y \\ N_y V_y \end{pmatrix} \qquad \mathbf{a_4} = \begin{pmatrix} N_x U_c + N_c U_x - D_x N_x \\ N_x V_c + N_c V_x - D_x N_y \end{pmatrix}$$
$$\mathbf{a_2} = \begin{pmatrix} N_y U_c + N_c U_y - D_y N_x \\ N_y V_c + N_c V_y - D_y N_y \end{pmatrix} \quad \mathbf{a_5} = \begin{pmatrix} N_x U_x \\ N_x V_x \end{pmatrix}$$
$$\mathbf{a_3} = \begin{pmatrix} N_y U_x + N_x U_y \\ N_y V_x + N_x V_y \end{pmatrix} \qquad \mathbf{a_6} = \begin{pmatrix} N_c U_c - D_c N_x \\ N_c V_c - D_c N_y \end{pmatrix}$$

Relation (91) represents a flux at a point inside the triangle. In order to build a numerical scheme, we need to estimate total flux over a boundary of a finite volume. Such flux would be an integral value of fluxes taken at all the points along the boundary.

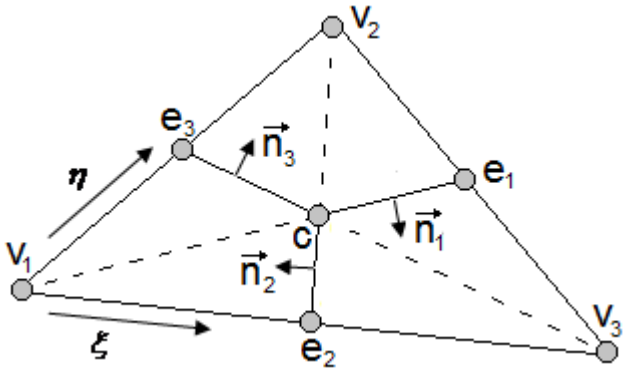

Figure 50. Triangle with locally indexed vertices, centers of the edges, and normal vectors

We assign an index $k = 1...N$ to each triangle connected to the vertex of interest. The centers of triangles receive the same index and become c_k. The centers of edges belong to two triangles (to one triangle - only in the case when the edge belongs to a boundary of the domain); hence, they cannot be indexed in such a simple manner. Inside a triangle we introduce a local indexing of vertices. The indices of centers of edges e_i and normal vectors $\mathbf{n_i}$ are connected to vertices, *opposite* to that edge. The normal vectors are directed in the direction of counting of the vertices (Figure 50).

The continuity equation for plasma can be written in terms of fluxes with the right-hand side written in a general form

$$\frac{\partial n}{\partial t} + \nabla \bullet \mathbf{Q} = I_{gen/rec} \tag{92}$$

Here Q is the summary of all the fluxes (incoming and outcoming) in the finite volume. Applying the concept of finite volume approach, we integrate equation (92) over the finite volume that has an area A.

$$\int_A \frac{\partial n}{\partial t} dA + \int_A \nabla \bullet \mathbf{Q} dA = \int_A I_{gen/rec} dA \tag{93}$$

We assume that values of number density, and generation/recombination term at the vertex $\bar{v}$ are average values over the whole finite volume associated with the vertex. Thus, they can be taken out of the integral. We also assume that integration is carried over the finite volume which consists of combination of smaller volumes contributed by each particular triangle. This assumption allows us to split the integral over the finite volume into a sum of integrals over each particular piece of a triangle.

$$\left.\frac{\partial n}{\partial t}\right|_{\bar{v}} A + \sum_{k=1}^{N} \int_{A_k} \nabla \bullet \mathbf{Q} dA = I_{gen/rec}\big|_{\bar{v}} A, \quad A = \sum_{k=1}^{N} A_k \tag{94}$$

Here A_k is the area of the sub-volume of the k^{th} triangle. Area of any triangle could be calculated using Heron's formula $A = \frac{1}{2}\left|x_1(y_2 - y_3) + x_2(y_3 - y_1) + x_3(y_1 - y_2)\right|$.

According to Divergence Theorem [87] the integral term of equation (94) can be modified as follows

$$\int_{A_k} \nabla \bullet \mathbf{Q} dA = \int_{\delta A_k} \mathbf{n} \bullet \mathbf{Q} dl \tag{95}$$

Here the right-hand side is the integral taken over the boundary of the k^{th} triangle. This integral could be further split into the sum of integrals over each separate piece of the boundary. As the example, let us write the integral at the vertex v_1 for the case shown in Figure 50.

$$\int_{\delta A_k} \mathbf{n} \bullet \mathbf{Q} dl = \int_{v_1 e_3} \mathbf{n} \bullet \mathbf{Q} dl + \int_{e_3 c} \mathbf{n} \bullet \mathbf{Q} dl + \int_{c e_2} \mathbf{n} \bullet \mathbf{Q} dl + \int_{e_2 v_1} \mathbf{n} \bullet \mathbf{Q} dl \tag{96}$$

If the edges of the triangle do not belong to the boundary of the domain, the integral terms in (96) over the boundaries $v_1 e_3$ and $e_2 v_1$ would be canceled out due to double integration. In the neighboring triangles that share the same edges $v_1 e_3$ and $e_2 v_1$ the integration would be

taken in the opposite direction, hence, the opposite sign of the integral terms. Therefore, equation (96) is reformulated accounting for the canceling terms and is substituted into (94).

$$\left.\frac{\partial n}{\partial t}\right|_{\bar{v}} A + \sum_{k=1}^{N}\left(\int_{e_{k3}c_k}\mathbf{n}\bullet\mathbf{Q}dl + \int_{c_k e_{k2}}\mathbf{n}\bullet\mathbf{Q}dl\right) = I_{gen/rec}\Big|_{\bar{v}} A \tag{97}$$

This is the continuity equation integrated over the finite volume and written in terms of fluxes.

Integration Path in the Mesh's Triangles

In order to evaluate the integral term of (97) over any set of triangles, we need to find normal vectors and estimate the fluxes over the boundaries e_3c and ce_2 (please, refer to Figure 49. The calculation of normal vectors is based on the following relations.

$$\begin{aligned}&\mathbf{n}_i \bullet \mathbf{ce}_i = 0\\ &\left\|\mathbf{n_i}\right\| = 1\\ &\mathbf{n_i} \bullet \mathbf{ce}_{i \bmod 3+1} < 0\end{aligned} \tag{98}$$

The last condition in (98) provides proper direction to normal vectors. According to relations (98), the normal vectors for a triangle are calculated with the following coordinates.

$$\begin{aligned}&Cn_i = \frac{x_{ce_i}}{y_{ce_i}}\\ &\mathbf{n_i} = \begin{pmatrix}\pm\dfrac{1}{\sqrt{1+Cn_i^2}}\\ \mp\dfrac{Cn_i}{\sqrt{1+Cn_i^2}}\end{pmatrix}\end{aligned} \tag{99}$$

The vector ce_i is calculated as follows

$$\mathbf{ce_i} = \begin{pmatrix}\dfrac{x_{i \bmod 3+1} + x_{(i+1) \bmod 3+1}}{2} - \dfrac{x_i + x_{i \bmod 3+1} + x_{(i+1) \bmod 3+1}}{3}\\ \dfrac{y_{i \bmod 3+1} + y_{(i+1) \bmod 3+1}}{2} - \dfrac{y_i + y_{i \bmod 3+1} + y_{(i+1) \bmod 3+1}}{3}\end{pmatrix} = \begin{pmatrix}\dfrac{x_{i \bmod 3+1} + x_{(i+1) \bmod 3+1} - 2x_i}{6}\\ \dfrac{y_{i \bmod 3+1} + y_{(i+1) \bmod 3+1} - 2y_i}{6}\end{pmatrix} \tag{100}$$

As the general approach, we assume that integral of the flux needs to be evaluated over some linear path in the triangle. The path is determined by coordinates of the end points

$$\mathbf{pth} = \begin{pmatrix} x_e - x_b \\ y_e - y_b \end{pmatrix} \tag{101}$$

Points $\mathbf{p}_b = \begin{pmatrix} x_b \\ y_b \end{pmatrix}$ and $\mathbf{p_e} = \begin{pmatrix} x_e \\ y_e \end{pmatrix}$ determine the beginning and the end of the path,

correspondingly. The normal vectors to this path are determined as

$$Cn = \frac{x_e - x_b}{y_e - y_b}$$
$$\mathbf{n} = \begin{pmatrix} \pm \dfrac{1}{\sqrt{1+Cn^2}} \\ \mp \dfrac{Cn}{\sqrt{1+Cn^2}} \end{pmatrix} \tag{102}$$

Validation of normal vectors confirms the major properties, i.e. their orthogonality and unit length. The sign of the normal vectors is determined based on specific conditions and depend on the location of the path. The orientation of normal vectors has a special form at the inner boundaries of the triangle to simplify summation of the fluxes when contribution at each particular vertex is estimated. It also could be inner/outer normal to the triangle edge, when the edge represents the boundary of the domain.

$$\mathbf{n} \cdot \mathbf{pth} = \begin{pmatrix} \pm \dfrac{1}{\sqrt{1+\left(\dfrac{x_e - x_b}{y_e - y_b}\right)^2}} \\ \mp \dfrac{\dfrac{x_e - x_b}{y_e - y_b}}{\sqrt{1+\left(\dfrac{x_e - x_b}{y_e - y_b}\right)^2}} \end{pmatrix} \cdot \begin{pmatrix} x_e - x_b \\ y_e - y_b \end{pmatrix} = \pm \frac{x_e - x_b}{\sqrt{1+\left(\dfrac{x_e - x_b}{y_e - y_b}\right)^2}} \mp \frac{\dfrac{x_e - x_b}{y_e - y_b}(y_e - y_b)}{\sqrt{1+\left(\dfrac{x_e - x_b}{y_e - y_b}\right)^2}} = \tag{103}$$
$$= \pm \frac{x_e - x_b}{\sqrt{1+\left(\dfrac{x_e - x_b}{y_e - y_b}\right)^2}} \mp \frac{x_e - x_b}{\sqrt{1+\left(\dfrac{x_e - x_b}{y_e - y_b}\right)^2}} = \frac{1}{\sqrt{1+\left(\dfrac{x_e - x_b}{y_e - y_b}\right)^2}} \left[\pm (x_e - x_b) \mp (x_e - x_b)\right] = 0$$

$$\|\mathbf{n}\| = \left[\left(\pm \frac{1}{\sqrt{1+\left(\frac{x_e - x_b}{y_e - y_b}\right)^2}} \right)^2 + \left(\mp \frac{\frac{x_e - x_b}{y_e - y_b}}{\sqrt{1+\left(\frac{x_e - x_b}{y_e - y_b}\right)^2}} \right)^2 \right]^{1/2} = \left[\frac{1}{1+\left(\frac{x_e - x_b}{y_e - y_b}\right)^2} + \frac{\left(\frac{x_e - x_b}{y_e - y_b}\right)^2}{1+\left(\frac{x_e - x_b}{y_e - y_b}\right)^2} \right]^{1/2} = \tag{104}$$

$$= \left[\frac{1+\left(\frac{x_e - x_b}{y_e - y_b}\right)^2}{1+\left(\frac{x_e - x_b}{y_e - y_b}\right)^2} \right]^{1/2} = 1$$

In the first case, condition (100) may be applied, when vertices of the triangles are counted clockwise/counterclockwise, the normal vector would be always pointing to the opposite direction, i.e. counterclockwise/clockwise. In the second case, the normal vector may point in the direction similar to direction of the vector starting at the vertex, opposite to the considered edge, and ending at the center of the edge (dot product of the specified vector and the normal vector should be positive); this condition provides the outer normal. When the integration part is an arbitrary line inside of the triangle, other conditions may apply to determine direction of the normal, but in most cases they could be built based on the vertices of the triangle and center points of the edges and the triangle itself.

The path, in the general case, may be formulated as a function of x or y only.

$$\begin{aligned} y &= \frac{y_e - y_b}{x_e - x_b} x + \frac{y_b x_e - y_e x_b}{x_e - x_b}, \quad \frac{y_e - y_b}{x_e - x_b} \le 1 \\ x &= \frac{x_e - x_b}{y_e - y_b} y + \frac{y_e x_b - y_b x_e}{y_e - y_b}, \quad \frac{y_e - y_b}{x_e - x_b} > 1 \end{aligned} \tag{105}$$

The flux at any point in the triangle is described by equation (91). This flux must be integrated over a portion of the boundary of the finite volume to yield with the integral term of (97). The integration could be accomplished analytically providing with very good accuracy and computational efficiency, but it requires knowledge on exact path of integration.

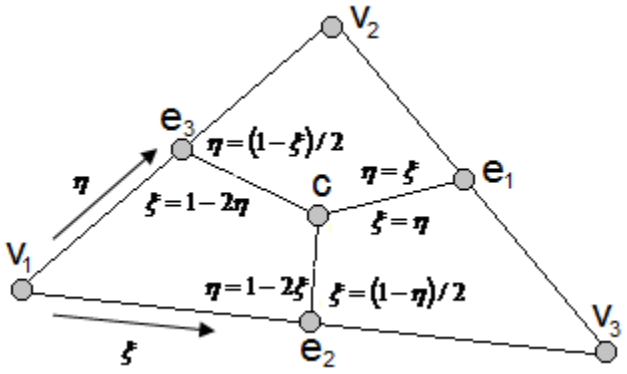

Figure 51. Integration paths in a triangle

We want to estimate the paths in the triangle along which the integration is carried on. Let us refer to the interpolation scheme one more time. In terms of interpolation coordinates (ξ,η) the important points in the triangle could be written in the following form

$$\begin{array}{ll} v_1=(0 \quad 0) & e_1=(1/2 \quad 1/2) \\ v_2=(0 \quad 1) & e_2=(1/2 \quad 0) \\ v_3=(1 \quad 0) & e_3=(0 \quad 0)1/2 \\ c=(1/3 \quad 1/3) & \xi+\eta=1, \text{ at } v_2v_3 \end{array} \tag{106}$$

Since the coordinates for all necessary points are known, we can estimate a line passing through two points and apply this method to ce_1, ce_2, and ce_3. The following lines are found

$$\begin{aligned} \text{line}\, ce_1 &: \begin{cases} \eta=\xi, \ \xi\in[0,1/2] \\ \xi=\eta, \ \eta\in[0,1/2] \end{cases} \\ \text{line}\, ce_2 &: \begin{cases} \eta=1-2\xi, \ \xi\in[0,1/2] \\ \xi=(1-\eta)/2, \ \eta\in[0,1] \end{cases} \\ \text{line}\, ce_3 &: \begin{cases} \eta=(1-\xi)/2, \ \xi\in[0,1] \\ \xi=1-2\eta, \ \eta\in[0,1/2] \end{cases} \end{aligned} \tag{107}$$

We substitute (84) into (107) and obtain integration paths in terms of (x,y).

$$\text{line } ce_1 : \begin{cases} y = -\dfrac{X_\eta - X_\xi}{Y_\eta - Y_\xi} x - \dfrac{C_\eta - C_\xi}{Y_\eta - Y_\xi} \\ x = -\dfrac{Y_\eta - Y_\xi}{X_\eta - X_\xi} y - \dfrac{C_\eta - C_\xi}{X_\eta - X_\xi} \end{cases} \qquad \text{line } ce_2 : \begin{cases} y = -\dfrac{X_\eta + 2X_\xi}{Y_\eta + 2Y_\xi} x + \dfrac{1 - C_\eta - 2C_\xi}{Y_\eta + 2Y_\xi} \\ x = -\dfrac{Y_\eta + 2Y_\xi}{X_\eta + 2X_\xi} y + \dfrac{1 - C_\eta - 2C_\xi}{X_\eta + 2X_\xi} \end{cases}$$

$$\text{line } ce_3 : \begin{cases} y = -\dfrac{2X_\eta + X_\xi}{2Y_\eta + Y_\xi} x + \dfrac{1 - 2C_\eta - C_\xi}{2Y_\eta + 2Y_\xi} \\ x = -\dfrac{2Y_\eta + Y_\xi}{2X_\eta + X_\xi} y + \dfrac{1 - 2C_\eta - C_\xi}{2X_\eta + X_\xi} \end{cases} \tag{108}$$

Relations (108) determines path of integration in the triangle. There are two functions ($y(x) = kx + b$ and $x(y) = my + d$) provided for each path, the reason is that the triangle is randomly oriented in space with path of integration represented by a line – in some cases the line is perfectly vertical or horizontal. The vertical case is extreme for $y(x)$ and the horizontal case is extreme for $x(y)$, thus one of the representations could be used, after orientation of the integration path is determined. The criterion for the path orientation is simple: when $k > 1$ we use $x(y) = my + d$, when $k <= 1$ we use $y(x) = kx + b$. The integration over the path requires not only knowledge on the function describing the path, but also evaluation of the length element along the path. The following formulation provides an easy way of such an evaluation.

$$\begin{array}{l|lll} y = kx + b & L_y = \sqrt{1 + y_x'^2} = \sqrt{1 + k^2} & dl = L_y dx \\ x = my + d & L_x = \sqrt{1 + x_y'^2} = \sqrt{1 + m^2} & dl = L_x dy \end{array} \tag{109}$$

Considering a triangle shown in Figure 51, we would like to introduce three auxiliary integrals, corresponding to the three paths of integration. We modify integral terms in (96) eliminating the normal vectors from the integrals, due to the fact that they are constants, and take only the terms that do not cancel out when integration passes through all the neighboring triangles.

$$\mathbf{I_1} = \int_c^{e_1} \mathbf{Q}(x, y)dl = \int_{x_c}^{x_{e1}} \mathbf{Q}(x, y(x))L_y dx = \int_{y_c}^{y_{e1}} \mathbf{Q}(x(y), y)L_x dy$$
$$\mathbf{I}_2 = \int_c^{e_2} \mathbf{Q}(x, y)dl = \int_{x_c}^{x_{e2}} \mathbf{Q}(x, y(x))L_y dx = \int_{y_c}^{y_{e2}} \mathbf{Q}(x(y), y)L_x dy \qquad (110)$$
$$\mathbf{I}_3 = \int_c^{e_3} \mathbf{Q}(x, y)dl = \int_{x_c}^{x_{e3}} \mathbf{Q}(x, y(x))L_y dx = \int_{y_c}^{y_{e3}} \mathbf{Q}(x(y), y)L_x dy$$

Since we know the flux value at any point (91), the length element (109), and the relation between the coordinates (108) when following the path, we can substitute all this expressions into (110) and proceed with further evaluation. The evaluation is done for two cases: $y(x) = kx + b$ and $x(y) = my + d$. After simple algebraic derivations, the resultant terms are gathered with respect to $\mathbf{a_j}$ (the coefficients from (91)). The result could be written as follows.

$$\mathbf{I_i} = \mathbf{a_1}b_{1i} + \mathbf{a_2}b_{2i} + \mathbf{a_3}b_{3i} + \mathbf{a_4}b_{4i} + \mathbf{a_5}b_{5i} + \mathbf{a_6}b_{6i}, \qquad i = 1...3 \qquad (111)$$

$y = k_i x + b_i$	$x = m_i y + d_i$
$b_{1i} = b_i^2 b_6 + 2b_i k_i b_4 + k_i^2 b_5$	$b_{1i} = L_x\left(y_{ei}^3 - y_c^3\right)/3$
$b_{2i} = b_i b_6 + k_i b_4$	$b_{2i} = L_x\left(y_{ei}^2 - y_c^2\right)/2$
$b_{3i} = b_i b_4 + k_i b_5$	$b_{3i} = d_i b_2 + m_i b_1$
$b_{4i} = L_y\left(x_{ei}^2 - x_c^2\right)/2$	$b_{4i} = d_i b_6 + m_i b_2$
$b_{5i} = L_y\left(x_{ei}^3 - x_c^3\right)/3$	$b_{5i} = d_i^2 b_6 + 2d_i m_i b_2 + m_i^2 b_1$
$b_{6i} = L_y\left(x_{ei} - x_c\right)$	$b_{6i} = L_x\left(y_{ei} - y_c\right)$

The coefficients b_{ji} depend only on geometry of the mesh. If the mesh does not change during the simulation, they remain constants. Before the simulation starts, the analysis of the mesh takes place: for each triangle of the mesh, orientation of the integration paths is estimated using the described criterion. The result is the decision on which representation of the path should be used $y(x) = kx + b$ or $x(y) = my + d$. According to the used representation, a set of b_{ji} is calculated and stored for the path i; thus, a triangle receives three such sets – one for each path. Whenever the flux along the path needs to be estimated, the coefficients $\mathbf{a_j}$ are recalculated

accounting for new values of number density, velocity, and diffusion coefficient at the vertices of the triangle. The relation (111) is then used to provide the fluxes along the paths.

One important note should be given. The integration of the fluxes proceeds from the center of the triangle $\mathbf{c}$ towards the edge $\mathbf{e_i}$. The sign of the flux $\mathbf{I_i}$ remains unchanged if the coordinate of point $\mathbf{c}$ used as parameter of integration is smaller than the corresponding coordinate of point $\mathbf{e_i}$, in the opposite case the sign of $\mathbf{I_i}$ should be reversed. This estimation may be performed at the initial stage of the simulation and the sign reversion could be introduced into b_{ji} automatically providing with the proper sign whenever (111) is applied.

The fluxes (111) are associated with the path of integration. In order to determine how much matter passes over the boundary created by the path lines, the dot product of the auxiliary fluxes and the corresponding normal vectors should be found. Each triangle contains a sub-volume of the finite volume element. The sub-volume at the vertex $\mathbf{v_i}$ is determined by two boundaries $ce_{(i+1)\bmod 3+1}$ and $ce_{i \bmod 3+1}$. We do not account for the boundaries $v_i e_{(i+1)\bmod 3+1}$ and $v_i e_{i \bmod 3+1}$, because positive/negative flux contribution here cancels out by negative/positive contribution at the neighboring triangle; unless the edge is at the boundary of the domain, which is the separate case discussed later. Thus, the contribution of the fluxes to the sub-volume at the vertex $\mathbf{v_i}$ in the triangle k is determined by fluxes over boundaries $ce_{(i+1)\bmod 3+1}$ and $ce_{i \bmod 3+1}$. Based on the direction of the normal vectors and location of the path lines, the following relation takes place.

$$\begin{aligned} \overline{Q}_{k1} &= \mathbf{I_3} \bullet \mathbf{n_3} - \mathbf{I}_2 \bullet \mathbf{n}_2 \\ \overline{Q}_{k2} &= \mathbf{I}_1 \bullet \mathbf{n}_1 - \mathbf{I}_3 \bullet \mathbf{n}_3 \\ \overline{Q}_{k3} &= \mathbf{I}_2 \bullet \mathbf{n}_2 - \mathbf{I}_1 \bullet \mathbf{n}_1 \end{aligned} \qquad (112)$$

In this relation, the variable $\overline{Q}_{ks}$ represents total contribution of the fluxes to the sub-volume at the vertex $\mathbf{v}_s$ in the triangle k with $s = 1,2,3$ being a local indexing within the triangle.

With modifications provided in (112), the continuity equation (97) is transformed into simpler version.

$$\left.\frac{\partial n}{\partial t}\right|_{\bar{v}} A + \sum_{k=1}^{N} \overline{Q}_{ks} = I_{gen/rec}\Big|_{\bar{v}} A \tag{113}$$

Equation (113) represents an explicit scheme for iterations of number density at the vertex of interest.

$$n_{new}\big|_{\bar{v}} = n_{old}\big|_{\bar{v}} + \Delta t\left(I_{gen/rec}\Big|_{\bar{v}} - \frac{1}{A}\sum_{k=1}^{N} \overline{Q}_{ks} \right) \tag{114}$$

Boundary Conditions

In order to properly estimate fluxes crossing the boundary of the domain, we have to consider an arbitrary flux in a general form, based on the derivations provided for the finite volumes. Let us assume an arbitrary line which provides a path for the integration.

$$\begin{aligned} y &= \frac{y_e - y_b}{x_e - x_b} x + \frac{y_b x_e - y_e x_b}{x_e - x_b}, \quad \frac{y_e - y_b}{x_e - x_b} \le 1 \\ x &= \frac{x_e - x_b}{y_e - y_b} y + \frac{y_e x_b - y_b x_e}{y_e - y_b}, \quad \frac{y_e - y_b}{x_e - x_b} > 1 \end{aligned} \tag{115}$$

$$\begin{array}{l|lll} y = kx + b & L_y = \sqrt{1 + y_x'^2} = \sqrt{1 + k^2} & dl = L_y dx \\ x = my + d & L_x = \sqrt{1 + x_y'^2} = \sqrt{1 + m^2} & dl = L_x dy \end{array}$$

The flux crossing this line at point (x, y) can be written in the following form

$$\mathbf{Q}(x, y) = \mathbf{a_1} y^2 + \mathbf{a_2} y + \mathbf{a_3} xy + \mathbf{a_4} x + \mathbf{a_5} x^2 + \mathbf{a_6} \tag{116}$$

This instantaneous flux is integrated along the considered path yielding with total flux

$$\mathbf{I}_{pth} = \int_{start}^{end} \mathbf{Q}(x, y) dl = \int_{xb}^{xe} \mathbf{Q}(x, y(x)) L_y dx = \int_{yb}^{ye} \mathbf{Q}(x(y), y) L_x dy \tag{117}$$

Substitute flux (91) into the integrals; also substitute definition of the lines

$$\mathbf{I}_{pth} = \int_{start}^{end} \left\{ \mathbf{a_1} y^2 + \mathbf{a_2} y + \mathbf{a_3} xy + \mathbf{a_4} x + \mathbf{a_5} x^2 + \mathbf{a_6} \right\} dl =$$
$$= \int_{xb}^{xe} \left\{ \mathbf{a_1} (kx+b)^2 + \mathbf{a_2} (kx+b) + \mathbf{a_3} x(kx+b) + \mathbf{a_4} x + \mathbf{a_5} x^2 + \mathbf{a_6} \right\} L_y dx \tag{118}$$
$$= \int_{yb}^{ye} \left\{ \mathbf{a_1} y^2 + \mathbf{a_2} y + \mathbf{a_3} (my+d) y + \mathbf{a_4} (my+d) + \mathbf{a_5} (my+d)^2 + \mathbf{a_6} \right\} L_x dy$$

This equation provides results for both representations of the integration path $y = y(x)$ and $x = x(y)$. We simplify this integral and gather the terms in front of coefficients $\mathbf{a_i}$

$$\int_{xb}^{xe} \left\{ \mathbf{a_1} (k^2 x^2 + 2bkx + b^2) + \mathbf{a_2} (kx+b) + \mathbf{a_3} (kx^2 + bx) + \mathbf{a_4} x + \mathbf{a_5} x^2 + \mathbf{a_6} \right\} L_y dx$$
$$\int_{yb}^{ye} \left\{ \mathbf{a_1} y^2 + \mathbf{a_2} y + \mathbf{a_3} (my^2 + dy) + \mathbf{a_4} (my+d) + \mathbf{a_5} (m^2 y^2 + 2mdy + d^2) + \mathbf{a_6} \right\} L_x dy \tag{119}$$

Since coefficients $\mathbf{a_i}$ are determined only from the nodal values and do not depend on the coordinates, they can be taken out of the integral together with the length correction which is constant for the whole integration path.

$$\mathbf{a_1} L_y \int_{xb}^{xe} (k^2 x^2 + 2bkx + b^2) dx + \mathbf{a_2} L_y \int_{xb}^{xe} (kx+b) dx +$$
$$+ \mathbf{a_3} L_y \int_{xb}^{xe} (kx^2 + bx) dx + \mathbf{a_4} L_y \int_{xb}^{xe} x dx + \mathbf{a_5} L_y \int_{xb}^{xe} x^2 dx + \mathbf{a_6} L_y \int_{xb}^{xe} dx$$
$$\mathbf{a_1} L_x \int_{yb}^{ye} y^2 dy + \mathbf{a_2} L_x \int_{yb}^{ye} y dy + \mathbf{a_3} L_x \int_{yb}^{ye} (my^2 + dy) dy + \tag{120}$$
$$+ \mathbf{a_4} L_x \int_{yb}^{ye} (my+d) dy + \mathbf{a_5} L_x \int_{yb}^{ye} (m^2 y^2 + 2mdy + d^2) dy + \mathbf{a_6} L_x \int_{yb}^{ye} dy$$

We evaluate the integrals

$$\begin{aligned}
&\mathbf{a_1}L_y\left(k^2\frac{x^3}{3}+2bk\frac{x^2}{2}+b^2x\right)_{xb}^{xe}+\mathbf{a_2}L_y\left(k\frac{x^2}{2}+bx\right)_{xb}^{xe}+\\
&+\mathbf{a_3}L_y\left(k\frac{x^3}{3}+b\frac{x^2}{2}\right)_{xb}^{xe}+\mathbf{a_4}L_y\left(\frac{x^2}{2}\right)_{xb}^{xe}+\mathbf{a_5}L_y\left(\frac{x^3}{3}\right)_{xb}^{xe}+\mathbf{a_6}L_y(x)_{xb}^{xe}\\
&\mathbf{a_1}L_x\left(\frac{y^3}{3}\right)_{yb}^{ye}+\mathbf{a_2}L_x\left(\frac{y^2}{2}\right)_{yb}^{ye}+\mathbf{a_3}L_x\left(m\frac{y^3}{3}+d\frac{y^2}{2}\right)_{yb}^{ye}+\\
&+\mathbf{a_4}L_x\left(m\frac{y^2}{2}+dy\right)_{yb}^{ye}+\mathbf{a_5}L_x\left(m^2\frac{y^3}{3}+2md\frac{y^2}{2}+d^2y\right)_{yb}^{ye}+\mathbf{a_6}L_x(y)_{yb}^{ye}
\end{aligned}\tag{121}$$

Then, estimate the general form of the coefficients to formulate the flux

$$\mathbf{I}_{pth}=\mathbf{a_1}b_1+\mathbf{a_2}b_2+\mathbf{a_3}b_3+\mathbf{a_4}b_4+\mathbf{a_5}b_5+\mathbf{a_6}b_6$$

$$\begin{aligned}
b_6&=L_y(x)_{xb}^{xe} & b_6&=L_x(y)_{yb}^{ye}\\
b_5&=L_y\left(\frac{x^3}{3}\right)_{xb}^{xe} & b_5&=L_x\left(m^2\frac{y^3}{3}+2md\frac{y^2}{2}+d^2y\right)_{yb}^{ye}\\
b_4&=L_y\left(\frac{x^2}{2}\right)_{xb}^{xe} & b_4&=L_x\left(m\frac{y^2}{2}+dy\right)_{yb}^{ye}\\
b_3&=L_y\left(k\frac{x^3}{3}+b\frac{x^2}{2}\right)_{xb}^{xe} & b_3&=L_x\left(m\frac{y^3}{3}+d\frac{y^2}{2}\right)_{yb}^{ye}\\
b_2&=L_y\left(k\frac{x^2}{2}+bx\right)_{xb}^{xe} & b_2&=L_x\left(\frac{y^2}{2}\right)_{yb}^{ye}\\
b_1&=L_y\left(k^2\frac{x^3}{3}+2bk\frac{x^2}{2}+b^2x\right)_{xb}^{xe} & b_1&=L_x\left(\frac{y^3}{3}\right)_{yb}^{ye}
\end{aligned}\tag{122}$$

Depending on the type of representation used for the integration path, there are two results obtained

$$\mathbf{I}_{pth} = \mathbf{a_1} b_1 + \mathbf{a_2} b_2 + \mathbf{a_3} b_3 + \mathbf{a_4} b_4 + \mathbf{a_5} b_5 + \mathbf{a_6} b_6$$

$$\begin{aligned}
b_1 &= k^2 b_5 + 2bk b_4 + b^2 b_6 & b_1 &= L_x \frac{1}{3}\left(y_e^3 - y_b^3\right) \\
b_2 &= k b_4 + b b_6 & & \\
b_3 &= k b_5 + b b_4 & b_2 &= L_x \frac{1}{2}\left(y_e^2 - y_b^2\right) \\
b_4 &= L_y \frac{1}{2}\left(x_e^2 - x_b^2\right) & b_3 &= m b_1 + d b_2 \\
 & & b_4 &= m b_2 + d b_6 \\
b_5 &= L_y \frac{1}{3}\left(x_e^3 - x_b^3\right) & b_5 &= m^2 b_1 + 2md b_2 + d^2 b_6 \\
b_6 &= L_y \left(x_e - x_b\right) & b_6 &= L_x \left(y_e - y_b\right)
\end{aligned} \tag{123}$$

The flux crossing the considered edge is found by projection of the total flux on the normal vector calculated for the edge

$$Q_{pth} = \mathbf{I}_{pth} \bullet \mathbf{n}_{pth} \tag{124}$$

The sign of the crossing flux depends on the direction of the normal, which could be either positive or negative, depending on the considered vertex.

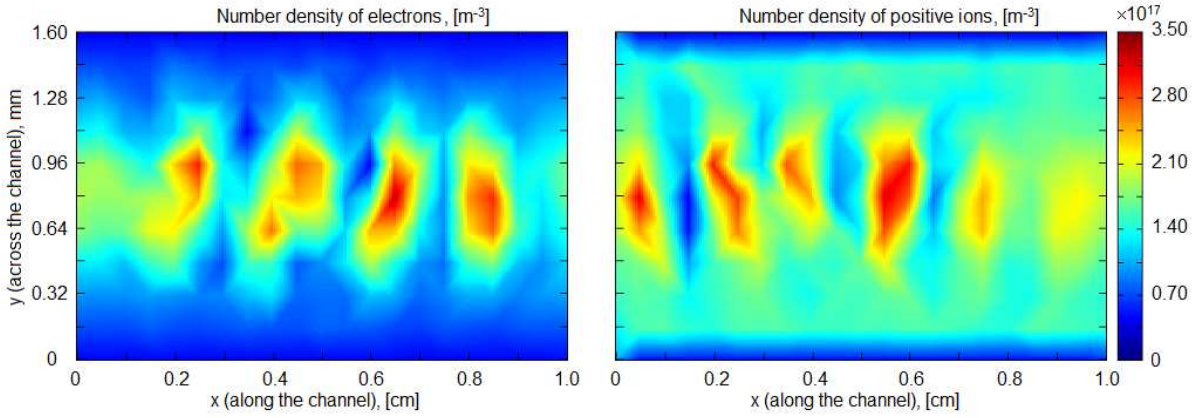

Figure 52. Convective transport of plasma species using central difference scheme only

Figure 52 shows the typical result for a calculation based on the central difference scheme for convective transport of the species. The "saw" effect is severely pronounced for both species. The peak value of the number density in both cases is $3.5 \times 10^{17} \left[1/\mathrm{m}^3\right]$ which is higher than the original maximum number density. The "saw" distribution of plasma species leads to

very high peaks and very deep valleys between the peaks. The species accumulated at the peaks result with high values of the number density.

Upwind Descritization

The method presented in the previous section resembles central difference scheme, which is known for introduction of unphysical oscillations when convective transport is considered. The oscillations lead to instabilities and poor convergence of the solution. In order to resolve the instability, the upwind descritization is applied to the problem. The value of the number density at the interface between two adjacent finite volumes is determined based on the velocity field. The velocity components are interpolated at the interface using simple geometric interpolation. A triangle is considered in order to estimate the interfacial parameters. The parameters (velocity, diffusion coefficient, and number density) are calculated at the center of the triangle and at the centers of its edges. Next, these parameters are calculated at the centers of the lines connecting triangle's center and edges' centers; the same lines represent the interfaces between adjacent finite volumes. The number density at the interface is calculated at this time for further use in central difference descritization. The interfacial velocities are multiplied by normal vectors at the interfaces to evaluate the overall impact of the flow on each of six sub-elements forming finite elements at the triangle. The sign of this multiplication determines which vertex lies upwind relative to the considered interface. The number density value and gradient of number density at the upwind vertex are used in the form of Taylor-series expansion to evaluate the number density at the interface. This newly evaluated number density is different from the one previously found in accordance with geometrical interpolation. The former includes more information about incoming flow which usually increases the interfacial number density.

The gradient of number density at the vertices of the triangle requires a special procedure for accurate calculation. The method that we use in our model is targeted to minimization of the gradient error in the least-squares sense; thus, it has a name of Least Squares Linear Reconstruction Method [88]. The idea of the method is relatively simple. We consider one computational node on the domain. In the general case, this node belongs to multiple triangles and is surrounded by multiple vertices which share same edge with the considered node. We may estimate a gradient between two nodes using ().

$$\nabla n_i = \frac{n_i - n}{\left\|\mathbf{x}_i - \mathbf{x}\right\|^2}\left(\mathbf{x}_i - \mathbf{x}\right) \tag{125}$$

This gradient is specific for the node *i*, when applied to other nodes it would result with sufficient error. If we cycle through all the surrounding nodes and calculate algebraic average of the gradient, we would find the first approximation to the gradient at the considered node. To increase the accuracy of gradient calculation, we represent the error in the form of the least squares minimization problem

$$\sum_{i=1}^{Nsur} \frac{1}{\left\|\mathbf{x}_i - \mathbf{x}\right\|^2}\left[n_i - \left(n + \nabla n\left(\mathbf{x}_i - \mathbf{x}\right)\right)\right]^2 \rightarrow \min \tag{126}$$

In this representation ∇n stands for the gradient that results in the smallest overall error when applied to any surrounding node. This gradient needs to be found from the solution of the minimization problem.

$$\frac{\partial}{\partial(\nabla n)}\left(\sum_{i=1}^{Nsur} \frac{1}{\left\|\mathbf{x}_i - \mathbf{x}\right\|^2}\left[n_i - \left(n + \nabla n\left(\mathbf{x}_i - \mathbf{x}\right)\right)\right]^2\right) = 0 \tag{127}$$

$$\left(-2\sum_{i=1}^{Nsur} \frac{1}{\left\|\mathbf{x}_i - \mathbf{x}\right\|^2}\left[n_i - \left(n + \nabla n\left(\mathbf{x}_i - \mathbf{x}\right)\right)\right]\left(\mathbf{x}_i - \mathbf{x}\right)^{\mathrm{T}}\right) = 0$$

$$\sum_{i=1}^{Nsur} \frac{1}{\left\|\mathbf{x}_i - \mathbf{x}\right\|^2} \left[(n_i - n)(\mathbf{x}_i - \mathbf{x}) - \nabla n (\mathbf{x}_i - \mathbf{x})(\mathbf{x}_i - \mathbf{x})^{\mathrm{T}} \right] = 0$$

$$\sum_{i=1}^{Nsur} \frac{1}{\left\|\mathbf{x}_i - \mathbf{x}\right\|^2} \left[(n_i - n)(\mathbf{x}_i - \mathbf{x}) \right] = \sum_{i=1}^{Nsur} \frac{1}{\left\|\mathbf{x}_i - \mathbf{x}\right\|^2} \left[\nabla n \left\|\mathbf{x}_i - \mathbf{x}\right\|^2 \right] \tag{128}$$

$$\nabla n = \frac{1}{Nsur} \sum_{i=1}^{Nsur} \frac{1}{\left\|\mathbf{x}_i - \mathbf{x}\right\|^2} \left[(n_i - n)(\mathbf{x}_i - \mathbf{x}) \right]$$

The upwind numerical scheme improves the overall stability of the simulation, at the same time it introduces significant numerical diffusion. This is why the upwind scheme is usually blended with other numerical schemes (the central difference scheme, for example). Such combination is advantageous in both, stability and diffusion domains.

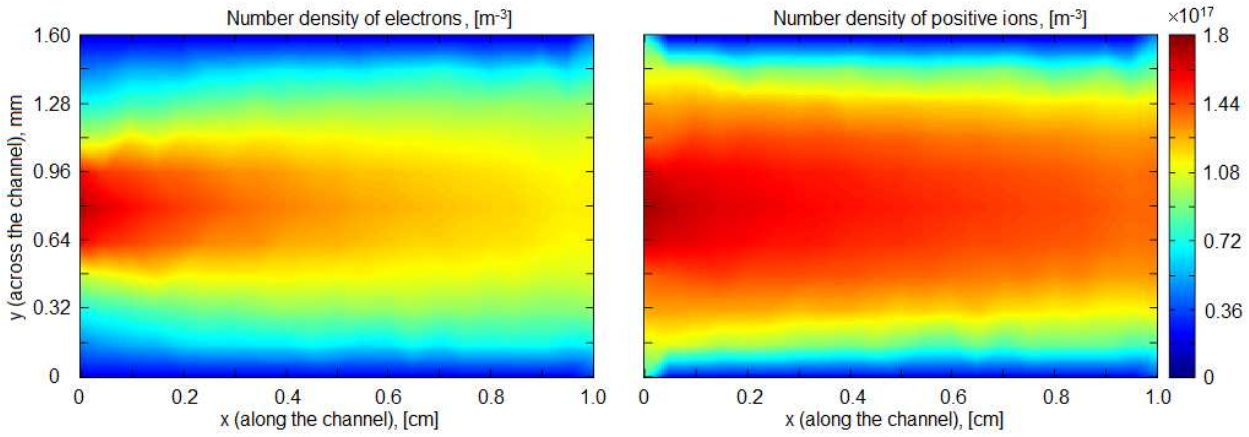

Figure 53. Convective transport of plasma species using upwind difference scheme only

Figure 53 represents the effect of upwind scheme when applied to 2D convective transport problem. In this simulation, a parabolic profile of longitudinal velocity and zero transverse velocity were applied. The species are expected to fill the whole domain using the initial distribution as a pattern. The numerical diffusion can be noticed when initial distribution of species number density (on the left side of either plot in Figure 53) is compared to that at the end of the channel (on the right side of the plots). The diffusion is so excessive, that this scheme

yields unphysical representation of the plasma and cannot be utilized alone to produce accurate results.

Blending

The two numerical techniques can be blended with arranging them into a linear combination, to determine the interfacial value of the conserved variable, in accordance with the following equation

$$n_f = \alpha n_{UPWIND} + (1-\alpha) n_{CENTRAL} \qquad 0 \le \alpha \le 1 \tag{129}$$

The blending coefficient α can be used as a constant for the whole simulation. The results of such blending are represented in Figure 54.

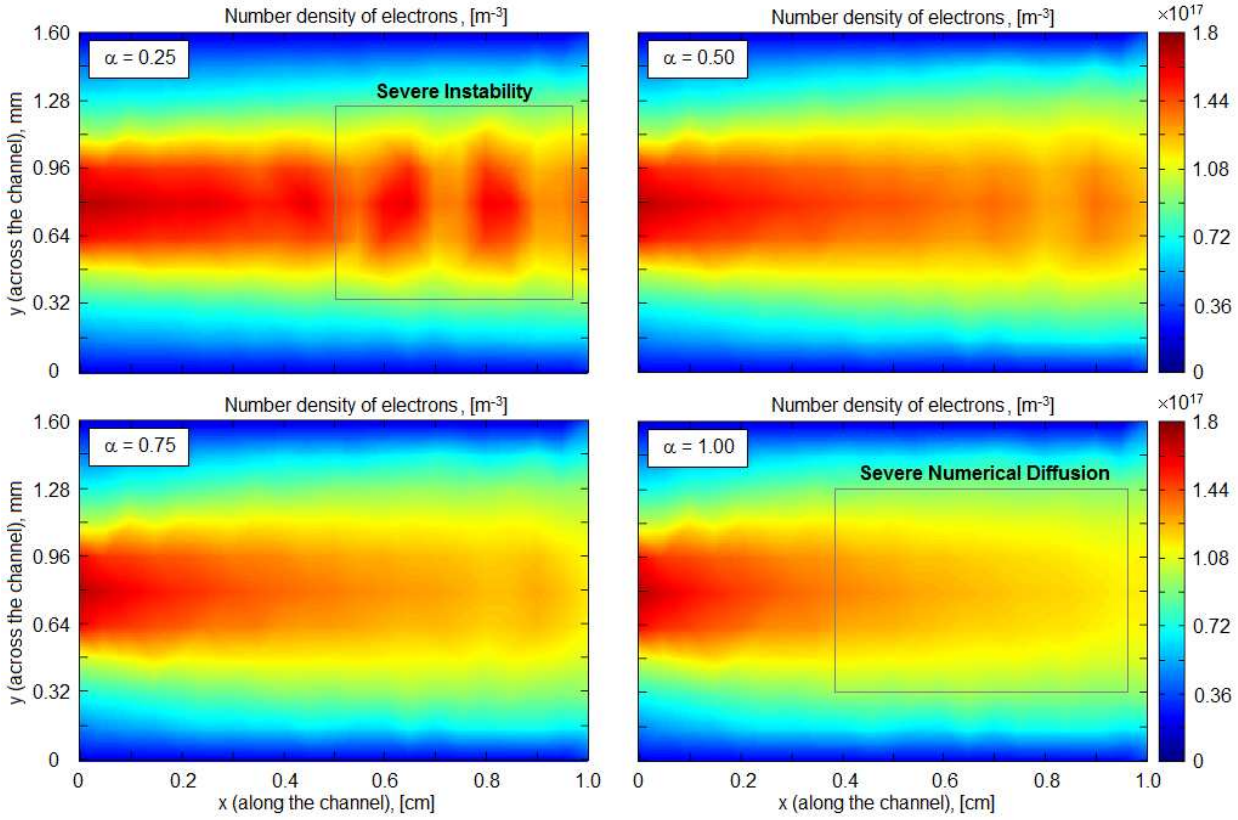

Figure 54. Blending of the numerical schemes with different blending coefficients α

Figure 54 represents static blending of Central and upwind numerical schemes. The following cases take place: $\alpha = 0$ is pure central difference scheme, $0 < \alpha < 1$ is blended numerical scheme, and $\alpha = 1$is pure upwind numerical scheme. In the shown result for $\alpha = 0.25$ central difference scheme dominates. The distribution of the species is significantly smoothened by partial contribution of upwind scheme, but smaller scale instabilities are still present, though the result is not as dramatic as the one calculated for $\alpha = 0$ (Figure 52). The case $\alpha = 0.5$may be considered the best of the presented four cases. The instability due to central difference scheme is hardly noticeable; at the same time, the numerical diffusion did not develop sufficiently to excessively smoothen the data at the outlet. In both cases $\alpha = 0.75$ and $\alpha = 1$the domination of upwind formulation determines significant smothering of the species profiles at the whole domain; thus, $\alpha > 0.5$is not a good factor when physical consistency is a concern.

As it can be concluded, the static application of the blending factor does not produce satisfactory results. This is why we develop and use dynamic blending. In dynamic blending the blending factor α is determined specifically for each particular part of the boundary of the considered finite volume. The algorithm for dynamic calculation of α is relatively simple.

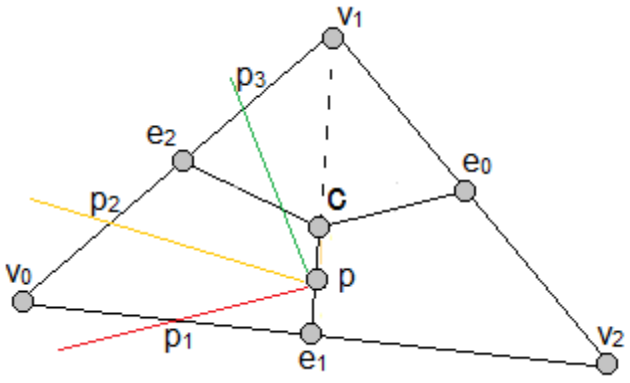

Figure 55. Calculation of dynamic blending factor

Let us consider an example shown in Figure 55. We assume that the interfacial value of number density at the point p has to be found, we also assume that the flux is directed left-to-right with the highest value at the vertex v_1. Next, we extrapolate the velocity vector at the point p following the upwind direction, until it intersects one of the triangle's edges. The green, orange, and red lines in Figure 55 represent such an extrapolation, with the points p_1, p_2, p_3 indicating the intersection with the edges. The major edges for the finite volumes at vertices v_0 and v_2 are e_2 and e_0, specifically the portions v_0e_2 and v_2e_0. When a line intersects the edge e_1 (the red line with the intersection point p_1 in Figure 55), the interfacial number density is severely affected by the vertex v_0; therefore the blending factor is $\alpha = 1$. Intersection with the edge e_2 above the center of the edge (green line with the intersection point p_3 in Figure 55) indicates that the effect of the center of the edge is dominant, thus the central difference scheme is used with the blending factor $\alpha = 0$.

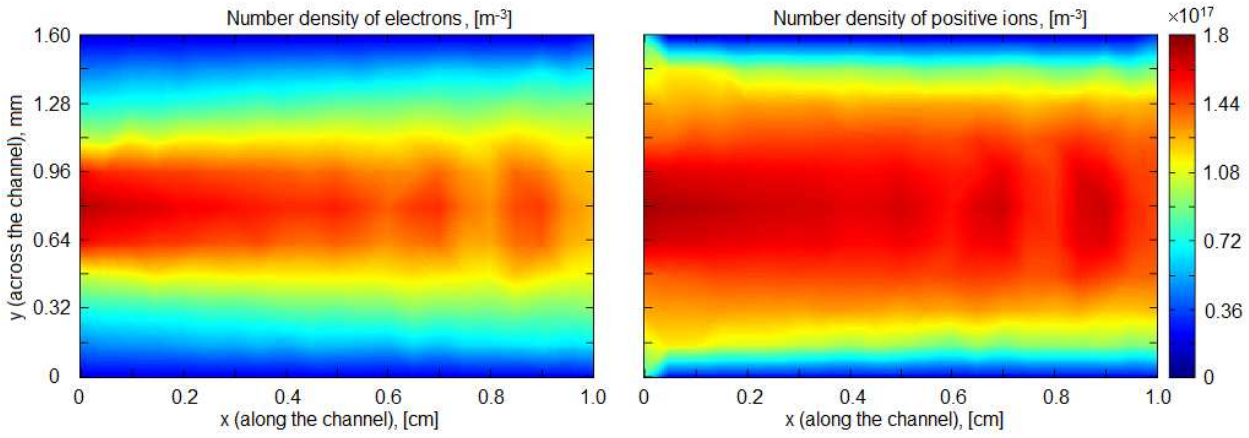

Figure 56. Dynamic blending results

The blending factor is between zero and one, when the line intersects the major edge at the proper half (the orange line with the intersection point p_2 in Figure 55). In this case, the

blending factor is determined as $\alpha = \|p_2 e_2\| / \|v_0 e_2\|$, which estimates the proper contribution of both of the scheme, based on the proximity of the extrapolated point to the center of the edge or the upwind vertex. The results calculated with dynamic blending (Figure 56) provide higher accuracy in comparison to those calculated with either of the numerical scheme alone.

The combination of central difference and upwind numerical schemes yields with relatively good number density profiles. Compared to the best static case ($\alpha = 0.5$) the numerical diffusion is slightly smaller, especially when comparing data at the outlet: orange-yellow color in the static case (Figure 54) versus red-yellow in the dynamic case (Figure 56). The instability due to the central difference scheme is still present. In order to estimate the work of the dynamic blending we calculate the mean α, as the average value of all the blending factors calculated on the domain within one particular iteration. The data presented in Figure 56 are acquired within 100000 iterations; thus, a set of 100000 alphas was recorded. The mean blending factor fits into the range $(0.3883498, 0.3888195)$, with the average of the factor being 0.388816.

The possible improvement for the dynamic blending may be achieved by using cell-centered finite volumes, as they provide more uniform distribution of the finite volume sixe and orientation.

Solution of Poisson Equation

The solution of Poisson equation requires a special numerical algorithm that is suitable for the unstructured meshes. There are different approaches used for solution of Poisson-based problems [89, 90]. Some researchers map the nodal values of the unstructured mesh to a regular mesh, solve the problem on the regular mesh using the “cross-pattern” for descritization of the

second derivative, and map the result back to the unstructured mesh. This approach does not provide any benefits and does not validate the use of unstructured mesh, as the evaluation could be performed on the regular mesh right away. Some other methods use Fast Fourier Transform [91] which can be very well parallelized [92] or Fast Multi-pole approach [90, 93]. The accuracy of the solution may be substantially improved by addition of Multigrid algorithm [94-96]. In this work we propose a novel method for descritization of Poisson problem on unstructured meshes.

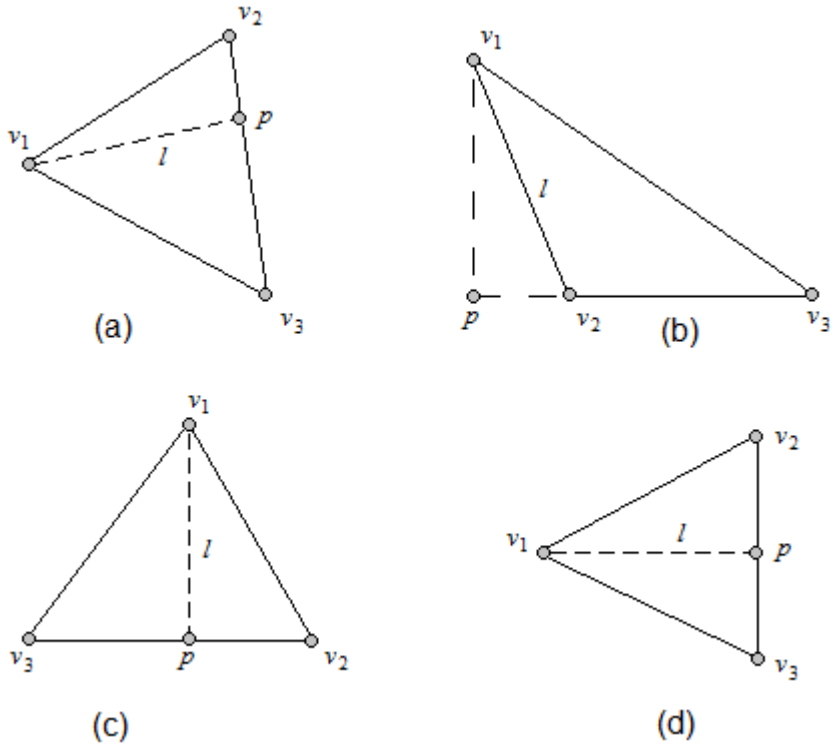

Figure 57. The shortest distance in a triangle from the vertex of interest to: (a) the opposite edge, (b) the closest vertex on the opposite edge, (c) horizontal edge, (d) vertical edge

The novel method is based on involvement of all the neighbor nodes into the calculation at the considered node. Each triangle connected to the considered node provides with a specific contribution to the function evaluated at the node. The contribution coming from a connected triangle is scaled according to the size of the triangle in terms of the angle span measured from the node of interest. The contribution of each particular triangle is determined at a specific

distance r_m from the considered node. This distance is evaluated as a fraction of the smallest distance between vertices and edges of the triangles in the whole mesh.

Assume that we are located at vertex $\mathbf{v}_1$ and we want to find the shortest distance between the current vertex and the opposite edge $\mathbf{v}_2\mathbf{v}_3$. If we are currently at another vertex, let's change the local indexing and denote the current vertex with index 1, the position of other two vertices does not matter. The shortest distance represents a line either connecting $\mathbf{v}_1$ with a point $\mathbf{p}$ on the opposite edge of the triangle (Figure 57.(a)) or connecting $\mathbf{v}_1$ with one of the other two vertices (Figure 57.(b)). There are two cases that could be handled without extra calculations – when the opposite edge is horizontal (Figure 57.(c)) the closest point is $p = (x_1 \quad y_2)$ and when the opposite edge is vertical (Figure 57.(d)) the closest point is $p = (x_2 \quad y_1)$.

In the general case (Figure 57.(a)) the closest point is calculated using two equations which are determined from the fact that vectors $\mathbf{v_1p}$ and $\mathbf{v}_2\mathbf{v}_3$ are perpendicular and the point $\mathbf{p}$ belongs to the edge $\mathbf{v}_2\mathbf{v}_3$.

The solution (130) represents the case when the edge $\mathbf{v}_2\mathbf{v}_3$ has a shallow slope. When the slope is steep, it is reasonable to handle the edge equation as $x = my + d$, the solution transforms accordingly

$$\begin{cases} (x_p - x_1)(x_3 - x_2) + (y_p - y_1)(y_3 - y_2) = 0 \\ y_p = \dfrac{y_3 - y_2}{x_3 - x_2} x_p + \dfrac{y_2 x_3 - y_3 x_2}{x_3 - x_2} \end{cases}$$

$$\begin{cases} x_p = \dfrac{1}{1 + k^2}(x_1 + y_1 k - kb) \\ y_p = kx_p + b \\ k = \dfrac{y_3 - y_2}{x_3 - x_2} \quad b = \dfrac{y_2 x_3 - y_3 x_2}{x_3 - x_2} \end{cases} \tag{130}$$

$$\begin{cases} x_p = my_p + d \\ y_p = \dfrac{1}{1+m^2}\left(y_1 + x_1 m - md\right) \\ m = 1/k \quad d = -b/k \end{cases} \tag{131}$$

Since the orientation and the shape of the triangle are arbitrary, the distance $l(v_1, p)$ should be compared to $l(v_1, v_2)$.

The general form of Poisson equation for electrostatic case reads

$$\Delta\varphi = \nabla \bullet \nabla\varphi = f = -\frac{\rho_f}{\varepsilon} \tag{132}$$

Here φ is a scalar electric potential, ρ_f is free charge density, and ε is electrical permittivity of the media. The formulation especially useful for our application is written as follows.

$$\frac{\partial}{\partial x}\left(\frac{\partial\varphi}{\partial x}\right) + \frac{\partial}{\partial y}\left(\frac{\partial\varphi}{\partial y}\right) = f \tag{133}$$

Using unstructured mesh we would like to develop a numerical scheme for calculation of electric potential at the node of interest $\bar{v}$. The usual approach to equation (133) on a regular mesh is to use cross-shaped pattern for finite difference to represent the second derivative of the potential.

On unstructured mesh, the nodes do not automatically fit into the cross pattern. A common way to handle this issue is to interpolate values of electric potential from neighboring nodes such as they lay exactly in the cross-pattern [94]. This method works well at the inner parts of the computational domain, but, approaching the boundary, the interpolated values may appear outside of the domain. This is especially true when the boundary is intensively curved. We utilize the idea of the cross-pattern and apply it to the unstructured mesh at the same time developing it even further. The cross-pattern assumes that the lines of the pattern coincide with the coordinate axis of the Euclidian coordinate system. The regular differentiation is

accomplished along the pattern lines in the direction corresponding to the positive direction of the coordinate axis.

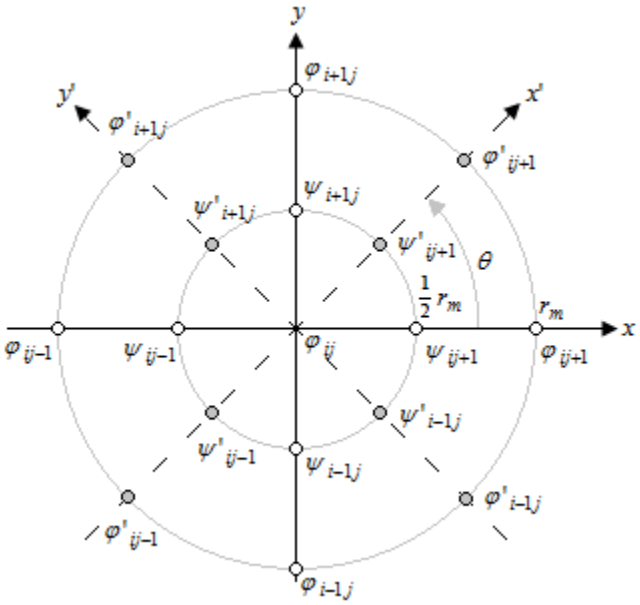

Figure 58. Cross-pattern for finite difference representing Laplace operator in Poisson equation

Let us assume that there are some arbitrary nodes which lay on a circle of radius r_m around the node of interest (Figure 58). The value of electric potential at the node of interest is φ_{ij}, the values of the arbitrary nodes, forming the cross-pattern are $\varphi_{i-1j}, \varphi_{i+1j}, \varphi_{ij-1}, \varphi_{ij+1}$. The cross pattern can be written as follows

$$\frac{\partial}{\partial x}\left(\frac{\partial \varphi}{\partial x}\right)+\frac{\partial}{\partial y}\left(\frac{\partial \varphi}{\partial y}\right)=\frac{1}{r_m}\left(\frac{\varphi_{ij+1}-\varphi_{ij}}{r_m}-\frac{\varphi_{ij}-\varphi_{ij-1}}{r_m}\right)+\frac{1}{r_m}\left(\frac{\varphi_{i+1j}-\varphi_{ij}}{r_m}-\frac{\varphi_{ij}-\varphi_{i-1j}}{r_m}\right) \tag{134}$$

Now let us imagine that the coordinate system is rotated at a small angle, becoming a coordinate system (x', y') (Figure 58). Since the cross-pattern lines are aligned with the coordinate axis, the pattern in new coordinates appears to be rotated at angle θ in comparison to the original orientation. Nevertheless, the same equation (134) is valid in new coordinates. The derivatives of electric potential with respect to x and y are taken along the new coordinate axis. We would like

to generalize this case: for any angle θ, the cross-pattern (134) properly defines Laplace operator with differentiation carried out along the new/rotated coordinate axis.

For the observer at the original coordinate system it would appear that differentiation is taken in "radial" direction with 90^o difference in angular direction for $\partial/\partial x$ and $\partial/\partial y$. Moreover, for $\theta = 90^\circ$ we have the following relations $\partial^2/\partial x'^2 \to \partial^2/\partial y^2$ and $\partial^2/\partial y'^2 \to -\partial^2/\partial x^2$. The second derivative does not change sign $\left(\partial^2 f/\partial x'^2 = \Delta f/\Delta x'^2 = \Delta f/(-\Delta x)^2 = \partial^2 f/\partial x^2\right)$when direction of differentiation is reversed. We introduce new function $\psi(x, y)$ which represents the first derivative of $\varphi(x, y)$ when taken to the right or to the top of the node of interest, and the first derivative with the negative sign when taken to the left or to the bottom of the node of interest. Numerically, this function is calculated like

$$\begin{aligned} \psi_{i-1j} &= \frac{\varphi_{i-1j} - \varphi_{ij}}{r_m} \quad \psi_{i+1j} = \frac{\varphi_{i+1j} - \varphi_{ij}}{r_m} \\ \psi_{ij-1} &= \frac{\varphi_{ij-1} - \varphi_{ij}}{r_m} \quad \psi_{ij+1} = \frac{\varphi_{ij+1} - \varphi_{ij}}{r_m} \end{aligned} \tag{135}$$

We substitute (135) into (134) and obtain

$$\frac{\partial}{\partial x}\left(\frac{\partial \varphi}{\partial x}\right) + \frac{\partial}{\partial y}\left(\frac{\partial \varphi}{\partial y}\right) = \frac{1}{r_m}\left(\psi_{ij+1} + \psi_{ij-1}\right) + \frac{1}{r_m}\left(\psi_{i+1j} + \psi_{i-1j}\right) = \frac{1}{r_m}\left(\psi_{i+1j} + \psi_{i-1j} + \psi_{ij+1} + \psi_{ij-1}\right) \tag{136}$$

Since the sign of the function $\psi(x, y)$ depends on its location relative to the node of interest, the mismatch in sign at $\theta = 90^\circ$ disappears when regular derivatives are substitute with this function. We can rewrite the Poisson equation in terms of the finite difference, using (136)

$$\frac{1}{r_m}\left(\psi_{i+1j} + \psi_{i-1j} + \psi_{ij+1} + \psi_{ij-1}\right) = f_{ij} \tag{137}$$

Since the cross-pattern (137) is valid for any angle θ, we want to summarize all such equations taken at angles $\theta \in [0, \pi/2]$. The summation is represented by an integral with respect to

the angle θ and evaluated over the interval $[0, \pi/2]$. There is no reason to take larger interval, as for $\theta > \pi/2$ the function $\psi(x, y)$ repeats.

$$\int_0^{\pi/2} \psi_{i+1j} d\theta + \int_0^{\pi/2} \psi_{i-1j} d\theta + \int_0^{\pi/2} \psi_{ij+1} d\theta + \int_0^{\pi/2} \psi_{ij-1} d\theta = r_m f_{ij} \int_0^{\pi/2} d\theta \tag{138}$$

The function $\psi(x, y)$ is determined on the circle with radius $r_m/2$ and changes with angle θ. Therefore, instead of $\psi(x, y)$ we can write $\psi(\theta)$.

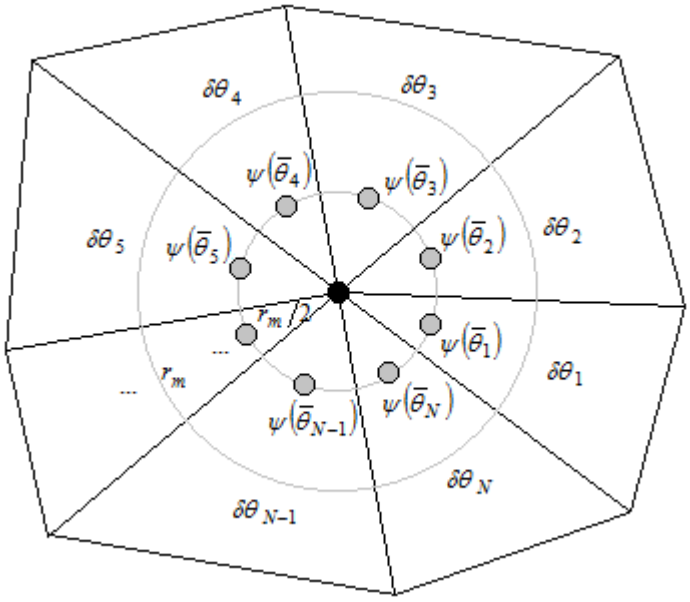

Figure 59. Finite difference for Poisson equation on unstructured mesh

Let us substitute this correction into (138) we keep the integral terms at the same places on the left- hand side so that the substitution is easy to track back to the original form.

$$\int_{\pi/2}^{\pi} \psi(\theta) d\theta + \int_{3\pi/2}^{2\pi} \psi(\theta) d\theta + \int_0^{\pi/2} \psi(\theta) d\theta + \int_{\pi}^{3\pi/2} \psi(\theta) d\theta = \frac{1}{2} \pi r_m f_{ij}$$

$$\int_0^{2\pi} \psi(\theta) d\theta = \frac{1}{2} \pi r_m f_{ij} \tag{139}$$

Next, we assume that $\psi(\theta)$ may be constant in some interval $[\theta_{k-1}, \theta_k]$. If we divide the circle where $\psi(\theta)$ is calculated into a set of such intervals, the integral (139) splits into a series of integrals over the intervals of constant values. Using the fact that $\psi(\theta)$ is constant in each interval, it can be taken out of the integral (140).

Figure 59 shows elements of an unstructured mesh connected to a vertex (the black point) where electric potential should be evaluated. The constant values of $\psi(\bar{\theta}_k)$ are taken at the circle of radius $r_m/2$, the angular element $\delta\theta_k$ corresponds to the angle of the k^{th} triangle at the vertex of interest.

$$\int_0^{2\pi} \psi(\theta) d\theta = \sum_{k=1}^{N} \int_{\theta_{k-1}}^{\theta_k} \psi(\bar{\theta}_k) d\theta = \sum_{k=1}^{N} \left\{ \psi(\bar{\theta}_k) \int_{\theta_{k-1}}^{\theta_k} d\theta \right\} = \sum_{k=1}^{N} \left\{ \psi(\bar{\theta}_k)(\theta_k - \theta_{k-1}) \right\} = \frac{1}{2} \pi r_m f_{ij}$$

$$\sum_{k=1}^{N} \left\{ \psi(\bar{\theta}_k) \delta\theta_k \right\} = \frac{1}{2} \pi r_m f_{ij} \qquad (140)$$

It is good to place $\psi(\bar{\theta}_k)$ at specific coordinates (ξ, η) in the triangle, for example on the median connecting the vertex of interest v_i and the point e_i at the middle of the opposite edge of the triangle (please refer to interpolation in triangle in the previous section). This way the coordinates are fixed and location of $\psi(\bar{\theta}_k)$ is approximately at the center of the angular segment $\delta\theta_k$. The radius r_m could be estimated as the half of the mean distance between the vertex of interest and all the surrounding vertices.

The advantage of such a modified numerical scheme for Poisson equation is that all vertices surrounding the vertex of interest contribute to the calculation process. When regular cross-pattern is used, there are only four points interpolated to fit the pattern. For the example presented in Figure 59, these points would fit into triangles 2, 3, 5, and *N*-1. The other surrounding triangles *do not* contribute into the calculation process. From one perspective this

saves calculation time, because only four interpolations are required. From another perspective, the information of electrical potential distribution is not complete at the vertex of interest, as some surrounding vertices did not contribute with their values.

In the Poisson Scheme we assumed that the integral (140) could be integrated over intervals of constant $\varphi(\bar{\theta}_k)$. In the simplest case, the constant value has to be taken at the median connecting the vertex of interest with the opposite edge. The position of the sample point at the median is determined by radius r_m. The coordinates of the sample point are

$$x_k = x_1 + \frac{r_m(x_2 + x_3 - 2x_1)}{\sqrt{(x_2 + x_3 - 2x_1)^2 + (y_2 + y_3 - 2y_1)^2}} \quad y_k = y_1 + \frac{r_m(y_2 + y_3 - 2y_1)}{\sqrt{(x_2 + x_3 - 2x_1)^2 + (y_2 + y_3 - 2y_1)^2}} \tag{141}$$

For better accuracy, the function $\varphi(\theta)$ has to be integrated from θ_{k-1} to θ_k along the circle with the center at $\mathbf{v_1}$ and radius r_m. The integration result needs to be averaged over $(\theta_k - \theta_{k-1})$. Such value would represent the true mean constant value in the triangle.

We assume that electric potential $(\varphi_1, \varphi_2, \varphi_3)$ is known at the corners of the triangle. The value at the sample point could be interpolated using (86).

$$\begin{aligned}
&\varphi(x_k, y_k) = \Phi_x x_k + \Phi_y y_k + \Phi_c \\
&\Phi_x = (\varphi_3 - \varphi_1)X_\xi + (\varphi_2 - \varphi_1)X_\eta \\
&\Phi_y = (\varphi_3 - \varphi_1)Y_\xi + (\varphi_2 - \varphi_1)Y_\eta \\
&\Phi_c = \varphi_1 + (\varphi_3 - \varphi_1)C_\xi + (\varphi_2 - \varphi_1)C_\eta
\end{aligned} \tag{142}$$

The coefficients of the Poisson Scheme are assembled using coefficients in front of $(\varphi_1, \varphi_2, \varphi_3)$. We expand (142) and derive the coefficients:

$$\begin{aligned}
&\varphi(x_k, y_k) = \Phi_1\varphi_1 + \Phi_2\varphi_2 + \Phi_3\varphi_3 \\
&\Phi_1 = 1 - \Phi_2 - \Phi_3 \\
&\Phi_2 = \eta_k = X_\eta x_k + Y_\eta y_k + C_\eta \\
&\Phi_3 = \xi_k = X_\xi x_k + Y_\xi y_k + C_\xi
\end{aligned} \tag{143}$$

The same result could be obtained using (84) and (85)

$$f = (1-\xi-\eta) f_1 + (\eta) f_2 + (\xi) f_3$$

We proceed further and calculate coefficients of function $\psi(\theta)$. Accounting for (135) we can write

$$\psi(\theta) = \frac{1}{r_m}\left(\varphi(\theta) - \varphi_{ij}\right) \tag{144}$$

Substitute (143) into (144)

$$\begin{aligned} &\psi(\theta) = \frac{1}{r_m}\left(\Phi_1\varphi_1 + \Phi_2\varphi_2 + \Phi_3\varphi_3 - \varphi_{ij}\right) = \Psi_1\varphi_1 + \Psi_2\varphi_2 + \Psi_3\varphi_3 \\ &\Psi_i = \frac{1}{r_m}\left(\Phi_i - \delta_{ik}\right) \end{aligned} \tag{145}$$

Here δ_{ik} is the Kronecker delta and k is the local index of the vertex of interest in the considered triangle. We substitute (144) into (140) and obtain modified coefficients

$$\sum_{k=1}^{N} \left\{ \left(\Psi_1\varphi_{k1} + \Psi_2\varphi_{k2} + \Psi_3\varphi_{k3}\right)\delta\theta_k \right\} = \frac{1}{2}\pi r_m f_{ij} \tag{146}$$

The index k in equation (146) passes through all the triangles surrounding the vertex of interest. The index i at the coefficients Ψ_i and electric potential φ_{ki} corresponds to the exact local index in the triangle k. The coefficients Ψ_i can be used only for one vertex in the triangle. If another vertex is considered, the coefficients must be recalculated, as the median would change with consequent change in position of the sample point (x_k, y_k).

Let us assume that the vertex of interest is surrounded by N_v other vertices. We can rewrite (146) in terms of these vertices

$$\begin{aligned} &\sum_{s=1}^{Nv}\left\{\sum_{k=1}^{N} C_{ks}\right\}\varphi_s = C_{fs} f_{ij} \\ &C_{ks} = \left(\Psi_i \delta\theta_k\right)\lambda_{ks} \quad C_{fs} = \frac{1}{2}\pi r_m \end{aligned} \tag{147}$$

In equation (147) the index s passes through a number of vertices that includes the vertex of interest and the surrounding vertices directly connected to the vertex of interest, the index k passes through all the surrounding triangles, the index i is the local index of the vertex s in the triangle k, the function λ_{ks} is equal to one if the vertex s belongs to the triangle k, otherwise it is equal to zero. We further simplify (146)

$$\overline{\varphi} = C_f f_{ij} - \sum_{s=1}^{Nv-1} C_s \varphi_s \tag{148}$$

Here $C_s = \frac{1}{\overline{C}} \sum_{k=1}^{N} C_{ks}$ represents the inner summation and $C_f = C_{fs} / \overline{C}$ is a coefficient in front of the free charge. Both of these coefficients account for the coefficient $\overline{C}$ in front of the vertex of interest. It is worth to mention that all considered coefficients depend on geometry only. If the mesh does not change, they stay constant throughout the simulation. Thus the coefficients could be calculated at the initial stage and stored in a list which order corresponds to the order of the vertices surrounding the vertex of interest. When solution of Poisson equation is required the coefficients are multiplied by corresponding electric potential and, according to (148), immediately provide the proper value at the considered vertex.

The implicit scheme can be easily derived from (148) resulting with a constant matrix (unless the mesh changes). This matrix could be processed before the simulation, in order to find its inverse form. At the simulation, only the right hand side vector consisting of the free charges needs to be formed. A simple multiplication by the inverse matrix immediately yields with the correct distribution of electric potential. Even simpler way to find the mean value of $\varphi(\theta)$ is to take the mean electric potential at the center of the triangle $\frac{1}{3}(\varphi_1 + \varphi_2 + \varphi_3)$ and to use it for any vertex assuming that this value is actually on the circle with radius r_m.

In order to estimate the effect of the fringing electric field and the species charge on a solution of the Poisson equation, we calculate and plot (Figure 60) the left-hand side and the right-hand side of equation (133). According to our analysis, the solution is not affected by species charges (the right plot in Figure 60); it mainly depends on the fringing electric field (the left plot in Figure 60) from the electrodes, as it is indicated by seven orders of magnitude difference between the left and the right hand sides of the Poisson equation.

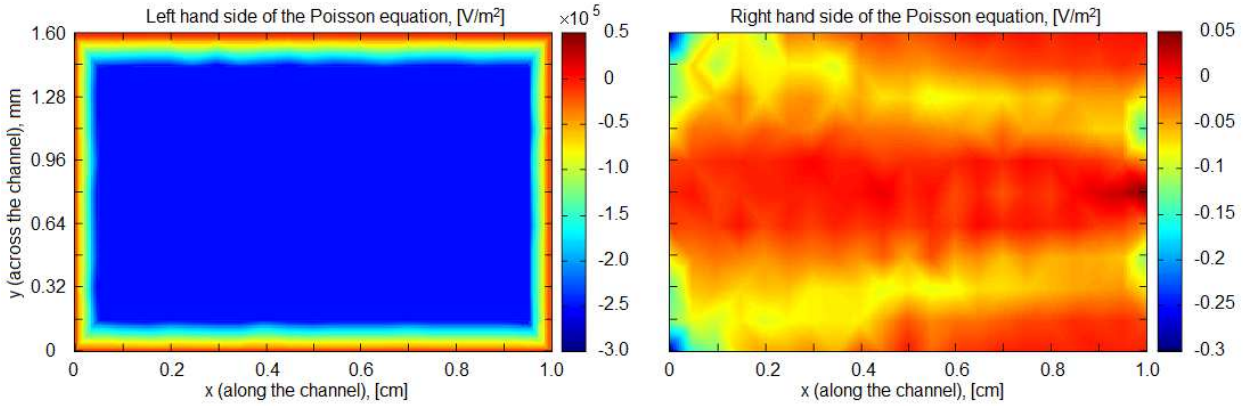

Figure 60. The left-hand side (left) and the right-hand (right) side of Poisson equation

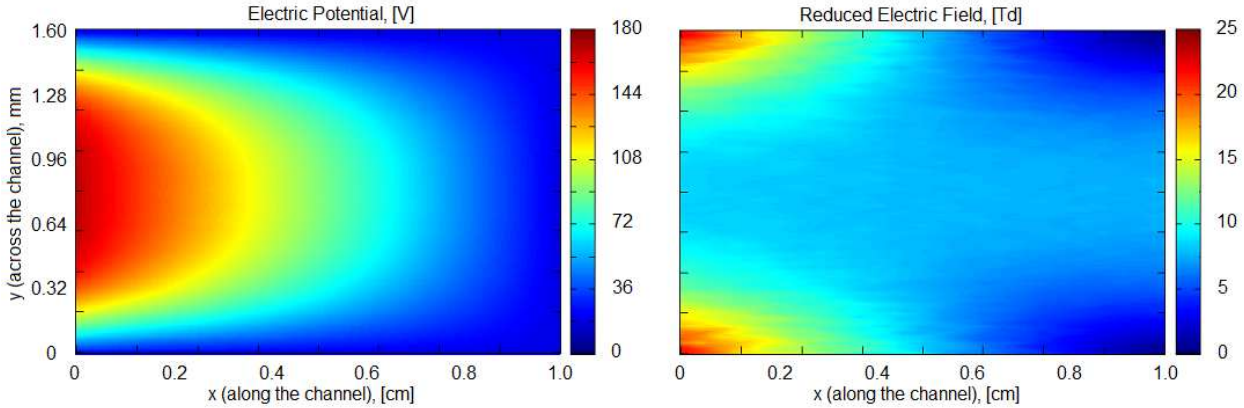

Figure 61. Electric potential (left) and reduced electric field (right)

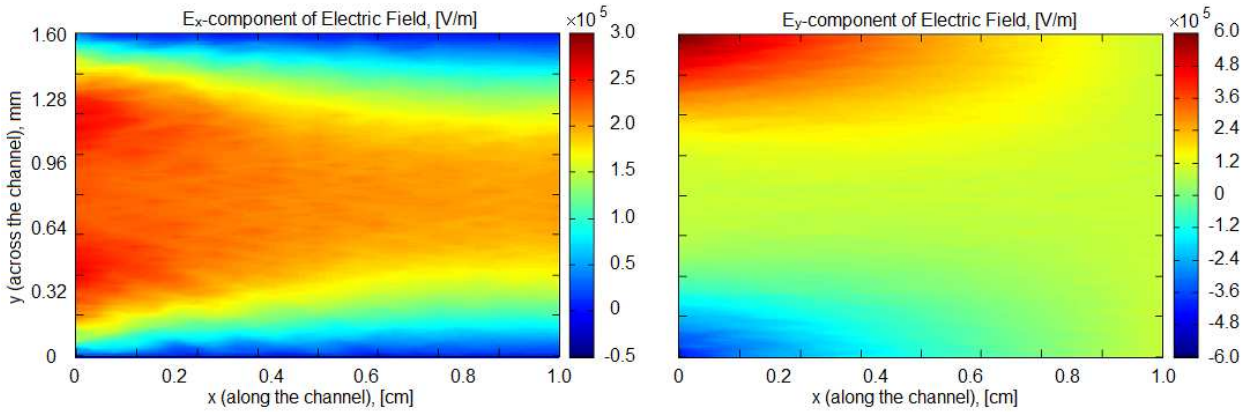

Figure 62. Electric field components: E_x (left) and E_y (right)

The left plot in Figure 61 represents the electric potential calculated with the use of the presented numerical scheme. The electric potential at the inlet (Figure 63) is derived from the 1D model of plasma generation. Due to significant contribution of the fringing electric field, the highest electric potential for 2D problem is found in the vicinity of electrodes. The further from the inlet, the lower becomes the electric potential. The electric potential almost does not change during the simulation due to negligible contribution of species charge to electric potential distribution. The x- and y-components of electric field (Figure 62) are determined from the gradient of electric potential.

The steep electric gradient along the inlet, especially in the vicinity of the walls (Figure 63), is a derivative of the oscillating electric field between the electrodes. The *y*-component of the electric field is constant, due to the strict relation between 2D and 1D plasma models. At the same time, the longitudinal component of the field is not bound to 1D problem. In 1D case, this component was zero, because everywhere between the electrodes, the electric field fluctuated uniformly. At the channel with free walls, the electric field rapidly changes in *x*-direction. This is why the relaxation of electric potential along the channel can be observed even at the inlet.

Comparing orders of magnitude, the transverse component of electric field is 2x larger than the longitudinal one.

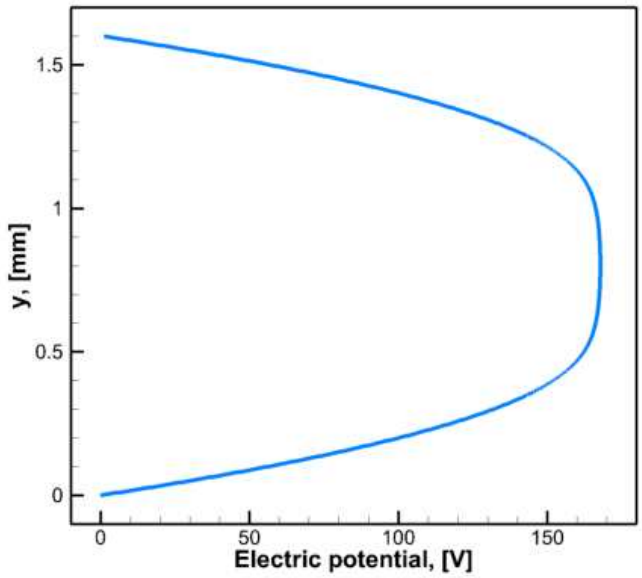

Figure 63. Electric potential at the Inlet

The right plot in Figure 61 shows the reduced electric field which is calculated as the length of the electric field vector divided by the number density of the neutral gas. The reduced electric field is not constant at the inlet: while the *y*-component of the field is constant, the x-component changes accounting for electrical conditions of open channel right after the inlet. Because the reduced electric field is determined from the length of the electric field vector, its value constantly changing, following the *x*-component of the field. The high values of the reduced electric field in the left-top and left bottom corners correspond to similar behavior of E_y, leading to well pronounced species generation at these areas of the domain.

There are analytical [93, 97] and numerical [98-100] approaches exist to solve Poisson equation in order to estimate the fringing effect of the electric field at the edges of the capacitor-type arrangement of the electrodes. Our model automatically accounts for the fringing effect,

using the initial 1D distribution of the electric potential, and expanding it along the channel. Due to this fact, there is no need for additional procedures to implement the fringing electric field in the 2D model.

Results and Discussion

The results acquired from 2D simulation of plasma advection in the channel may be divided into three categories – convective results, electrical results, and the ones combining both, fluidic and electrical effects. The first category represents plasma species advancing along the channel due to purely convective forces with no electrical field engaged. For convective transport, the species may be considered as a regular gas which flows due to the imposed velocity field. Species distribution due to convective transport is shown in Figure 56. The species distribution follows velocity profile of the gas flow, resembling parabolic shape. These data do not properly represent the plasma, as there is no collective behavior of the species when electric field is taken out of the consideration. Nevertheless, the species distribution is calculated based on their profile taken from the 1D problem of plasma generation. The next step is introduction of electric field that is shown in Figure 61 and calculation of the species respond to the field. We implement the recombination of electrons and positive ions, in order to properly account for the species losses. Electrons are present at the Inlet in smaller number than positive ions, this is why they are completely consumed in the recombination process, showing no propagation in the left plot of Figure 64.

The right plot of Figure 64 represents propagation of positive ions along the channel of the plasma reactor. The recombination process consumes a majority of positive ions within a

short distance, with the peak population falling from $1.8\times10^{17}\left[1/m^3\right]$ to $0.4\times10^{17}\left[1/m^3\right]$, resulting in 4x decrease in the number density at the distance of $1\,\mathrm{cm}$.

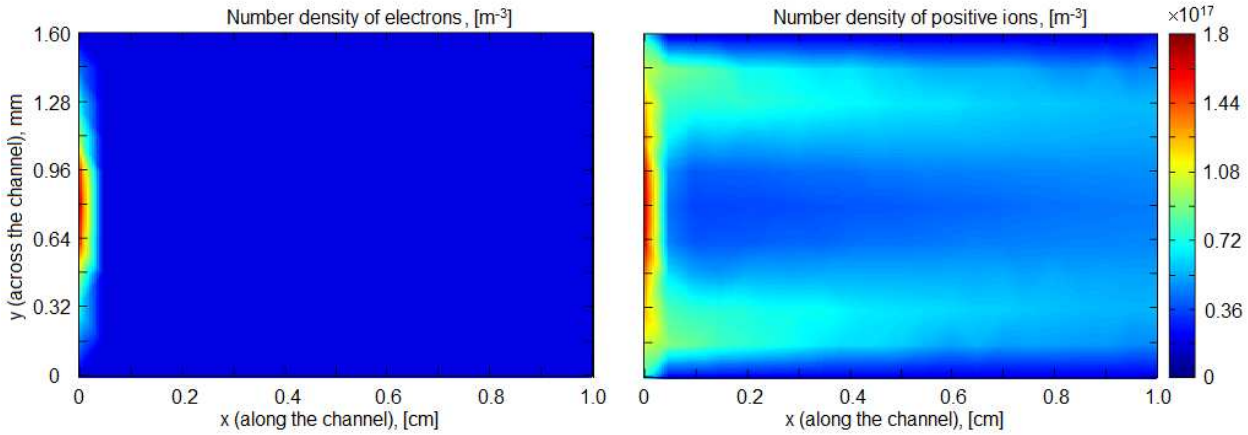

Figure 64. Convective flux of species at the steady state

The species generation and accounting for drift velocity introduces fluxes of few orders of magnitude higher than those generated by convective transport. These fluxes require extremely small time step to be resolved correctly by either presented numerical scheme. This case requires additional treatment that works with large gradients of number density.

Comparing the prediction of 1D plasma model for plasma fade, we can conclude that in 1D case the remaining number density is underestimated. For example, Figure 37 shows $1.776\times10^{15}\left[1/m^3\right]$ as the number density for remaining positive ions at the distance of $1\,\mathrm{cm}$, which is 20x smaller than the value predicted by 2D model.

Figure 65 shows typical profiles for number density of positive ions measured with $2\,\mathrm{mm}$ step, starting from the Inlet. The drastic decrease in number of ions could be immediately seen when the profile at the Inlet (0 mm) and the one at $2\,\mathrm{mm}$ are compared. The very pronounced feature of all the profiles, except the initial one, is a depression at the center which is formed due to the recombination process. Since the recombination term is directly proportional

to the number density of the species, the highest species loss occurs at the central area where the largest number of the species is present. Electrons are consumed in this process entirely, while positive ions develop a depression in their number density profile.

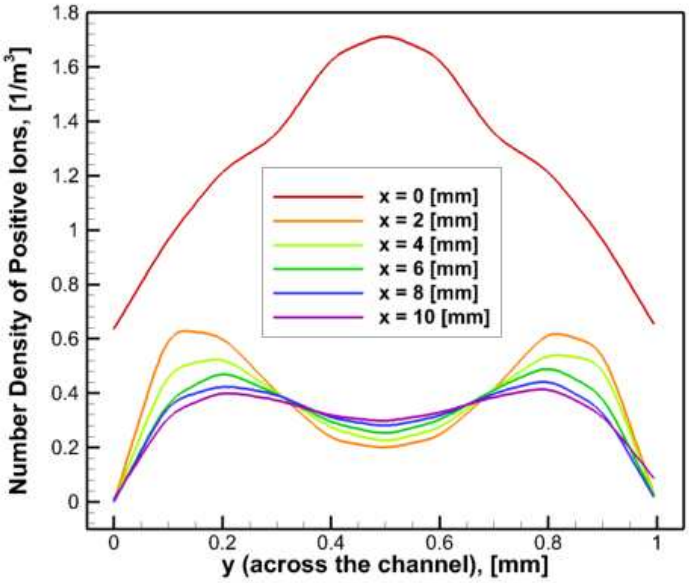

Figure 65. Typical profiles of advected plasma at different locations along the channel

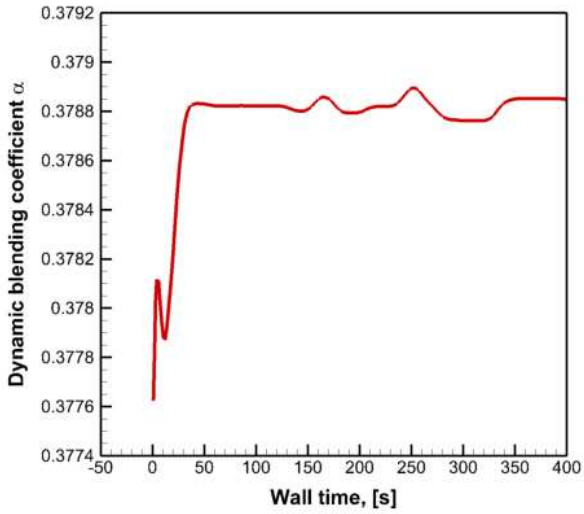

Figure 66. Average blending coefficient for dynamic blending of 2D numerical scheme

The data presented in this section is calculated using 100000 iterations on a computational domain consisting of 2500 nodes connected into 4752 triangular elements that compose the mesh. The dynamic blending favored central difference scheme spending most of the time around $\alpha = 0.3788$(Figure 66). A similar value of the blending factor was observed for random unstructured mesh and for the mesh with triangles having two sides aligned with the coordinate axes.

CONCLUSION

The model of plasma discussed in this work has been known for few decades. However, some features of this model were not clearly understood. In this work we highlighted the details that we found important or challenging while simulating plasma behavior, for example, we found how the boundary conditions have to be properly constructed for a numerical representation of 1D Poisson equation, we observed major species generation at locations different from the peaks of number density, we also developed two numerical approaches to solution of convective transport and the Poisson equation in 2D case.

For the 1D problem of plasma generation between two parallel electrodes, we discussed time-averaged profiles of number density of the species, the electric field, the generation/recombination, the temperature of species, and some other parameters evaluated in numerical simulation. These parameters provide the necessary initial conditions for the 2D model of the LAPPD system. The analysis of these parameters emphasized important features and revealed previously hidden relations among processes in plasma.

The surface plots presented in the work help with understanding of some dynamic effects, such as when and why the generation/recombination happens. Some results lead to interesting outcomes. For example, it is easy to imagine that generation of species should happen when a large cloud of electrons passes through a neutral gas. Nevertheless, the surface plots showed that the major generation happens at the point where number density of electrons is closer to the mean value, with high electric field generated due to overhead of ions at that location. The surface plots also provided visual assistance in understanding dynamics of plasma motion in the alternating electric field.

Plasma sheath and phase shift were considered as potential parameters for experimental measurements, creating a good validation point for the model of plasma generation and sustainment. Finally, some engineering outcomes were made from the model of plasma generation. Temperature of electrodes was represented as a function of applied external voltage and analyzed with considerations on the necessity of cooling equipment. The interesting example of plasma fade showed a potential range of plasma plume. The range was estimated for different voltages in order to roughly determine the favorable mode of operation for the LAPPD setup.

In the 2D model we developed two numerical methods in order to simulate plasma on unstructured meshes. One method addresses solution of continuity equation for plasma species, using the concept of finite volumes and analyzing fluxes crossing the boundaries of the finite volumes. Analytical derivations and numerical results are present in this work to demonstrate this method. The second method was developed for solution of Poisson equation on unstructured meshes. When calculating electric potential at one of the nodes, the method naturally involve all the surrounding nodes into the calculation, with each node contributing to the result according to the angular span of the triangle that contains both nodes – the one that is subject for potential evaluation and the one contributing with its potential. This method requires only minor derivations on based on the geometry of the given mesh. If geometry does not change, the method allows creation of a constant matrix and, possibly, finding its inverse form for very fast and accurate solution of Poisson problem.

Numerical results acquired for 2D problem of plasma advective transport along a channel representing the linear plasma head, showed typical distribution of plasma species for the case of pure convection, as well as for the case of recombination. The length of the plasma plume and average number density of plasma species are found to be underestimated in the case of 1D

plasma fade. The 2D model introduces corrections into the expected profiles of number density taken at different distance from the outlet of the generation chamber.

REFERENCES

1. A. E. Koniges, “Industrial Strength Parallel Computing”, 2000, Morgan Kaufmann Publishers, San Francisco

2. M. A. Lieberman, A. J. Lichtenberg, “Principles of plasma discharges and materials processing”, 2nd Ed, 2005, Wiley-Interscience, Hoboken, NJ.

3. K. W. Johnson, “Atmospheric pressure plasma enhanced chemical vapor deposition : design and application”, Thesis, Mechanical Engineering Department, North Dakota State University, 2011, Fargo, ND.

4. A. Sarani, A. Nikiforov, N. De Geyter, R. Morent, C. Leys, ., “Characterization of an atmospheric pressure plasma jet and its application for treatment of non-woven textiles”, Proceedings of 20th international symposium on plasma chemistry, 2011.

5. A. Bogaerts, E. Neyts, R. Gijbels, J. van der Mullen, “Gas discharge plasmas and their applications”, Spectrochimica Acta Part B-Atomic Spectroscopy, 2002, 57(4), pp. 609-658.

6. A. A. Fridman, “Plasma chemistry”, 2008, Cambridge University Press, Cambridge, NY.

7. S. Z. Li, J. P. Lim, J. G. Kang, H. S. Uhm, “Comparison of atmospheric-pressure helium and argon plasmas generated by capacitively coupled radio-frequency discharge”, Physics of Plasmas, 2006, 13(9)

8. I. A. Kossyi, A. Y. Kostinsky, A. A. Matveyev, V. P. Silakov, "Kinetic scheme of the non-equilibrium discharge in nitrogen-oxygen mixtures", Plasma Sources Sci. Technol., 1992, 1, pp. 207-220

9. J. M. Stillahn, K. J. Trevino, E. R. Fisher, "Plasma Diagnostics for Unraveling Process Chemistry", Annu. Rev. Anal. Chem., 2008, 1, pp. 261–291

10.D. Orlicki, V. Hlavaceky, H. J. Viljoenz, "Modeling of a-Si : H deposition in a DC glow discharge reactor", Journal of Material Research, 1992, 7(8), pp. 2160 - 2181

11 G. Chen, “Nanoscale Energy Transport and Conversion”, 2005, Oxford University Press, New York

12. S. Jennings, "The mean free path in air", Journal of Aerosol Science, 1988, 19 (2)

13. Hirschfelder, Curtiss, Bird, “Molecular Theory of Gases and Liquids”, 1954, Wiley, New York

14. “Noble Gas”, Encyclopedia Britannica, 2008

15. BOLSIG+ Software Package, available from: http://www.siglo-kinema.com/bolsig.htm, last accessed: 11/06/2012

16. U. Fantz, "Basics of plasma spectroscopy", Plasma Sources Sci. Technol., 2006, 15, pp. S137–S147

17. R. A. Gottscho, T. A. Miller, "Optical Techniques in Plasma Diagnostics", Pure Appi. Chem., 1984, 56(2), pp. 189-208

18. M. S. Mokrov, Y. P. Raizer, "On the mechanism of the negative differential resistance of a Townsend discharge", Plasma Sources Sci. Technol., 2008, 17

19. O. A. Omarova and A. A. Rukhadzeb, "On the Theory of Plasma Streamer Development", Kratkie Soobshcheniya po Fizike, 2009, 36(10), pp. 3–8

20. P. M. Windham, P. J. Joseph, J. A. Weinman, “Negative Helium Ions”, Physical Review, 1958, 109(4), pp. 1193-1195

21. B. L. Donnally, G. Thoeming, “Helium Negative Ions From Metastable Helium Atoms”, Physical Review, 1967, 159(1), pp. 87-90

22. D. J. Nicholas, C. W. Trowbrid, W.D. Allen, “Lifetime Of A Negative Helium Ion”, Physical Review, 1968, 167(1), pp. 38-42

23. S. I. Krasheninnikov, A. Yu. Pigarov, S. Takamura, N. Ohno, B. Lipschultz, J. T. Terry, “Molecular Effects in Plasma Recombination”, 27th EPS Conference on Contr. Fusion and Plasma Physics, 12-16 June 2000, Budapest

24 C. F. Eyring, "Pulling Electrons out of Metals by Intense Electrical Fields", Thesis, Department of Physics, California Institute of Technology, 1923

25 P. W. Bridgman, "General Considerations on the Emission of Electrons From Conductors Under Intense Fields", Physical Review, 1929, 34, pp. 1411-1417

26. C. R. Crowell, "The Richardson constant for thermionic emission in Schottky barrier diodes", Solid-State Electronics, 1965, 8 (4), pp. 395–399

27. M. E. Kiziroglou, X. Li, A. A. Zhukov, P. A. De Groot, C. H. De Groot, "Thermionic field emission at electrodeposited Ni-Si Schottky barriers", Solid-State Electronics, 2008, 52 (7), pp. 1032–1038

28. J. Orloff, "Schottky emission", Handbook of Charged Particle Optics (2nd ed.), 2008, CRC Press

29. E. L. Murphy, G. H. Good, "Thermionic Emission, Field Emission, and the Transition Region", Physical Review ,1956, 102 (6), pp. 1464–1473

30. V. L. Granovsky, “Electric Current in Gas”, Steady Current, Nauka (Science), 1971, Moscow

31. X. Yang, M. Moravej, G. R. Nowling, S. E. Babayan, J. Panelon, J. P. Chang, R. F. Hicks, “Comparison of an atmospheric pressure, radio-frequency discharge operating in the alpha and gamma modes”, Plasma Sources Science & Technology, 2005, 14(2), pp. 314-320

32 A. G. Kulikovskiy, G. A. Lyubimov, “Magnetohydrodynamics”, 1962, State Physics and Mathematics Press, Moscow

33. A. Schutze, J. Y. Jeong, S. E. Babayan, J. Park, G. S. Selwyn, R. F. Hicks, “The atmospheric-pressure plasma jet: A review and comparison to other plasma sources”. IEEE Transactions on Plasma Science, 1998, 26(6), pp. 1685-1694

34. D. Braun, V. Gibalovt, G. Pietsch, "Two-dimensional modelling of the dielectric barrier discharge in air", Plasma Sources Sci. Technol., 1992, 7, pp. 166-174

35. N. S. Rudenko and V. I. Smetanin, "Streamer Propagation Mechanism on the Basis of Plasma Oscillations", Russian Physics Journal, 1977, 20(7), pp. 859-864

36. H. P. Li, W. T. Sun, H. B. Wang, G. Li, C. Y. Bao, "Electrical Features of Radio-frequency, Atmospheric pressure, Bare-metallic-electrode Glow Discharges", Plasma Chem Plasma Process, 2007, 27, pp. 529–545

37. C. Tendero, C. Tixier, P. Tristant, J. Desmaison, P. Leprince, “Atmospheric pressure plasmas: A review”, Spectrochimica Acta Part B-Atomic Spectroscopy, 2006, 61(1), pp. 2-30

38. V. Hopfe, D. W. Sheel, "Atmospheric-Pressure PECVD Coating and Plasma Chemical Etching for Continuous Processing", IEEE Transactions on Plasma Science, 2007, 35(2)

39. M. Moravej, R. F. Hicks, "Atmospheric Plasma Deposition of Coatings Using a Capacitive Discharge Source", Chem. Vap. Deposition, 2005, 11, pp. 469-476

40. S. E. Alexandrov, M. L. Hitchman, "Chemical Vapor Deposition Enhanced by Atmospheric Pressure Non-thermal Non-equilibrium Plasmas", Chem. Vap. Deposition, 2005, 11, 457-468

41. V. Rohani, G. Bauville, B. Lacour, V. Puech, F. D. Duminica, E. Silberberg, “Study of the treatment homogeneity in plasma assisted chemical vapour deposition by atmospheric pressure dielectric barrier discharge”, Surface & Coatings Technology, 2008, 203, pp. 862-867

42. H. Conrads, M. Schmidt, “Plasma generation and plasma sources”, Plasma Sources Science & Technology, 2000, 9(4), pp. 441-454

43. A. V. Chirokov, “Stability of Atmospheric Pressure Glow Discharge”, Thesis, Drexel University, 2005

44. J. Park, I. Henins, H. W. Herrmann, G. S. Selwyn, R. F. Hicks, “Discharge phenomena of an atmospheric pressure radio-frequency capacitive plasma source”, Journal of Applied Physics, 2001, 89(1), pp. 20-28

45. F. F. Young, C. H. Wu, “A Comparative-Study Between Nonequilibrium And Equilibrium-Models of RF Glow-Discharges”, Journal Of Physics D-Applied Physics, 1993, 26(5), pp. 782-792

46 F. Lepkojus, N. Watanabe, W. Buscher, K. Cammanna, G. Bohm, "A simple radiofrequency helium discharge plasma (RFP) for spectroscopic purposes", Journal of Analytical Atomic Spectrometry, 1999, 14, pp. 1511-1513

47 H. W. Berry, “Energy Distribution of Electrons from Ionizing Collisions of Atoms and Ions”, Physical Review, 1962, 127(5)

48. F. F. Chen, “Introduction to plasma physics and controlled fusion”, 2nd Ed, 1984, Plenum Press, New York

49. M. Shoji, M. Sato, "Argon gas breakdown with bare and insulated electrodes in dc-biased RF field", J. Phys. D: Appl. Phys., 1999, 32 , pp. 1640–1645

50. T. R. Govindan , M. Meyyappan, “One-dimensional modeling studies of the gaseous electronics conference RF reference cell”, Journal of Research of the National Institute of Standards and Technology, 1995, 100(4), pp. 463-472

51. R. Fitzpatrick, “Plasma Physics Lectures”, 2012, available from: http://farside.ph.utexas.edu/teaching/plasma/lectures1/Plasmahtml.html, last accessed: 11/06/2012

52. C. Suplee, A. Bhattacharjee, K. Donahue, “The plasma universe”, 2009, Cambridge University Press, Cambridge, NY

53. M. Meyyappan, T. R. Govindan, “Radio-Frequency Discharge Modeling - Moment Equations Approach”, Journal Of Applied Physics, 1993, 74(4), pp. 2250-2259

54. Garcia Odd Erik, “Plasma Fluid Models”, Riso National Laboratory, available from: http://ftp.risoe.dk/pub/plf/erga/plasma/fluid.pdf, last accessed: 11/06/2012

55. J. P. Boeuf, “Numerical-Model of RF Glow-Discharges”, Physical Review A, 1987, 36(6), pp. 2782-2792

56 J. H. Parker, J. J. Lowke, "Theory of Electron Diffusion Parallel to Electric Fields. I. Theory", Physical Review, 1969, 181(1), pp. 290-301

57. S. V. Berezhnoi, I. D. Kaganovich, L. D. Tsendin, V. A. Schweigert, "Fast modeling of the low-pressure capacitively coupled radio-frequency discharge based on the nonlocal approach", Appl. Phys. Lett., 1996, 69 (16)

58. R. Wester, S. Seiwert, “Numerical Modelling of RF Excited CO 2 Laser Discharges”, Journal Of Physics D: Applied Physics, 1991, 24(8), pp. 1371-1375

59. D. Edelson, K. B. McAfee, "Improved Pulsed Townsend Discharge Experiment", Review of Scientific Instruments, 35(2), 1964, pp. 187-194

60. G. G. Lister, “Low-Pressure Gas-Discharge Modeling”, Journal of Physics D-Applied Physics, 1992, 25(12), pp. 1649-1680

61. L.S. Frost, A. V. Phelps, “Rotational Excitation And Momentum Transfer Cross Sections For Electrons In H_2 And N_2 From Transport Coefficients”, Physical Review, 1962, 127(5), pp. 1621-1633

62. Y. Ohmori, M. Shimozuma, H. Tagashira, “Boltzmann-Equation Analysis of Electron Swarm Behavior In Nitrogen”, Journal of Physics D-Applied Physics, 1988, 21(5), pp. 724-729

63. G. J. M. Hagelaar, L. C. Pitchford, “Solving the Boltzmann equation to obtain electron transport coefficients and rate coefficients for fluid models”, Plasma Sources Science and Technology, 2005, 14(4), pp. 722-733

64. H. W. Ellis, R. Y. Pai, E. W. McDaniel, E. A. Mason, L. A. Viehland, “Transport properties of gaseous ions over a wide energy range”, Atomic Data and Nuclear Data Tables, 1976, 17(3), pp. 177-210

65. M. G. Kong, X. T. Deng,, “Electrically efficient production of a diffuse nonthermal atmospheric plasma”, IEEE Transactions on Plasma Science, 2003, 31(1), pp. 7-18

66. Y. Lin, R. A. Adomaitis, "Simulation and Model Reduction Methods for an RF Plasma Glow Discharge", Journal of Computational Physics, 2001, 171, pp. 731–752

67 A. Arnau, M. Panelba, P. M. Echenique, F. Flores, R. H. Ritchie, "Stopping Power for Helium in Aluminum", Physical Review Letters, 1990, 65(8)

68 M. Pounds, S. Tazi, M. Salanne, P. A. Madden, "Ion adsorption at a metallic electrode: an ab initio based simulation study", Journal of Physics: Condensed Matter, 2009, 21

69 R. W. Shokwiler, L. Lefton, “An Introduction to Parallel and Vector Scientific Computing”, 2006, Cambridge University Press, New York

70. OpenMPI, available from: http://www.open-mpi.org/, last accessed: 11/06/2012

71 P. S. Pacheco, “Parallel Programming with MPI”, 1997, Morgan Kaufmann Publishing, Inc, San Francisco

72. S. V. Patankar, “Numerical heat transfer and fluid flow. Series in computational methods in mechanics and thermal sciences”, 1980, Hemisphere Pub. Corp., McGraw-Hill, Washington, New York

73. D. I. Scharfetter, H. K. Gummel, “Large-Signal Analysis Of A Silicon Read Diode Oscillator”, IEEE Transactions on Electron Devices, 1969, ED16(1), pp. 64-77.

74. T. Austin, M. Berndt, D. Moulton, “A Memory Efficient Parallel Tridiagonal Solver”, 2004, Preprint LA-UR-03-4149, available from: http://math.lanl.gov/~berndt/Papers/ parallel-line-solver.pdf, last accessed: 11/06/2012

75 S. Brawer, “Introduction to Parallel Programming”, 1989, Academic Press, Inc, San Diego

76. G. Karniadakis, R. M. Kirby, “Parallel scientific computing in C++ and MPI : a seamless approach to parallel algorithms and their implementation”, 2003, Cambridge University Press, New York, XI

77 L. Baker, B. J. Smith, “Parallel Programming”, 1996, McGraw-Hill, New York

78 M. A. Lieberman, “Dynamics of collisional, capacitive RF sheath”, IEEE Transaction of Plasma Science, 1989, 17(2), pp. 338-341

79 V. A. Godyak, N. Sternberg, “Dynamic model of the electrode sheaths in symmetrically driven rf discharges”, Phys. Rev. A, 1990, 42(4), pp. 2299-2312

80 M. A. Sobolewski, “Experimental test of models of radio-frequency plasma sheaths”, Appl. Phys. Lett., 1997, 70 (8)

81. E. M. Oks, "Physics and technique of plasma electron sources", Plasma Sources Sci. Technol., 1992, 1, pp. 249-255

82. Z. Fan, Y. Zhao, A. Kaufman, Y. He, "Adapted Unstructured LBM for Flow Simulation on Curved Surfaces", Eurographics/ACM SIGGRAPH Symposium on Computer Animation, 2005

83. Mathworks Matlab Software Package, available from: http://www.mathworks.com/products/matlab/, last accessed: 11/06/2012

84. B. Delaunay, " Sur la sphère vide", Izvestia Akademii Nauk SSSR, Otdelenie Matematicheskikh i Estestvennykh Nauk, 1934, 7, pp.793–800

85. G. Peng, H. Xi, C. Duncan, S. H. Chow, "Finite volume scheme for the lattice Boltzmann method on unstructured meshes", Physical Review E, 1999, 59(4), pp.4675-4682

86. S. Ubertini, G. Bella, S. Succi, "Lattice Boltzmann method on unstructured grids: Further developments", Physical Review E, 2003, 68

87 J. Stewart, "Vector Calculus", Calculus: Early Transcendentals (6 ed.), 2008, Thomson Brooks/Cole

88. M. Stiebler, J. Tolke, M. Krafczyk, "An upwind discretization scheme for the finite volume lattice Boltzmann method", Computers and Fluids, 2006, 35, pp. 814-819

89. M. Younas, "Scalable, Parallel Poisson Solvers for CFD Problems", Dissertation, Faculty of Mathematics and Natural Sciences, Johann Bernoulli Institute for Mathematics and Computer Science, University of Groningen, 2012, The Netherlands

90. W. H. Hayt, J. A. Buck, "Engineering Electromagnetics", 2011, McGraw-Hill Science

91. L. Borges, P. Daripa, "A Fast Parallel Algorithm for the Poisson Equation on a Disk", Journal of Computational Physics, 2001, 169, pp. 151–192

92 R. H. Bisseling, "Parallel Scientific Computation", 2004, Oxford University Press, New York

93. W. F. Ames, "Numerical Methods for Partial Differential Equations", 1977, Academic Press, New York

94. F. Ethridge, L. Greengard, "A New Fast-Multipole Accelerated Poisson Solver in Two Dimensions", SIAM Journal on Scientific Computing, 2001, 23(3), pp. 741–760

95. A. McAdams, E. Sifakis, J. Teran, "A parallel multigrid Poisson solver for fluids simulation on large grids", Eurographics/ ACM SIGGRAPH Symposium on Computer Animation, 2-4 July 2010, Madrid, Spain

96. S. R. Fulton, P. E. Ciesielski, W. H. Schubert, "Multigrid Methods for Elliptic Problems: A Review", Monthly Weather Review, 1986, 114, pp. 944-959

97. M. P. Bradley, "Edge Effects in the Parallel Plate Capacitor: The Maxwell Transformation and the Rogowski Profile", EP464, Fall 2004, available from: physics.usask.ca/~bradley/pll_plate_edge.pdf, last accessed: 11/06/2012

98. S. Catalan-Izquierdo, J. M. Bueno-Barrachina, C. S. Cañas-Peñuelas, F. Cavallé-Sesé, "Capacitance Evaluation on Parallel-Plate Capacitors by Means of Finite Element Analysis", International Conference on Renewable Energies and Power Quality (ICREPQ'09), Valencia (Spain), 15th to 17th April, 2009

99.M. C. Hegg, A. V. Mamishev, "Influence of Variable Plate Separation on Fringing Electric Fields in Parallel-Plate Capacitors", IEEE, 2004 International Symposium on Electrical Insulation, Indianapolis, IN USA, 19-22 September, 2004

100. G. W. Parker, "Electric field outside a parallel plate capacitor", Am. J. Phys., 2002, 70

APPENDIX A

Table A.1
Typical electrons' rate parameters calculated with BOLSIG+

E/N Td	μ_e, $m^2/V.s$	D_e, m^2/s	α, 1/m	ω_{mean}, eV
0	0.261000000	0.0488	0	0
1	0.179970972	0.079342042	0	0.5641
2	0.127274757	0.106434446	$7.699\times10^{-58+}$	1.082
3	0.105131927	0.129954226	$7.185\times10^{-18+}$	1.626
4	0.092962674	0.154032228	1.882E-07	2.224
5	0.08563135	0.181422351	0.002095132	2.906
6	0.081277213	0.214096982	0.176354373	3.692
7	0.079044323	0.2497488	2.42134581	4.508
8	0.078151167	0.282274571	12.6078732	5.223
9	0.077927878	0.30832496	38.210562	5.776
10	0.078039522	0.328197685	84.428682	6.186
11	0.078225596	0.34338134	153.540894	6.492
12	0.078448885	0.355364519	245.762166	6.729
13	0.07863496	0.365077593	360.34011	6.917
14	0.078821034	0.373264858	495.76995	7.074
15	0.079007108	0.380335678	650.54691	7.207
16	0.079155967	0.386662201	823.32744	7.324
17	0.079304827	0.392244427	1012.23057	7.429
18	0.079416471	0.397454505	1216.45017	7.525
19	0.079565331	0.402292434	1434.37398	7.614
20	0.079676975	0.406758215	1665.19587	7.697
21	0.07978862	0.411223996	1907.57229	7.775
22	0.079900264	0.415689777	2160.96582	7.85
23	0.079974694	0.419411261	2424.30162	7.922
24	0.080086338	0.423504894	2697.8484	7.992
25	0.080197983	0.427226378	2979.9939	8.059
26	0.080272413	0.43132001	3270.2007	8.125
27	0.080384057	0.435041495	3565.7817	8.19
28	0.080458487	0.43839083	3872.1111	8.253
29	0.080570131	0.442112314	4183.8147	8.315
30	0.080644561	0.445833799	4500.8925	8.376
31	0.080756206	0.449183134	4826.0316	8.436
32	0.080830635	0.452904618	5156.5449	8.495
33	0.080905065	0.456253954	5492.4324	8.554

Table A.1
Typical electrons' rate parameters calculated with BOLSIG+
(continued)

E/N Td	μ_e, $m^2/V.s$	D_e, m^2/s	α, 1/m	ω_{mean}, eV
34	0.081016709	0.45960329	5836.3812	8.613
35	0.081091139	0.463324774	6180.33	8.67
36	0.081202784	0.46667411	6532.3401	8.728
37	0.081277213	0.470023445	6889.7244	8.785
38	0.081388858	0.473372781	7249.7958	8.841
39	0.081463288	0.477094265	7615.2414	8.898
40	0.081537717	0.480443601	7983.3741	8.954
41	0.081649362	0.483792937	8356.881	9.01
42	0.081723791	0.487142272	8733.075	9.065
43	0.081835436	0.490863756	9114.6432	9.121
44	0.081909866	0.494213092	9498.8985	9.176
45	0.08202151	0.497562428	9885.8409	9.231
46	0.08209594	0.500911764	10275.4704	9.286
47	0.082207584	0.504633248	10670.4741	9.341
48	0.082319229	0.507982583	11065.4778	9.396
49	0.082393659	0.511331919	11465.8557	9.451
50	0.082505303	0.515053403	11868.9207	9.506
51	0.082579733	0.518402739	12274.6728	9.56
52	0.082691377	0.522124223	12680.4249	9.615
53	0.082803022	0.525473559	13091.5512	9.67
54	0.082877452	0.529195043	13505.3646	9.724
55	0.082989096	0.532544379	13919.178	9.779
56	0.083100741	0.536265863	14338.3656	9.833
57	0.083212385	0.539615199	14757.5532	9.888
58	0.083286815	0.543336683	15179.4279	9.943
59	0.083398459	0.547058167	15601.3026	9.997
60	0.083510104	0.550407503	16028.5515	10.05
61	0.083621748	0.554128987	16455.8004	10.11
62	0.083696178	0.557850471	16885.7364	10.16
63	0.083807823	0.561571955	17315.6724	10.22
64	0.083919467	0.565293439	17748.2955	10.27
65	0.084031112	0.569014923	18183.6057	10.33
66	0.084142756	0.572736407	18621.603	10.38
67	0.084254401	0.576457891	19056.9132	10.44
68	0.08432883	0.580179376	19497.5976	10.49
69	0.084440475	0.58390086	19938.282	10.55

Table A.1
Typical electrons' rate parameters calculated with BOLSIG+
(continued)

E/N Td	μ_e, $m^2/V.s$	D_e, m^2/s	α, 1/m	ω_{mean}, eV
70	0.084552119	0.587622344	20378.9664	10.60
71	0.084663764	0.591715976	20822.3379	10.66
72	0.084775408	0.59543746	21268.3965	10.71
73	0.084887053	0.599158945	21714.4551	10.77
74	0.084998697	0.603252577	22160.5137	10.83
75	0.085110342	0.606974061	22609.2594	10.88
76	0.085221987	0.611067694	23058.0051	10.94
77	0.085333631	0.614789178	23509.4379	10.99
78	0.085445276	0.61888281	23960.8707	11.05
79	0.08555692	0.622976443	24412.3035	11.11
80	0.085668565	0.626697927	24866.4234	11.16
81	0.085780209	0.63079156	25320.5433	11.22
82	0.085891854	0.634885192	25774.6632	11.28
83	0.086003498	0.638978825	26228.7831	11.33
84	0.086115143	0.643072457	26685.5901	11.39
85	0.086264002	0.64716609	27139.71	11.45
86	0.086375647	0.651259722	27596.517	11.5
87	0.086487291	0.655725503	28053.324	11.56
88	0.086598936	0.659819136	28510.131	11.62
89	0.08671058	0.663912768	28966.938	11.68
90	0.086822225	0.668378549	29450.616	11.74
91	0.086933869	0.672472182	29907.423	11.79
92	0.087045514	0.676565814	30364.23	11.85
93	0.087194373	0.681031595	30821.037	11.91
94	0.087306018	0.685497376	31277.844	11.97
95	0.087417662	0.689591009	31734.651	12.03
96	0.087529307	0.69405679	32218.329	12.09
97	0.087640951	0.698522571	32675.136	12.15
98	0.087752596	0.702988352	33131.943	12.2
99	0.087901455	0.707454133	33588.75	12.26
100	0.0880131	0.711919914	34072.428	12.32

[+]This value is taken from fit-data. The original result from BOLSIG+ is zero.

APPENDIX B

Table B.1
Typical He^+ ions' rate parameters found in [64]

E/N Td	μ_p $\times 10^{-3}$ m^2/V.s	E/N Td	μ_p $\times 10^{-4}$ m^2/V.s
0	1.05	40	9.28
1	1.04	50	8.97
2	1.04	60	8.67
3	1.04	80	8.12
4	1.03	100	7.67
5	1.03	120	7.25
6	1.03	150	6.78
8	1.02	200	6.12
10	1.02	250	5.60
12	1.01	300	5.19
15	1.00	400	4.58
20	0.99	500	4.17
25	0.974	600	3.81
30	0.96	700	3.57

APPENDIX C

Initial distribution of plasma parameters for 2D advective transport of plasma

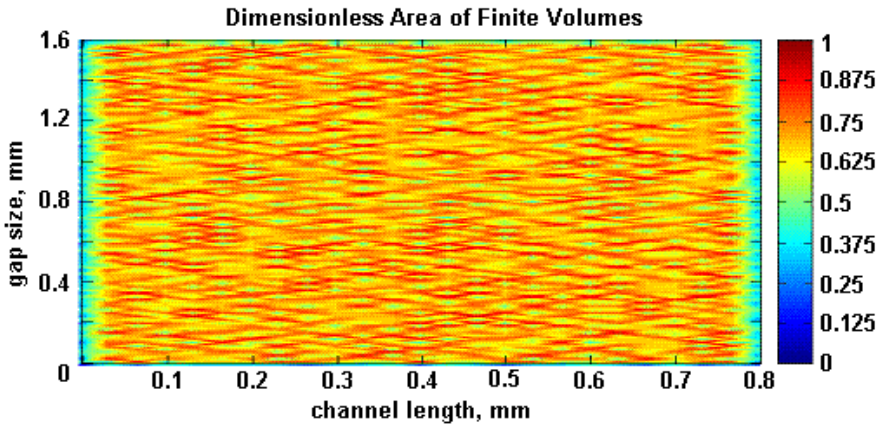

Figure C.1. Area of the finite volumes

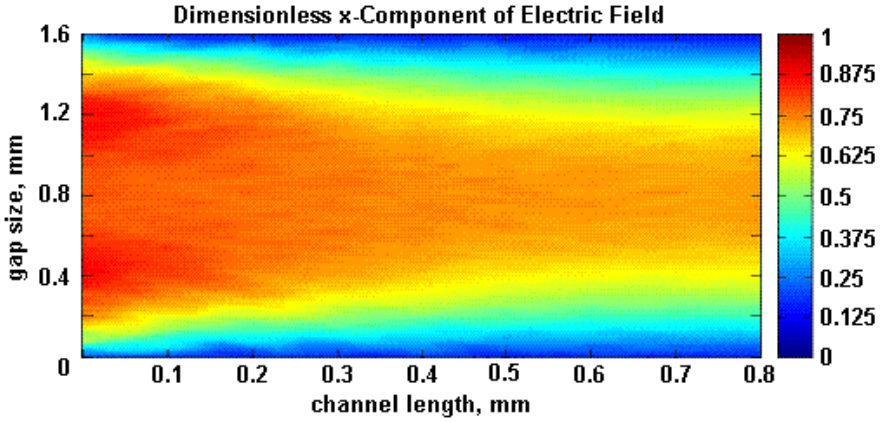

Figure C.2. Initial distribution of x-component of electric field

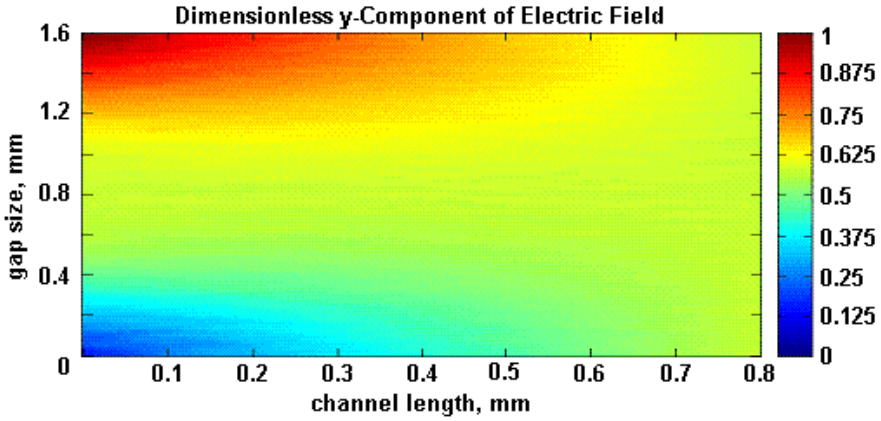

Figure C.3. Initial distribution of y-component of electric field

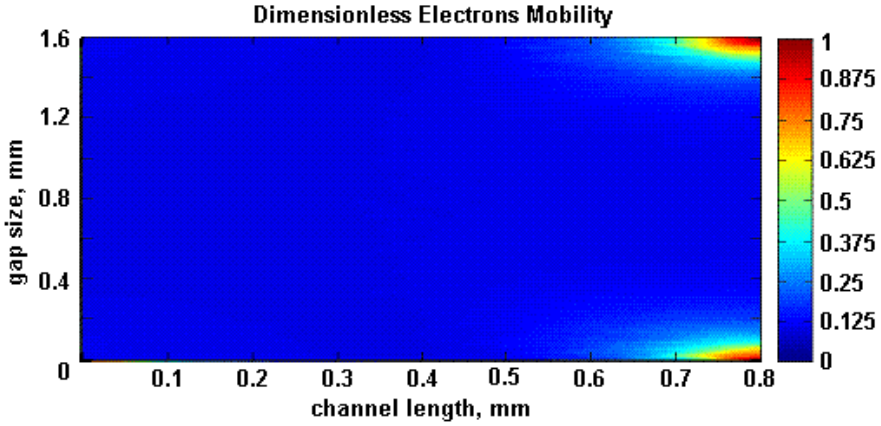

Figure C.4. Initial distribution of electrons mobility

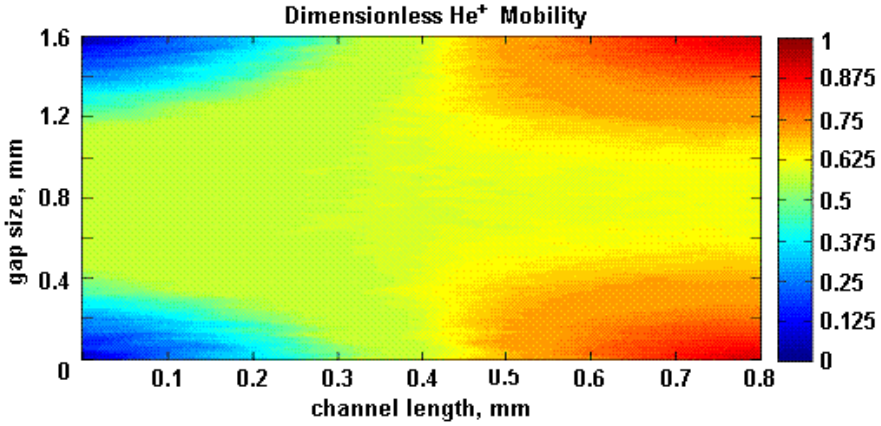

Figure C.5. Initial distribution of positive ions mobility

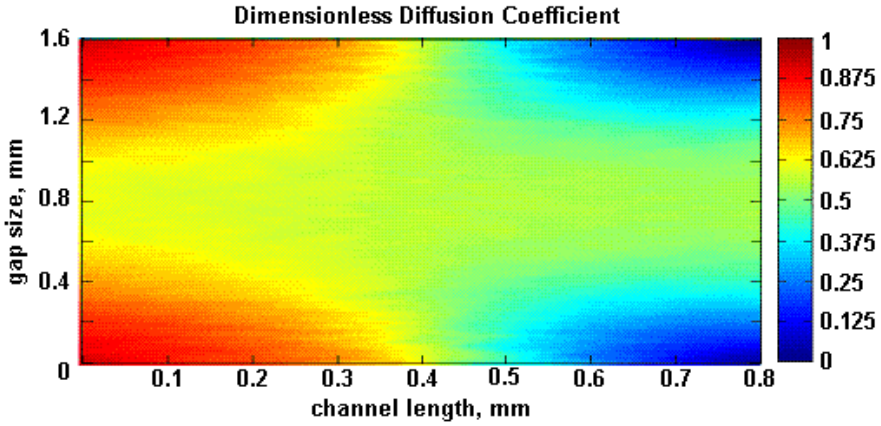

Figure C.6. Initial distribution of electrons diffusion coefficient

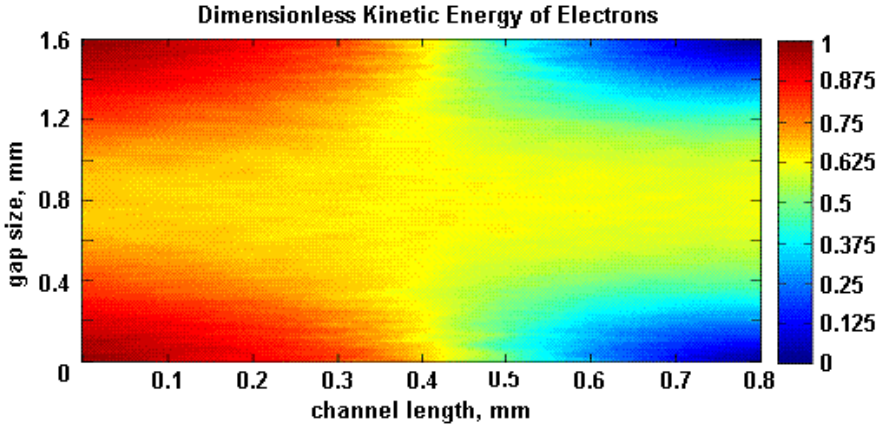

Figure C.7. Initial distribution of electrons kinetic energy

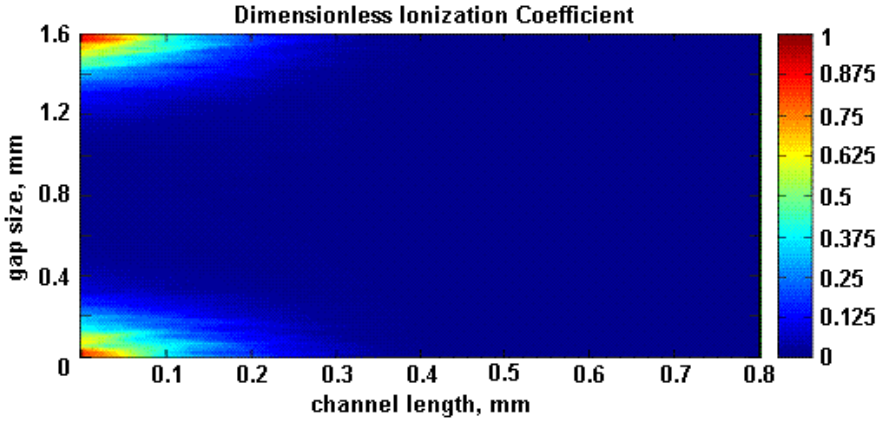

Figure C.8. Initial distribution of ionization coefficient

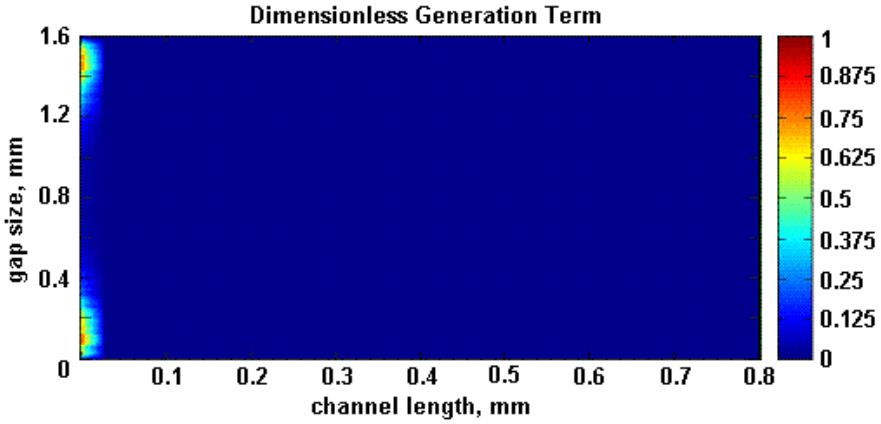

Figure C.9. Initial distribution of generation term

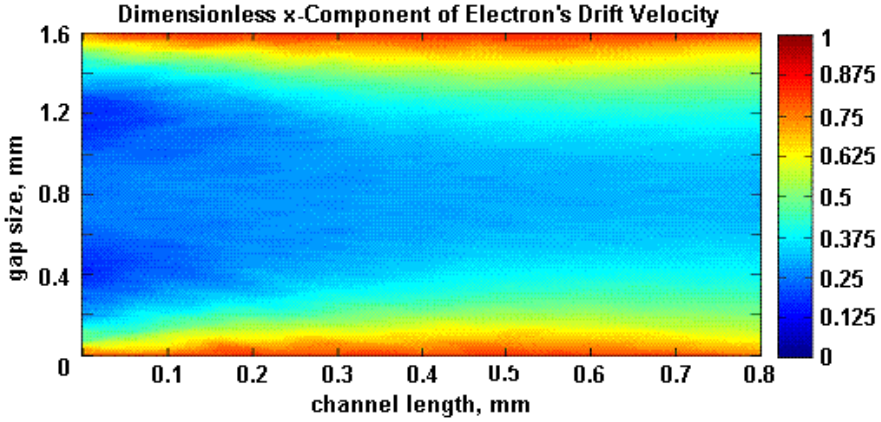

Figure C.10. Initial distribution of x-component of electrons drift velocity

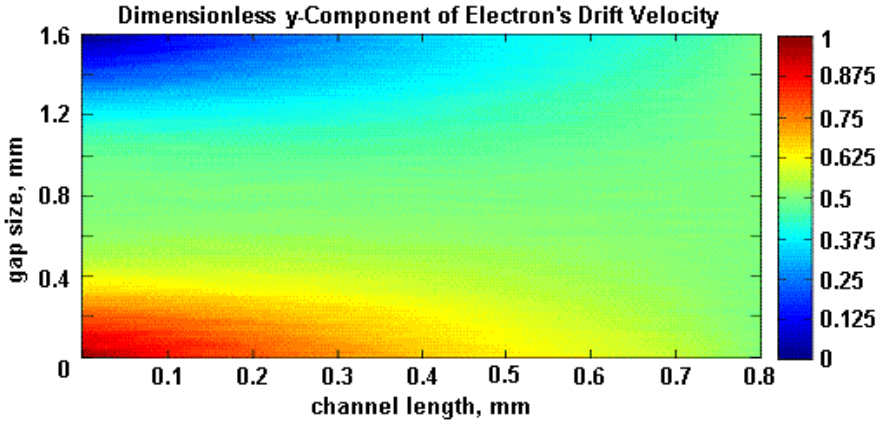

Figure C.11. Initial distribution of y-component of electrons drift velocity

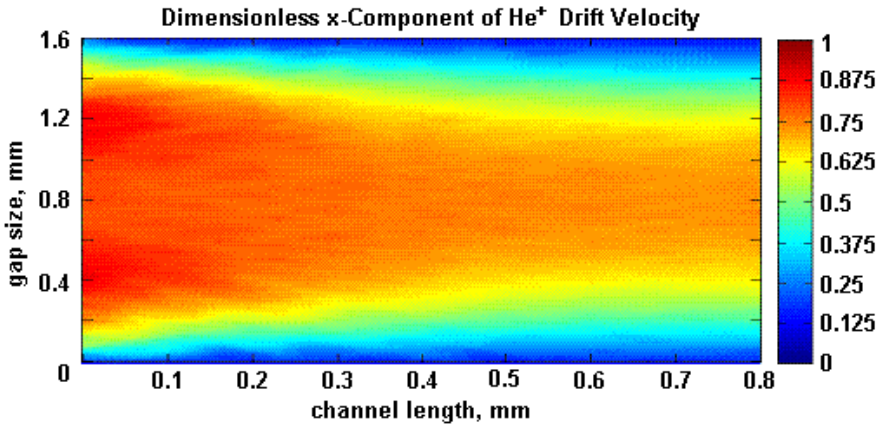

Figure C.12. Initial distribution of x-component of positive ions drift velocity

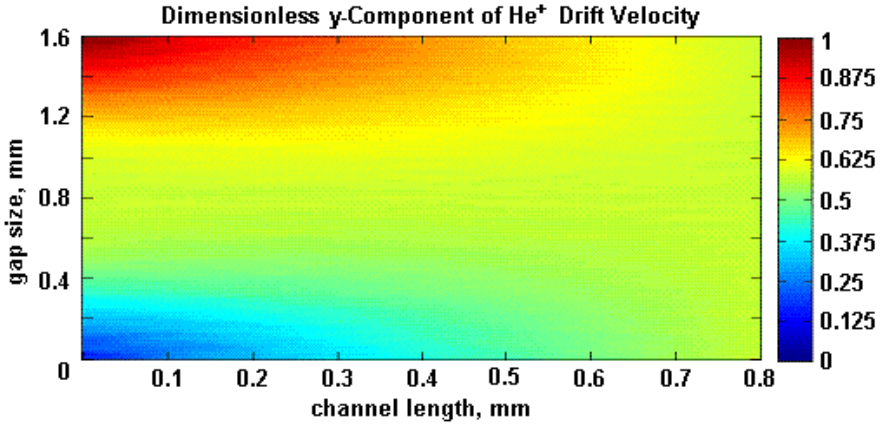

Figure C.13. Initial distribution of y-component of positive ions drift velocity